NASA CONTRACTOR REPORT 166608

135P.

Parametric Analysis of a Passive Cyclic Control Device for Helicopters

Hiroyuki Kumagai

32768

CONTRACT NCC 2-175
October 1984

NASA

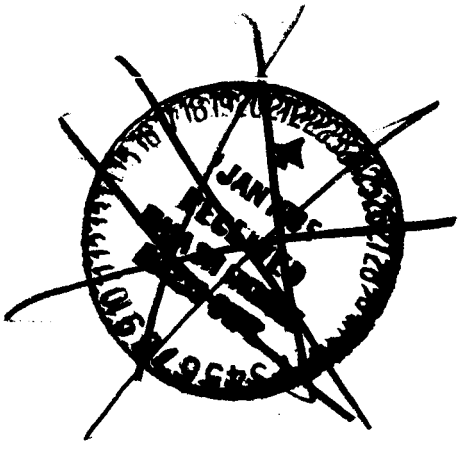

TABLE OF CONTENTS

Parametric Analysis of a Passive Cyclic Control Device for Helicopters

Hiroyuki Kumagai

The University of Kansas Center for Research Inc.
2291 Irving Hill Dr. - Campus West
Lawrence, KS 66045

Summary

A parametric study of a passive device which provides a cyclic longitudinal control moment for a helicopter rotor was performed. It utilizes a rotor blade tip which is structurally decoupled from the blade inboard section. This rotor configuration is generally called the Free-Tip Rotor.

A two dimensional numerical model was used to review the Constant Lift Tip Rotor, a predecessor of the current configuration, and then the same model was applied to the Passive Cyclic Control Device. The Constant Lift Tip was proven to have the ability to suppress the vibratory lift loading on the tip around the azimuth and to eliminate a significant negative lift peak on the advancing tip. The Passive Cyclic Control Device showed a once-per-revolution lift oscillation with a large amplitude, while minimizing the higher harmonic terms of the lift oscillation. This once-per-revolution oscillation results in the cyclic moment to trim the rotor longitudinally.

A rotor performance analysis was performed by a three dimensional numerical model. It indicated that the vortices shed from the junction between the tip and the inboard section has a strong influence on the tip, and it may severely limit the tip performance.

It was also shown that the Free-Tip allows the inboard section to have a larger twist, which results in a better performance.

1. Introduction

The rotor blade tip has a strong influence on the overall rotor performance and the load characteristics. Therefore, an improvement on the tip aerodynamics is expected to result in a large improvement in total rotor performance.

A basic configuration of the Free-Tip Rotor consists of a conventional blade inboard section and a tip section of 10 percent radius whose pitching motion is decoupled from the inboard section. There is a passive pitch control device built into the inboard section of the blade, adjacent to the tip section. This control device (controller) generates a constant pitch-up moment, and the pitch angle of the tip is determined by a moment balance between this control moment and other external moments, such as aerodynamic moment, moment due to lift and aerodynamic center offset from the tip pitch axis, etc. The Free-Tip Rotor concept is shown schematically in Figure 1-1. More detailed description is given in Reference 1.

There are two applications of the Free-Tip Rotor and they can be classified as follows.

1.1. Free-Tip Rotor I (FTR I).

If there is a large offset between tip pitch axis and the aerodynamic center, it results in a large negative c_{m_α} around the pitch axis. This large negative c_{m_α} enables the tip to respond to the perturbations.

The resulting tip pitch motion generates a relatively uniform lift distribution around the azimuth. This will improve the lift over drag ratio, L/D of the helicopter by eliminating the negative lift at the tip on the advancing side. It also helps to reduce the drag associated with compressibility on the advancing side as the resulting angle of attack has a small positive

Figure 1-1 Free-Tip Rotor Schematics

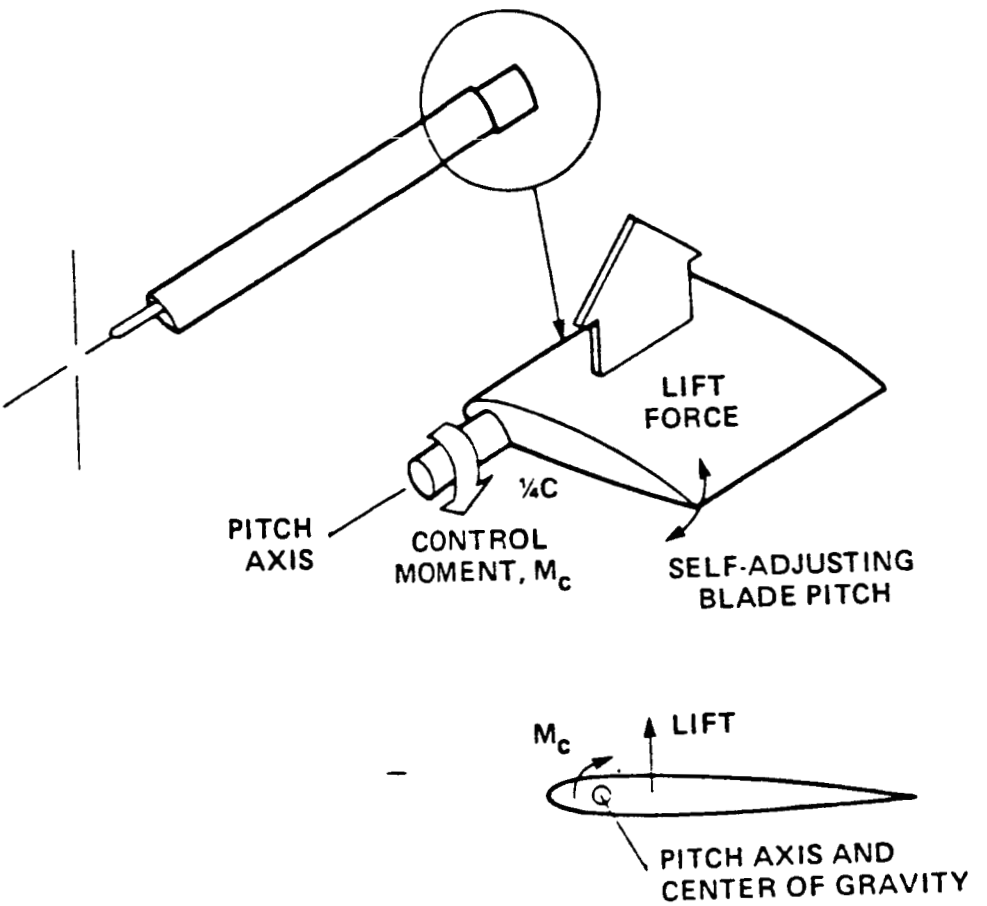

value compared with a large negative angle of attack on a conventional tip.

Since the amplitude of the lift oscillation on the tip is also suppressed, the Free-Tip should also improve rotor vibration characteristics.

In the case of Free-Tip Rotor I concept, which is also called Constant Lift Tip Rotor, the control moment, externally applied by the controller is constant and independent on the blade azimuth location.

1.2. Free-Tip Rotor II (FTR II).

A basic concept of the Free-Tip Rotor II is the utilization of the Free-Tip as a passive cyclic control device for longitudinal trim. For this purpose, a once-per-revolution cyclic pitch motion must be induced on the tip section. This can be done by a pitch control mechanism which generates a control moment as a function of local dynamic pressures. Such a mechanism will add a complexity to the system. However, it is still possible to use the pitch control mechanism with a constant control moment, designed for the FTR I, for this application if an additional external pitch-down moment with a once-per-revolution variation is also applied to the tip. The sum of these moments induces a once-per-revolution pitch oscillation on the tip. Such a periodic external pitch-down moment can be created by a large negative pitching moment of the airfoil, or the drag acting on the tip with a negative dihedral. Since the aerodynamic pitching moment and drag are both functions of local dynamic pressure, the resulting pitching moment will have a once-per revolution variation. This configuration is called Passive Cyclic Control Device.

2. List of Symbols

a	sonic velocity (ft/sec)
a_1, b_1	first harmonic coefficients of $\ell(\psi)$ (lb/ft)
$b_\alpha(t)$	aerodynamic damping coefficient $(lb\ ft\ sec/ft)$
$b_\theta(t)$	mechanical damping coefficient $(lb\ ft\ sec/ft)$
c	chord length (ft)
$C(t)$	a sum of $b_\theta(t)$ and $b_\alpha(t)$ $(lb\ ft/sec/ft)$
c_{ℓ_α}	sectional lift curve slope
c_{L_α}	lift curve slope of three dimensional Free-Tip
c_{m_0}	moment coefficient around 25 % chord
$c_{m_{\alpha.13}}$	variation of moment coefficient around 13 % chord due to angle of attack
C_P	power coefficient
C_T	thrust coefficient
D	sectional drag on the Free-Tip (lb)
d_i, d_o	inner and outer diameters of the helical screw (ft)
H	inplane H-force (lb)
J	moment of inertia of the Free-Tip per unit span $(slug\ ft^2/ft)$

$K(t)$	a sum of $k_\theta(t)$ and $k_\alpha(t)$ $(lb\ ft/ft)$
$k_\alpha(t)$	aerodynamic spring coefficient $(lb\ ft/ft)$
$k_\theta(t)$	mechanical spring coefficient $(lb\ ft/ft)$
$\mathcal{L}$	longitudinal cyclic moment generated by Free-Tip $(lb\ ft/ft)$
$\mathcal{L}_1$	contribution of first harmonic lift component on the Free-Tip to the longitudinal cyclic moment $(lb\ ft/ft)$
ℓ_f, ℓ_a	forward and aft moment arms contributing to feathering moment (ft)
ℓ_{tip}	span of the Free-Tip (ft)
$\ell(\psi)$	sectional lift distribution on the Free-Tip around the azimuth (lb/ft)
$\ell_1(\psi)$	first harmonic component of sectional lift variation on the Free-Tip around the azimuth (lb/ft)
M	Mach number
$M(t)$	a sum of external moment $(lb\ ft/ft)$
M_{dh}	moment due to drag and dihedral (lb)
M_f	moment due to friction $(lb\ ft/ft)$
M_{fe}	feathering moment $(lb\ ft/ft)$
m_f, m_a	forward and aft masses contributing to feathering moment $(slug/ft)$

q	dynamic pressure (lb/ft^2)
R	radius of rotor (ft)
R_{tip}	radial location of the Free-Tip c. g. (ft)
T	thrust (lb)
V	helicopter forward flight speed (kts)
v_{tip}	nondiminsional flow velocity at the tip
X	inplane X-force (propulsive force) (lb)
Y	inplane Y-force (side force) (lb)
α	sectional angle of attack $(rad.)$
α_{HELIX}	helical screw angle $(rad.)$
α_{shaft}	rotor angle of attack, positive rearward $(deg.)$
β_0	coning angle $(deg.)$
β_{1c}	longitudinal flapping in shaft axis $(deg.)$
β_{1s}	lateral flapping in shaft axis $(deg.)$
Δc	nondimensional chordwise distance between Free-Tip pitch axis and aerodynamic center of the Free-Tip
Δc_d	sectional drag coefficient increment for Reynolds number effect compensation
Δc_{m_0}	sectional moment coefficient increment due to tab deflection

Γ	dihedral angle of the Free-Tip $(rad.)$
θ	pitch angle of Free-Tip measured from the tip path plane $(rad.)$
$\theta_{0.75}$	collective pitch control input measured at 75 % spanwise blade station $(deg.)$
θ_{1c}	lateral cyclic pitch control input $(deg.)$
θ_{1s}	longitudinal cyclic pitch control input $(deg.)$
θ_{tw}	blade twist, positive up $(deg.)$
μ	rotor advance ratio
μ'	friction coefficient
ν_N	nondimensional induced velocity component normal to the airfoil chord line
ρ	air density $(slug/ft^3)$
σ	rotor solidity
ϕ	inflow angle $(rad.)$
ψ	azimuthal angle $(deg.)$
Ω	angular velocity of rotor

3. Two Dimensional Analysis of FTR I

3.1. Numerical Model Description.

A computer program AZIMUTH was originally developed at NASA-Ames Research Center to model the tip response of the Free-Tip Rotor. This section describes a parametric study of the FTR I tip response characteristics, performed by the AZIMUTH. Prior to the parametric study, the program was modified to extend its original capabilities.

This numerical model focuses on the motion of the tip itself and the resulting aerodynamic forces from the tip motion. It does not include the rotor inboard section.

Other assumptions included in the numerical model are presented below.

1. Induced velocity is modeled in terms of a prescribed wake. Three types of prescribed wakes were used in the analysis, one being based on the uniform downwash, the other based on the nonuniform downwash, and the third also based on the nonuniform downwash but with strong higher harmonic terms. These wakes, which were prescribed in terms of inflow angle distributions, were obtained from various numerical models of a rotor with a conventional tip, and therefore do not reflect the aerodynamic loading on the free-tip. Also, they do not include any vortices shed from the junction of the tip and inboard section of the blade. These downwash distributions are presented in Figure 3-1 as inflow angle distributions.They include the wake induced velocity and the velocity induced by blade motions.

2. All aerodynamic parameters are based on the two dimensional blade element theory. However, the effect of planform geometry,

Figure 3-1 Inflow Angle Distribution.

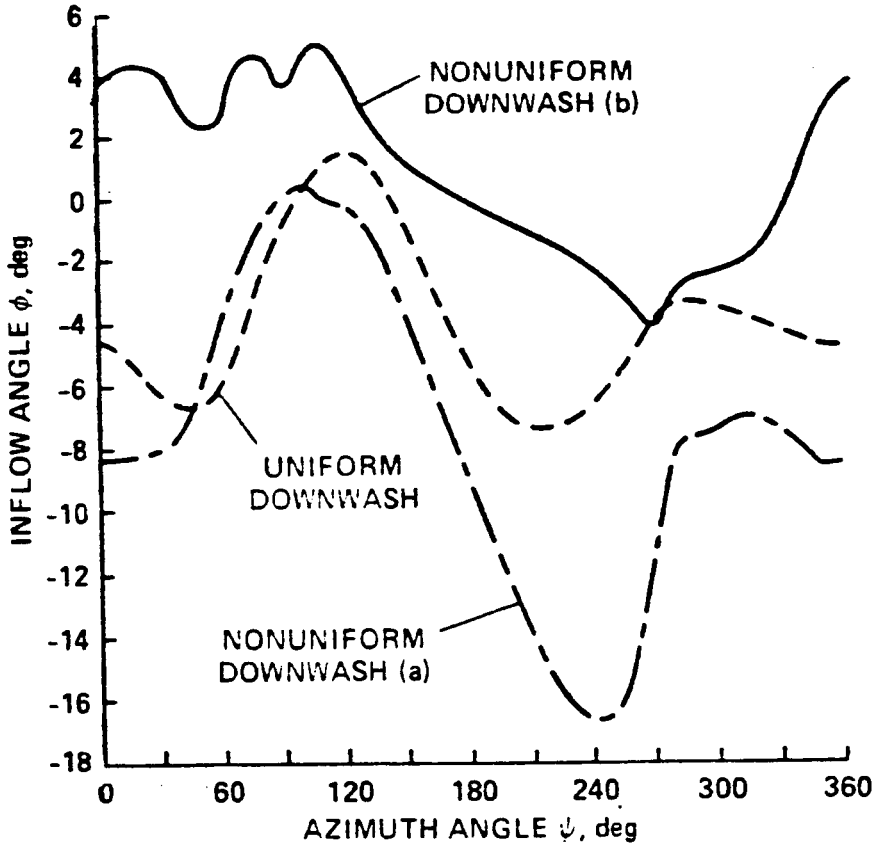

particularly, the effect of sweep, was accounted for in terms of a shift of the effective aerodynamic center. Although the numerical model was formulated as a two dimensional model, the actual aerodynamic data such as lift curve slope, were taken from the semi-span wind tunnel data. This enables the numerical model to make a more realistic simulation of the tip motion.

3. Although the compressibility compensation is included, it lacks a detailed description of the transonic phenomena associated with a shock wave. This compensation is strictly an approximation, which utilizes Prantl-Glauert similarity rule and polynomial approximation functions for c_{ℓ_α}, c_d and c_m.

4. Aerodynamic damping is the only unsteady effect that was included in the analysis. Unsteady-Quasi-Vortex-Lattice-Method was used to estimate the aerodynamic damping term. It was based on a fixed wing approximation with a sinusoidal oscillation, whose reduced frequency, k is approximately 0.22 (Reference 2).

5. The center of gravity of the tip is assumed to be on the pitch axis. This, by design, minimizes the moment of inertia of the tip.

Pitch angle of the tip is modeled as a dynamic response of a torsional vibration system around the pitch axis. Its equation of motion is;

$$J\frac{d^2\theta}{dt^2} + C(t)\frac{d\theta}{dt} + K(t)\theta = M(t) \qquad (3.1)$$

where

θ = tip pitch angle measured from the tip path plane.
J = moment of inertia of the tip
$C(t)$ = a sum of aerodynamic and mechanical damping rate
$= b_\alpha(t) + b_\theta(t)$
$K(t)$ = a sum of aerodynamic and mechanical spring rate
$= k_\alpha(t) + k_\theta(t)$
$M(t)$ = a sum of external moment

The external moment $M(t)$ includes the control moment, airfoil pitching moment, feathering moment and the moment due to friction.

The aerodynamic spring rate per unit span length, k_α is defined as;

$$k_\alpha = c_{\ell_\alpha} qc\Delta c \tag{3.2}$$

where c_{ℓ_α} is the sectional lift curve slope, q, local dynamic pressure, c, chord length and Δc is the offset of the effective aerodynamic center from the pitch axis. The values for c_{ℓ_α} and Δc were determined experimentally by a semi-span low subsonic wind tunnel test.

Tip pitch angle, θ, is defined in terms of angle of attack, α and inflow angle, ϕ which is prescribed in terms of Fourier coefficients D_n and F_n.

$$\theta = \alpha - \phi \tag{3.3}$$

$$\phi = \phi_0 + \sum_{n=1}^{10} [D_n \sin(n\Omega t) + F_n \cos(n\Omega t)] \tag{3.4}$$

where, Ω is the angular velocity of the blade.

Substituting above expressions into equation (3.1) and rearranging,

$$\frac{d^2\alpha}{dt^2} + \frac{b_\alpha + b_\theta}{J}\frac{d\alpha}{dt} + \frac{k_\alpha + k_\theta}{J}\alpha =$$
$$\frac{d^2\phi}{dt^2} + \frac{b_\alpha + b_\theta}{J}\frac{d\phi}{dt} + \frac{k_\alpha + k_\theta}{J}\phi + \frac{q_0}{J} + \frac{M_0}{J} + \frac{M_{fe}}{J} + \frac{M_f}{J} \quad (3.5)$$

where

$$\begin{aligned} q_0 &= \text{a constant control moment} \\ M_0 &= \text{aerodynamic moment} \\ &= c_m q c^2 \quad (3.6) \\ M_{fe} &= \text{feathering moment} \\ &= -\Omega^2(m_f \ell_f^2 + m_a \ell_a^2)\sin\theta \quad (3.7) \\ M_f &= \text{moment due to friction} \\ &= m\Omega^2 R\mu' \frac{\frac{d\theta}{dt}}{\left|\frac{d\theta}{dt}\right|} \quad (3.8) \end{aligned}$$

where, m_f, m_a, ℓ_f, ℓ_a are masses and moment arms which contribute to the feathering moment and m is the mass of the free tip, μ' is the equivalent friction coefficient and R is the radius of the rotor.

In equation (3.5) the initial conditions are unknown. Therefore, arbitrary starting values were assigned to α and $\frac{d\alpha}{dt}$. Then the equation was solved by the Runge-Kutta method. Since the initial conditions given initially are merely a guess, the Runge-Kutta method was iterated for each rotor revolution until a converged solution was obtained. The method converged very quickly and the solution was obtained in the second iteration.

This version of AZIMUTH program was superseded by a new version developed for FTR II analysis. The new version of AZIMUTH is called FTR2 and it is described in section 4.

For the analysis of hovering mode, a half sine wave was prescribed for the inflow angle to simulate an air jet. All parameters were the same as those in the analysis of the forward flight mode. The inflow angle is given

by the following equation;

$$\phi = \phi_{peak} \sin\left(\frac{\psi - \frac{\pi}{2}}{\frac{2\pi}{3} - \frac{\pi}{2}}\pi\right) \quad \text{when} \quad \frac{\pi}{2} \leq \psi \leq \frac{2\pi}{3}$$
$$\phi = 0 \quad \text{otherwise} \tag{3.9}$$

where

$$\phi_{peak} = \frac{\pi}{60} \tag{3.10}$$

A special version of AZIMUTH program, HOVER was developed for the analysis and its program listing is available on request.

3.2. Aerodynamic Parameters.

The following rotor parameters were selected for the analysis.

$$\begin{aligned} \text{Radius} &= 28.0\ ft \\ \text{Average Chord} &= 1.3667\ ft \quad \text{for a rectangular tip} \\ &= 1.2657\ ft \quad \text{for a swept-tapered tip} \\ \text{Average Tip Speed} &= 650.0\ ft/sec. \\ \text{Forward Flight Speed} &= 325.25\ ft/sec. \\ \text{Advance Ratio} &= 0.5 \end{aligned}$$

For feathering moment,

$$\begin{aligned} m_f &= 0.0445\ slug/ft \\ m_a &= 0.0445\ slug/ft \\ \ell_f &= 0.0205\ ft \\ \ell_a &= 0.2297\ ft \end{aligned}$$

Two planforms, rectangular and swept-tapered, were used and they are shown in Figure 3-2. In both cases, the center of gravity of

Figure 3-2 Free-Tip Planform

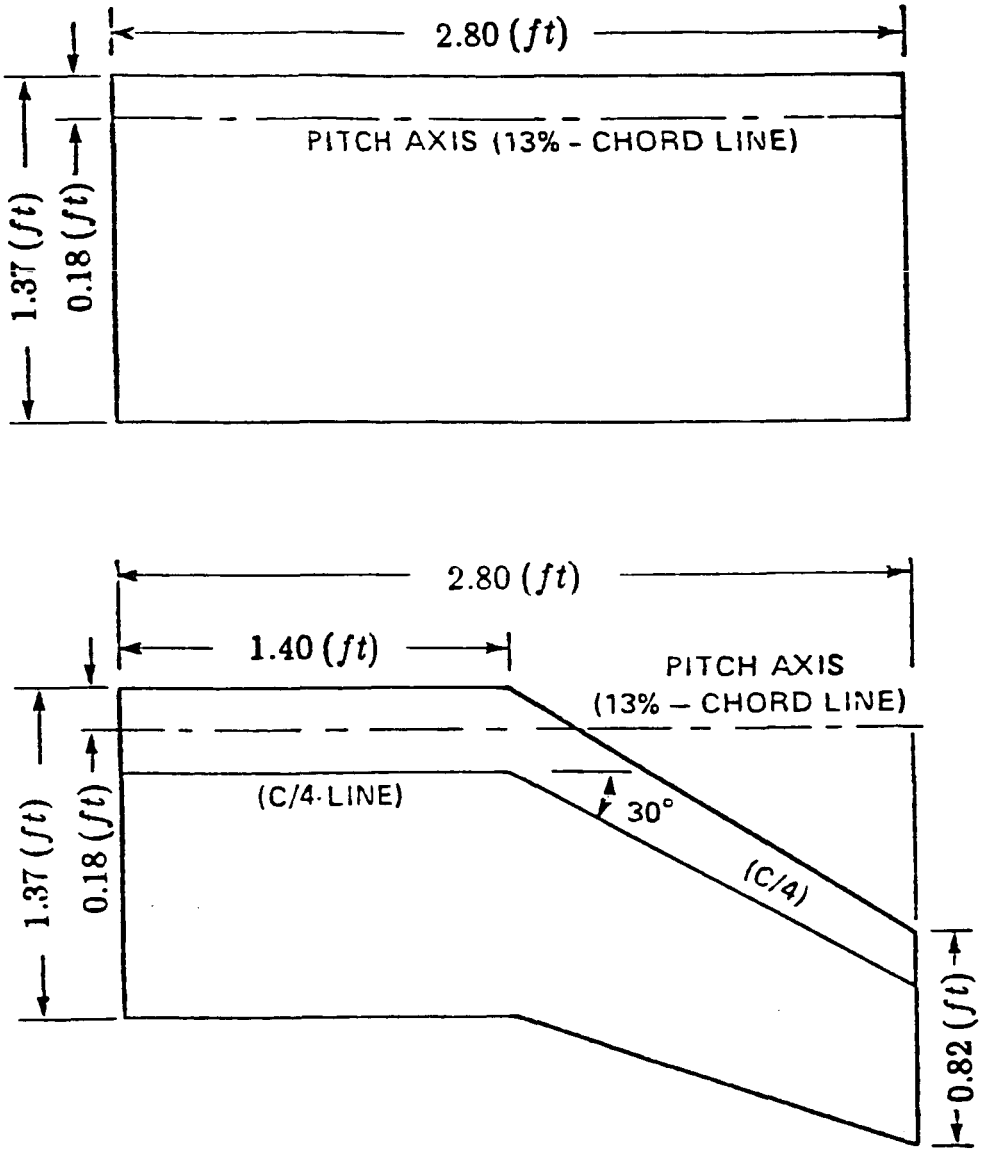

the tip and the pitch axis were assumed to be at 13 % chord location.

The basic aerodynamic characteristics of these tips were obtained by a semi-span wind tunnel test in the Ames 7- by 10-foot Wind Tunnel. Figures 3-3 and 3-4 shows the lift and moment around 25 % and 13 % chord as functions of angle of attack for the two planforms. The airfoil used in the test was Boeing Vertol V23010-1.58. The discussion on this airfoil will be given in section 4. The offset of the effective aerodynamic center from the pitch axis, Δc, was computed from $c_{m_{a.13}}$ by the equation;

$$\Delta c = \frac{c_{m_{a.13}}}{c_{L_a}} \tag{3.11}$$

where

c_{L_a} = lift curve slope

3.3. Results.

3.3.1. Forward Flight

In forward flight, the behavior of the Free-Tip is basically a torsional vibration of the mass (the tip) around its pitch axis with nonconstant damping and spring rate. Since the pitch angle of the tip is determined by the response characteristic of this vibration, the resulting lift loading around the azimuth is very different from a conventional tip, which has a prescribed pitch angle. A typical lift distribution of the Free-Tip, together with the lift on a conventional tip are presented in Figure 3-5. The lift distribution on a Free-Tip was computed for the swept, tapered tip with nonuniform downwash (a) and airfoil pitching moment being $c_{m_0} = -0.01$. The ability of the Free-Tip configuration to suppress the oscillatory lift is evident.

Figure 3-3 Aerodynamic Characteristics of Rectangular Tip.

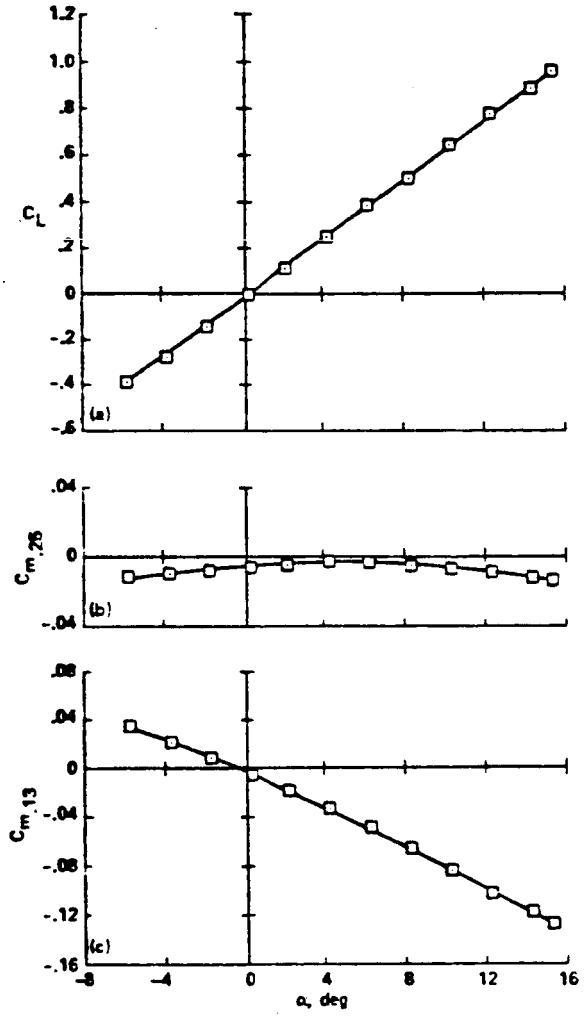

Figure 3-4 Aerodynamic Characteristics of Swept, Tapered Tip.

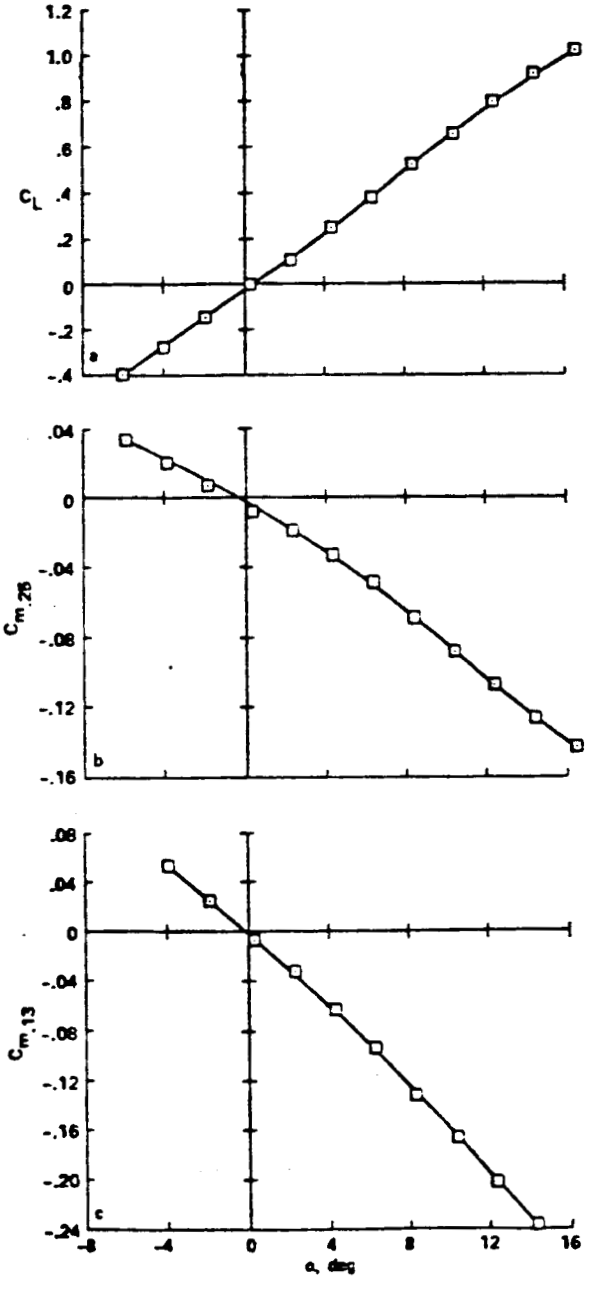

Figure 3-5 A Typical Lift Distribution on a Free-Tip and a Conventional Tip.

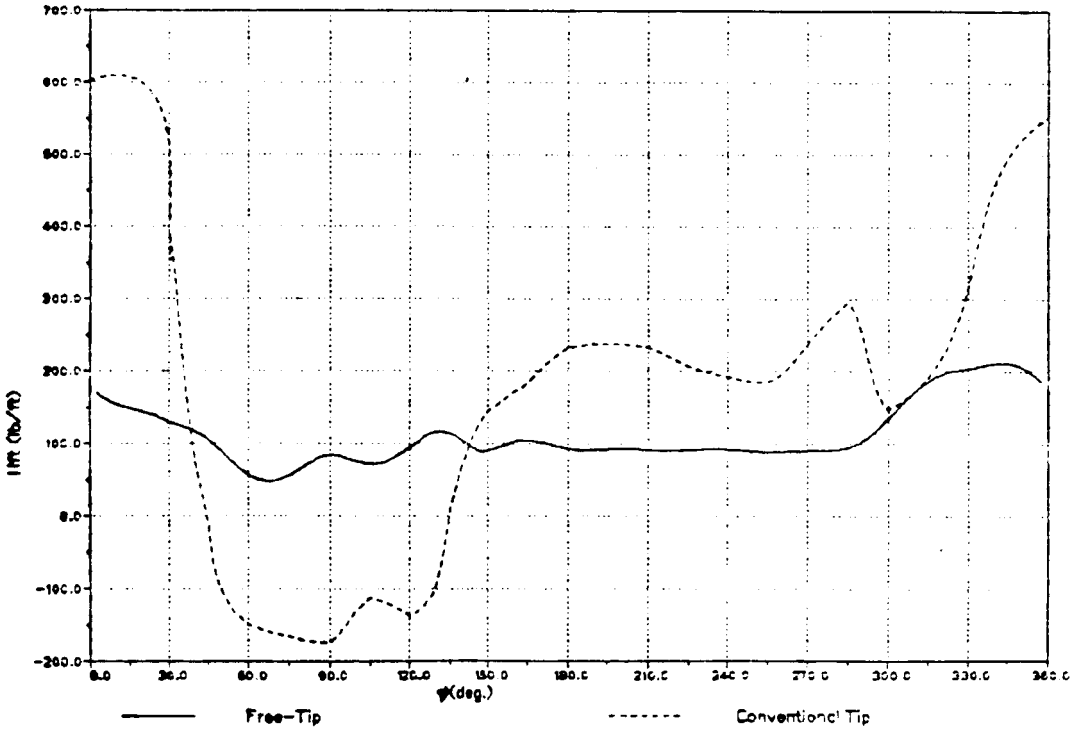

The performance criteria used in this parametric study were, primarily, peak-to-peak amplitude of the lift oscillation, with the mean lift level as a secondary factor.

Figures 3-6 and 3-7 show the peak-to-peak lift amplitude for both the rectangular and the swept, tapered planforms with three levels of moment inertia and control moment.

It was shown that the resulting lift oscillations were relatively insensitive to the level of moment of inertia. The moment of inertia used in this analysis was the "effective moment of inertia", which includes the tip, the shaft of the pitch axis and a contribution from the controller mechanism which generates the control moment. A typical effective moment of inertia for a unit span length is 0.03 $slug\,ft^2/ft$.

The rectangular planform generated considerably higher peak-to-peak lift than the swept tapered configuration for the same mean lift level. The major reason for this was the low aerodynamic spring rate that caused a low undamped natural frequency and resulted in a system whose response to the angle of attack variation is slow. The response can be improved by increased aerodynamic spring rate by shifting the aerodynamic center downstream, creating a larger offset from the pitch axis. This can be done by sweeping back the tip planform.

The aerodynamic spring, created by the aerodynamic moment and the lift offset, is proportional to the square of the local flow velocity and the aerodynamic damping is considered to be proportional to the local flow velocity. Therefore, it is impossible to achieve an optimal response at all azimuth location. In fact, the unsteady lifting surface theory (Reference 2) predicted that the aerodynamic damping alone is large enough to make the system slightly underdamped in the advancing side and heavily overdamped on the retreating side. This makes adding a mechanical damper to adjust the damping characteristics impractical. It also implies that any damping which is inherent in the mechanical system should be eliminated as much as possible. If, however, the lift oscillations on

Figure 3-6 Peak-to-Peak Lift for Rectangular Tip.

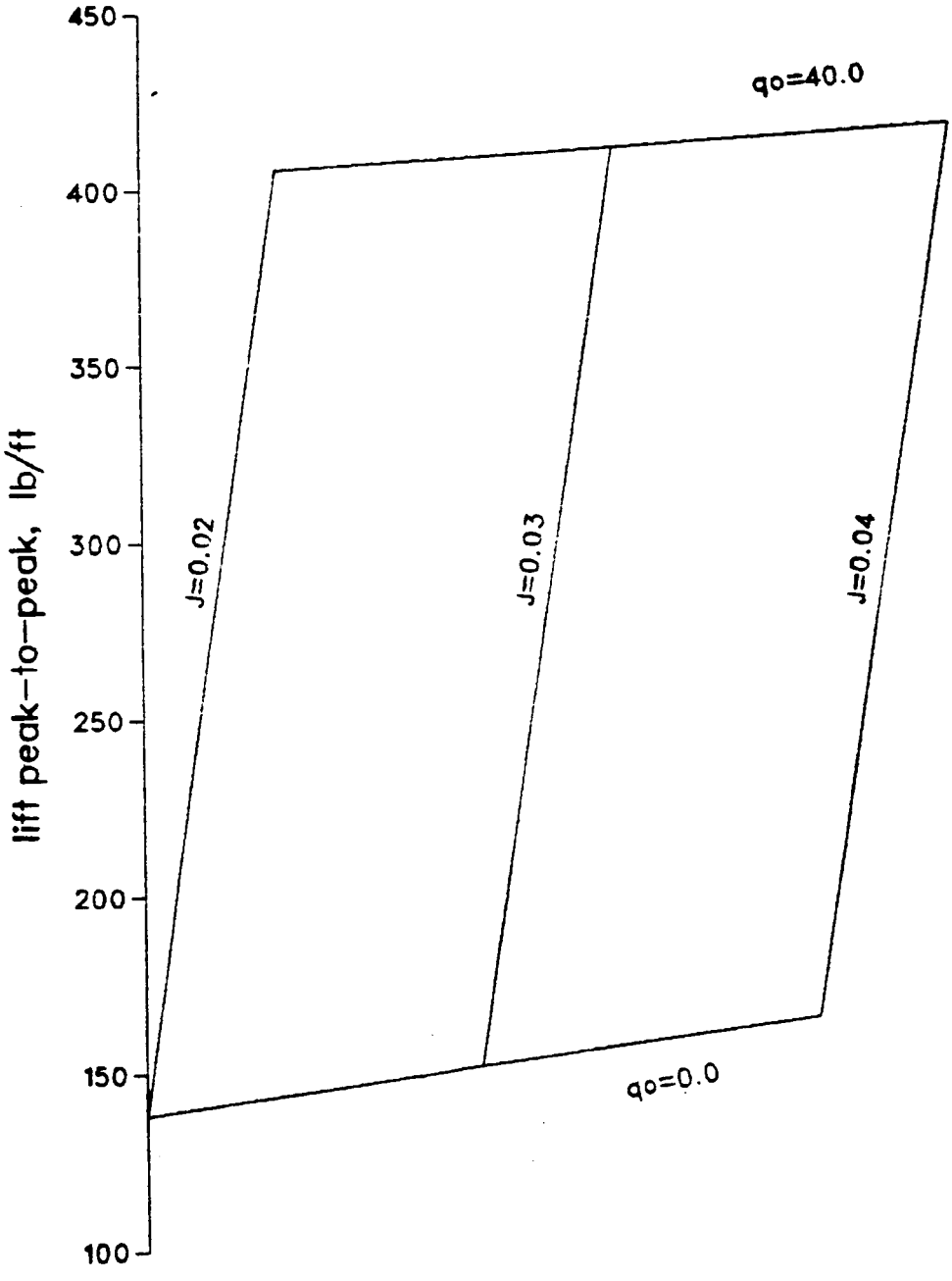

Figure 3-7 Peak-to-Peak Lift for Swept, Tapered Tip.

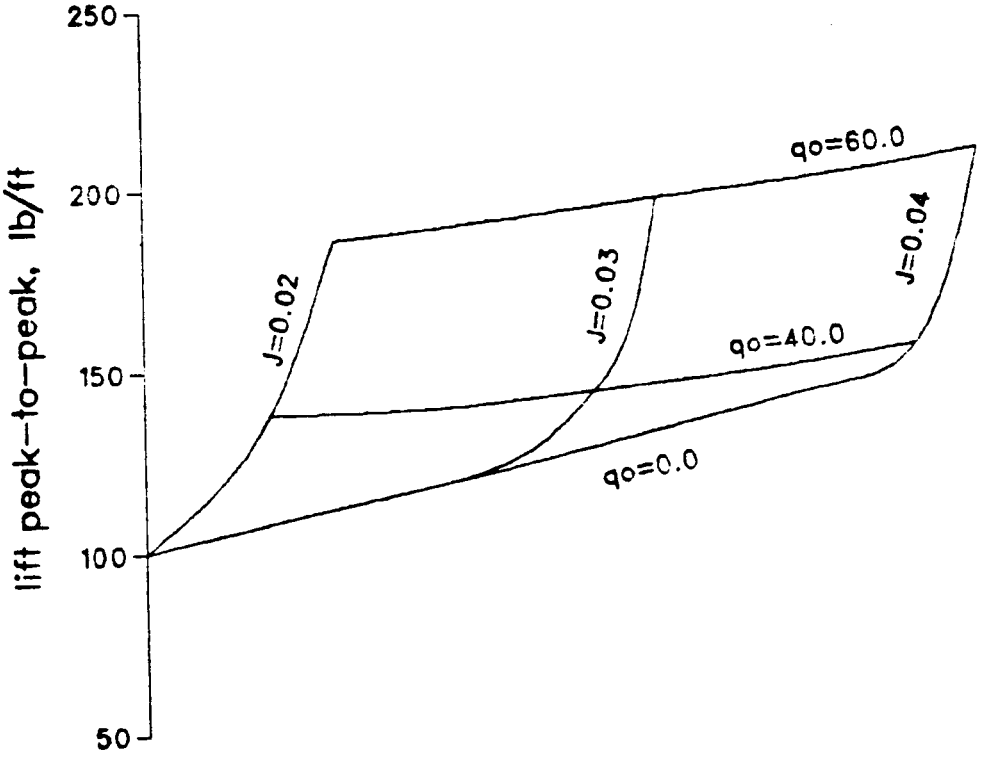

the advancing side become large and dominant, then adding a mechanical damper to achieve the critical damping on the advancing side may be attractive.

Because of the above stated overdamping situation on the retreating side, the tip is unable to increase its pitch angle fast enough to respond to the rapidly decreasing dynamic pressure, q, prior to the azimuth location of $\psi = 270^o$ and fails to respond to the dynamic pressure build-up beyond $\psi = 270^o$. This results in a low lift loading around $\psi = 240^o$ and a high lift loading around $\psi = 300^o$. This phenomenon may be called q-effect and is shown in Figure 3-5. Usually the peak-to-peak lift due to the q-effect overshadows the lift peaks on the advancing side due to the underdamped oscillation.

The amount of control moment determines the mean lift loading. However, if an excessive control moment is applied to the tip, it brings the tip pitch angle to a high value around $\psi = 270^o$, so that it takes a longer time for a tip to respond to the dynamic pressure build-up after passing $\psi = 270^o$. As a result, the peak-to-peak lift becomes larger as the control moment becomes higher. This phenomenon becomes more significant on the rectangular tip because it has a lower aerodynamic spring.

An increased control moment can also bring the airfoil close to the stall condition, which cannot be predicted by the AZIMUTH program.

As it is indicated in Figure 3-5, for this particular configuration, the minimum lift occurs on the advancing side due to the oscillatory motions. This part of the lift can be increased by the airfoil pitching moment coefficient c_{m_0}, because the aerodynamic moment is proportional to the local dynamic pressure, which becomes maximum at $\psi = 90^o$ and minimum at $\psi = 270^o$, Thus because of c_{m_0}, a cyclic pitch is developed to increase the lift on the advancing side without any appreciable impact on the retreating side.

For example, Figure 3-8 shows an identical configuration which yields the lift distribution in Figure 3-5, but the pitching moment coefficient of the airfoil around the 25 % chord was changed from -0.01 to $+0.01$. The positive pitching moment coefficient brings up the mean lift level without deteriorating, if not improving, the peak-to-peak lift characteristics. On the other hand, Figure 3-9 shows the situation in which the tip is carrying a large lift on the advancing side. This lift peak can be brought down by reducing the airfoil pitching moment. In other words, the lift level on the advancing side can be fine-tuned by the airfoil pitching moment.

Mechanical friction is also a key element in the behavior of the Free-Tip because it can inhibit the tip to respond to flow perturbations and cause a considerable oscillation in the resultant lift. This is shown in Figure 3-10. If the Free-Tip is supported by a pitch mechanism involving a surface contact perpendicular to the centrifugal force vector acting on the tip, the Free-Tip performance will be severly degraded because the friction coefficient for the surface contact averages at 0.03 to 0.04. Note that the peak-to-peak lift, $\ell_{pp} \approx 800\ (lb/ft)$ at $\mu' = 0.04$ corresponds to the peak-to-peak lift of a conventional tip (Figure 3-5). Boeing Vertol performed a wind tunnel test of FTR I utilizing a controller involving such a surface contact in 1981. (This controller configuration will be shown in section 4.) The results showed that the large friction can inhibit the tip from responding to the disturbances (Reference 3). Thus, friction must be minimized.

The tip response to the three effective inflow models are shown in Figures 3-11 through 3-13. The basic characteristic of the lift response seems to be the same for all three models. The only significant difference is the higher harmonic lift oscillations between $\psi = 0^o$ and $\psi = 120^o$, which is a characteristic of the nonuniform downwash (b), shown in Figure 3-1.

The Free-Tip system involves two kinds of spring. One is aerodynamic and the other is mechanical which can be artificially added to the system. It has been shown that a large aerodynamic spring, which can be achieved by sweeping back the tip, is desirable for a better response.

Figure 3-8 Effect of Airfoil Pitching Moment Coefficient.

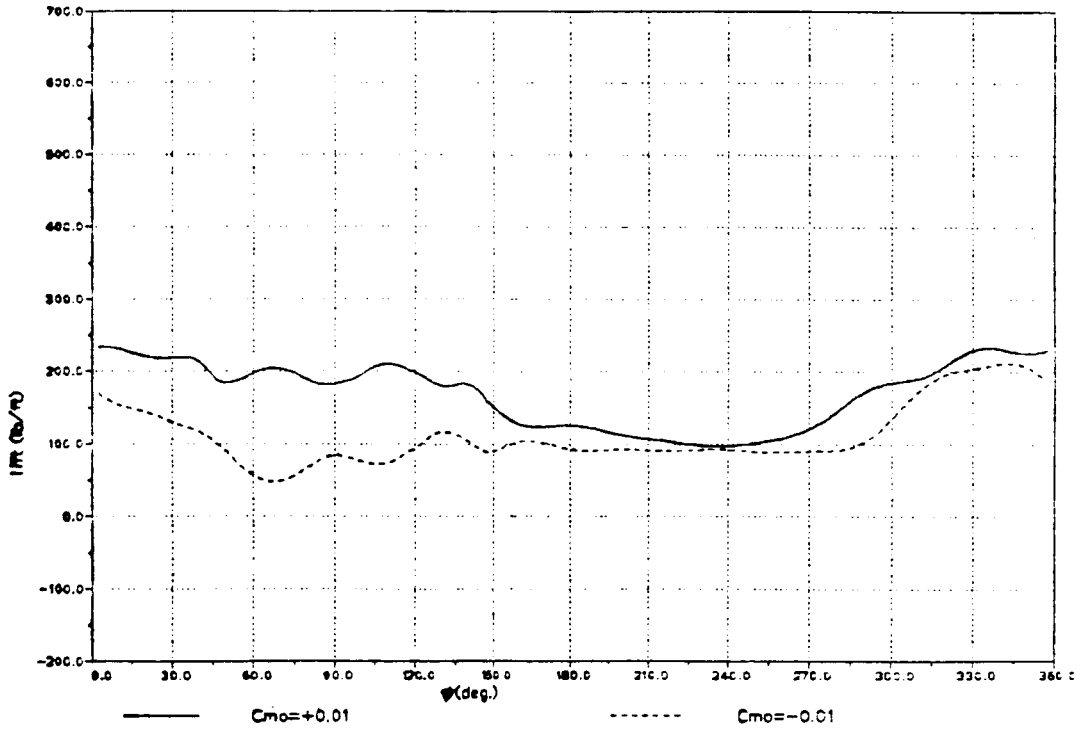

Figure 3-9 General Trend of Airfoil Pitching Moment Coefficient Effect.

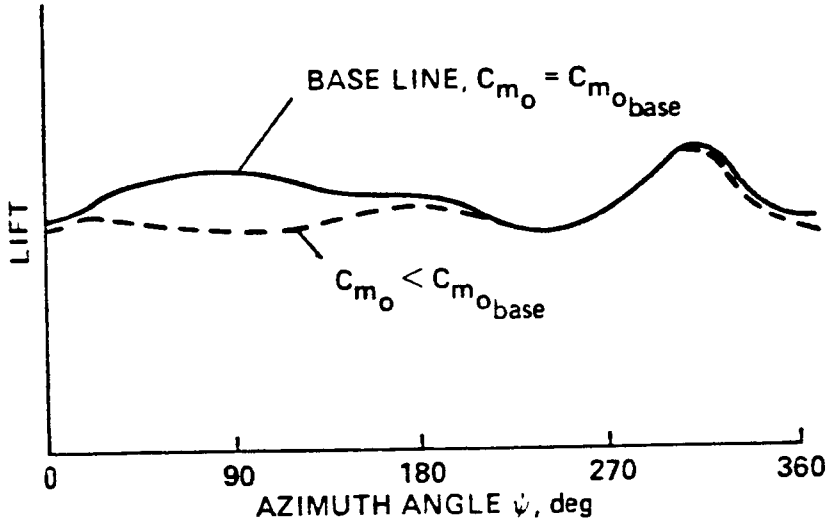

Figure 3-10 Effect of Friction

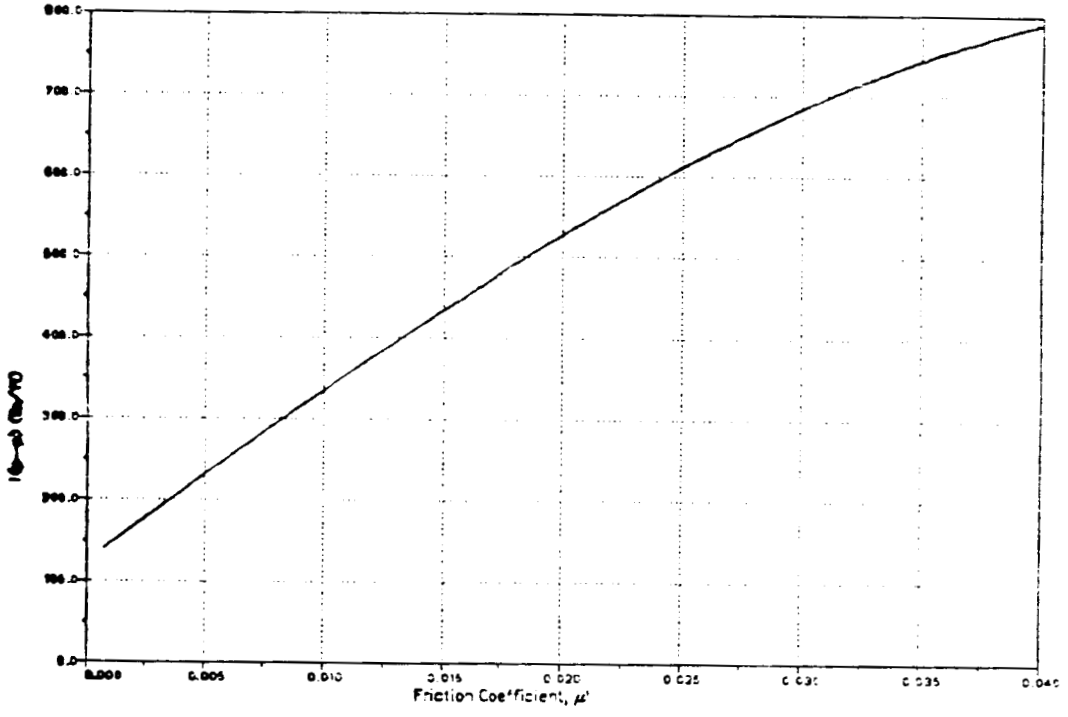

Figure 3-11 Lift Distribution on the Swept, Tapered Tip with Nonuniform Downwash (a).

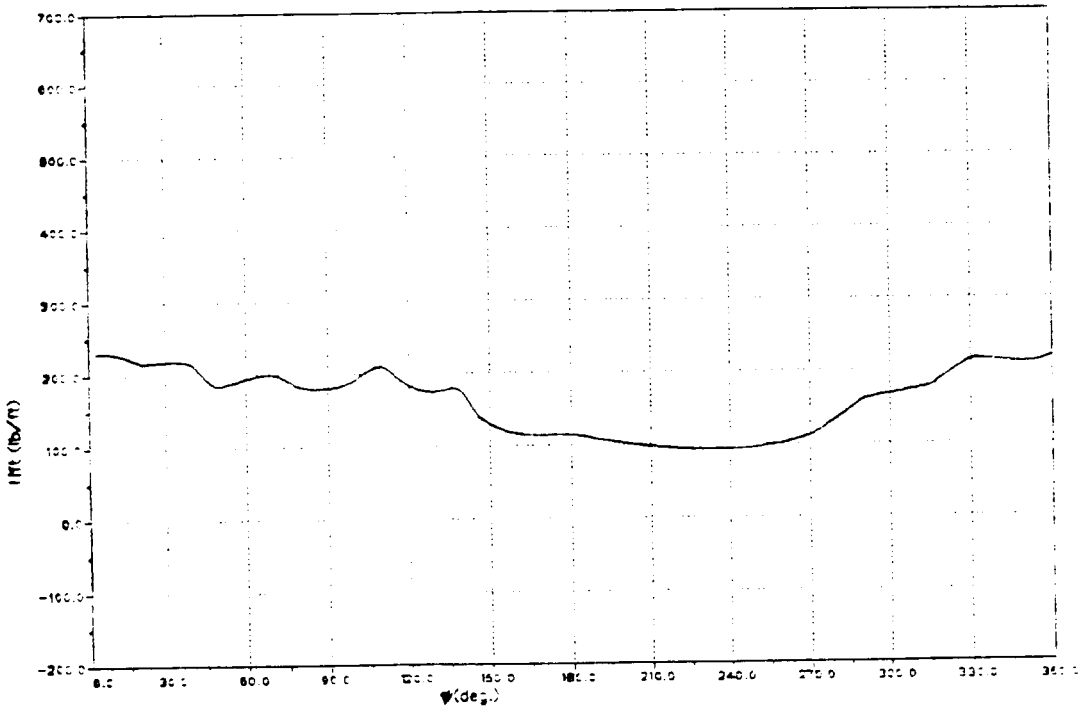

Figure 3-12 Lift Distribution on the Swept, Tapered Tip with Uniform Downwash.

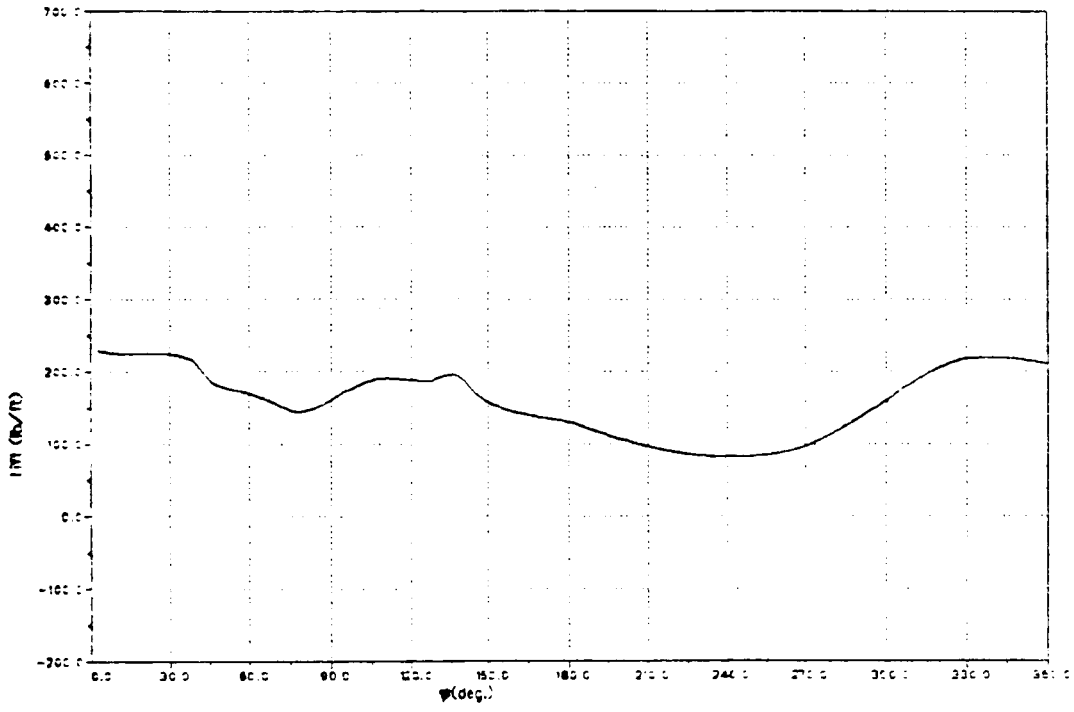

Figure 3-13 Lift Distribution on the Swept, Tapered Tip with Nonuniform Downwash (b).

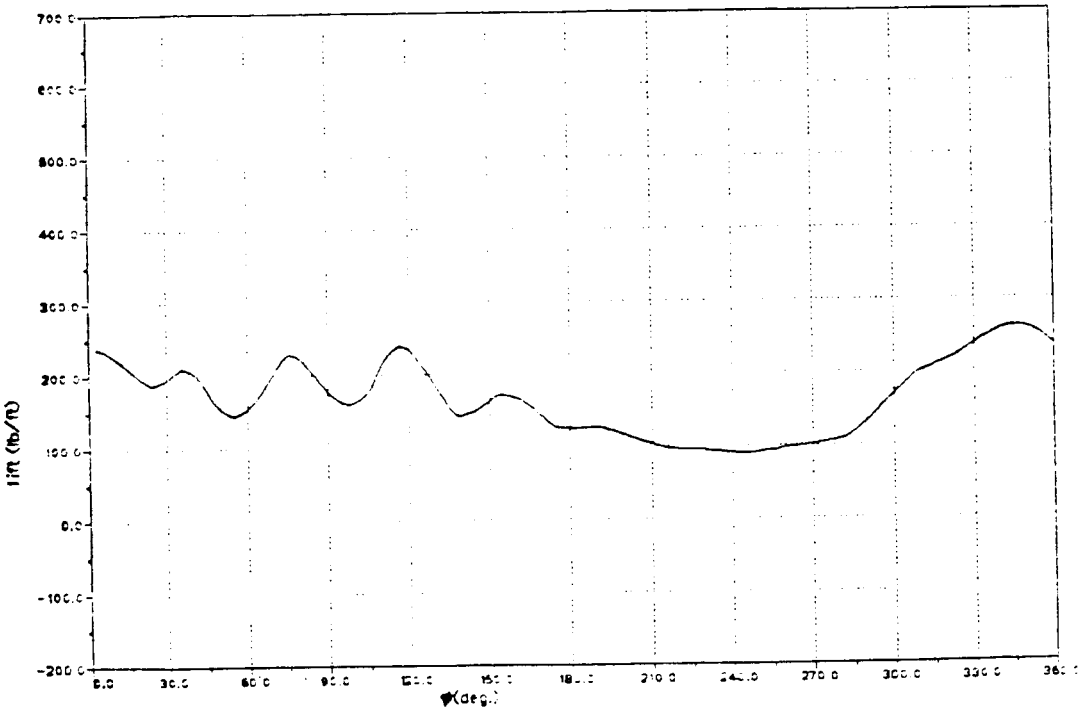

The mechanical spring also has a large impact on the tip response. Its effect on the amplitude of the lift oscillation is presented in Figures 3-14 and 3-15. These figures show that the mechanical spring with excessive spring rate will degrade the tip performance. However, the system can tolerate a small mechanical spring rate which may be inherent in the design of a controller.

In fact, a mechanical spring with a low spring rate and a large pretwist can replace the constant moment controller. The moment from the spring stays relatively constant in the range of the tip motion, since the tip motion is restricted in approximately $\pm 10^o$, which is much smaller than the pretwist. Figure 3-16 shows the peak-to-peak lift on the Free-Tip controlled by a mechanical spring with various spring rate/pretwist combinations. The spring rate and pretwist were adjusted so that their combination always yields 40 $ft\ lb/ft$ moment when the tip pitch angle is zero relative to the blade inboard section.

3.3.2. Hover

Figure 3-17 shows a lift distribution resulting from a response of the swept tapered tip to an air jet. This response is the expected response for this system, a rise in pitch angle with a damped oscillatory return. Note that the perturbation starts at $\psi = 90^o$ and ends at $\psi = 120^o$.

3.4. Conclusions.

Both of the rectangular and the swept tapered configurations used in the present study generated less mean lift than a conventional tip. However, they successfully eliminated the negative lift on the advancing side. They also showed a drastic reduction in amplitude of lift oscillation (peak-to-peak lift), which is a source of vibration.

Figure 3-14 Effect of Mechanical Spring, Swept, Tapered Tip, $c_{m_0} = -0.01$.

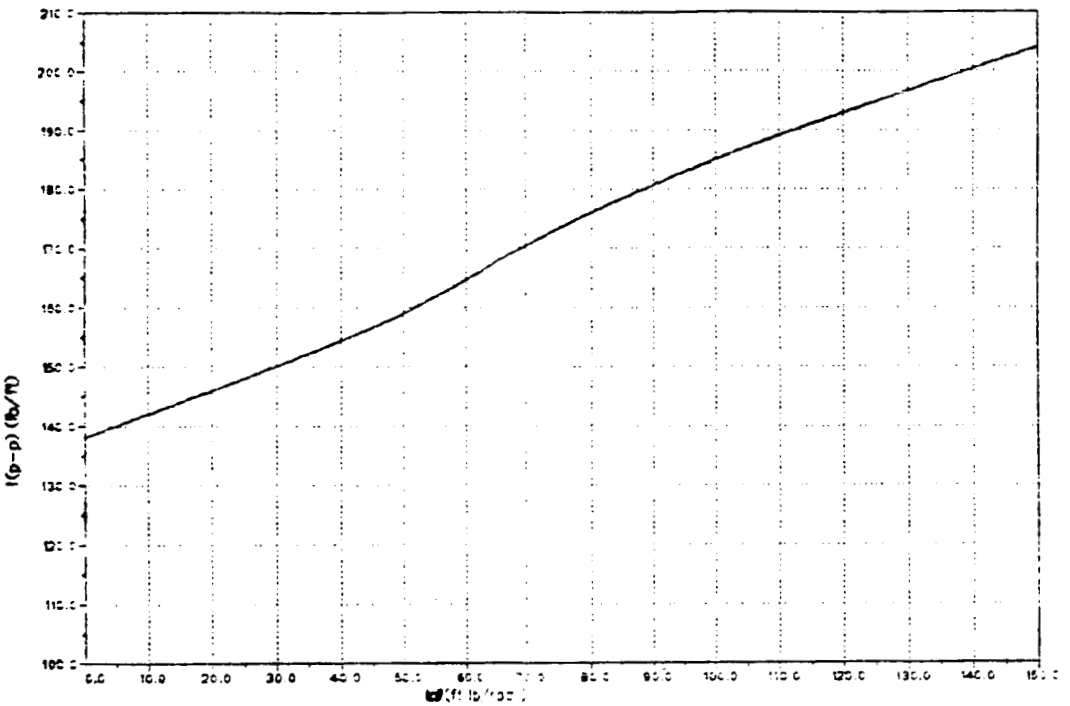

Figure 3-15 Effect of Mechanical Spring, Swept, Tapered Tip, $c_{m_0} = +0.01$.

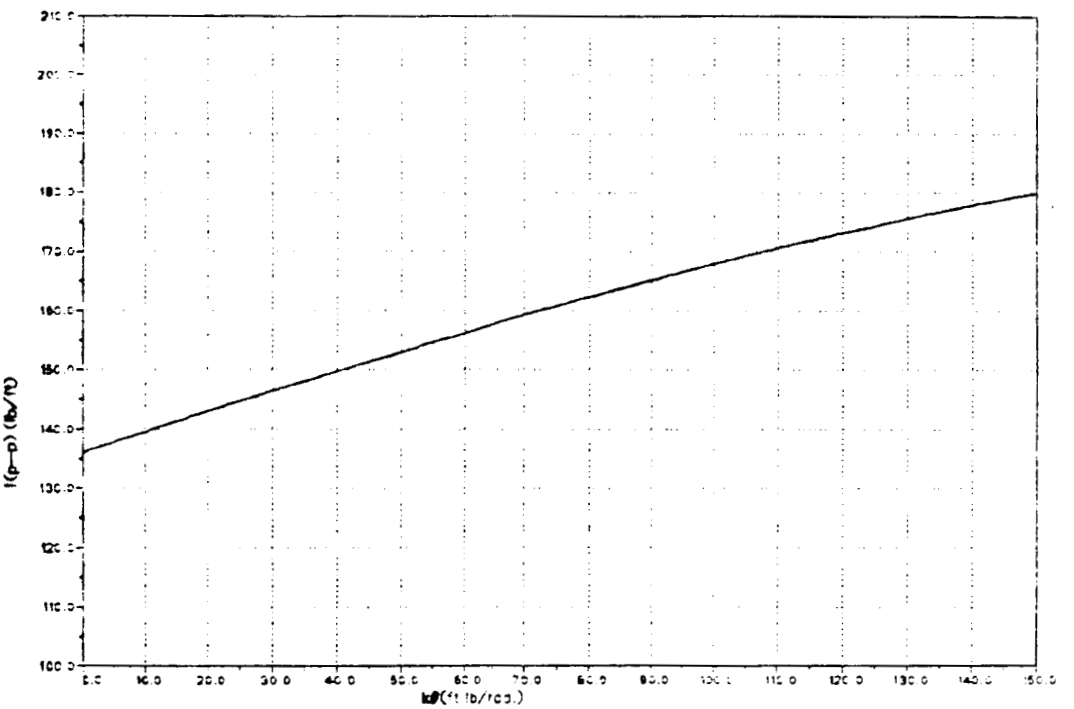

Figure 3-16 Spring Controller, $c_{m_0} = +0.01$.

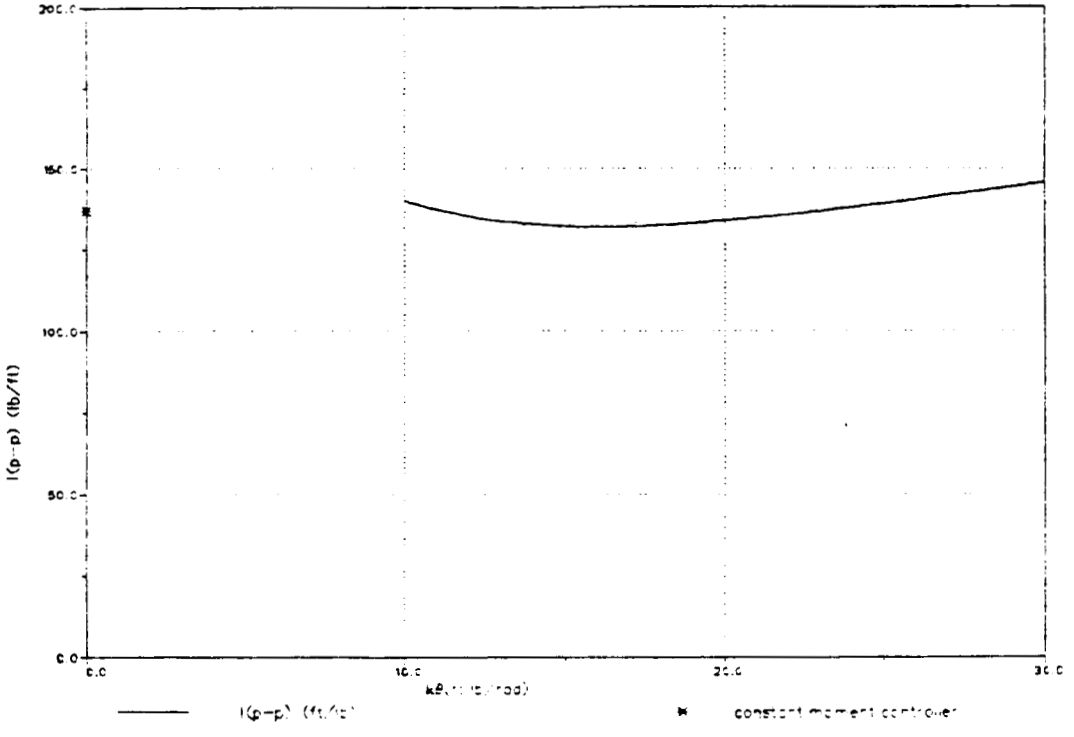

Figure 3-17 Tip Response to an Air Jet.

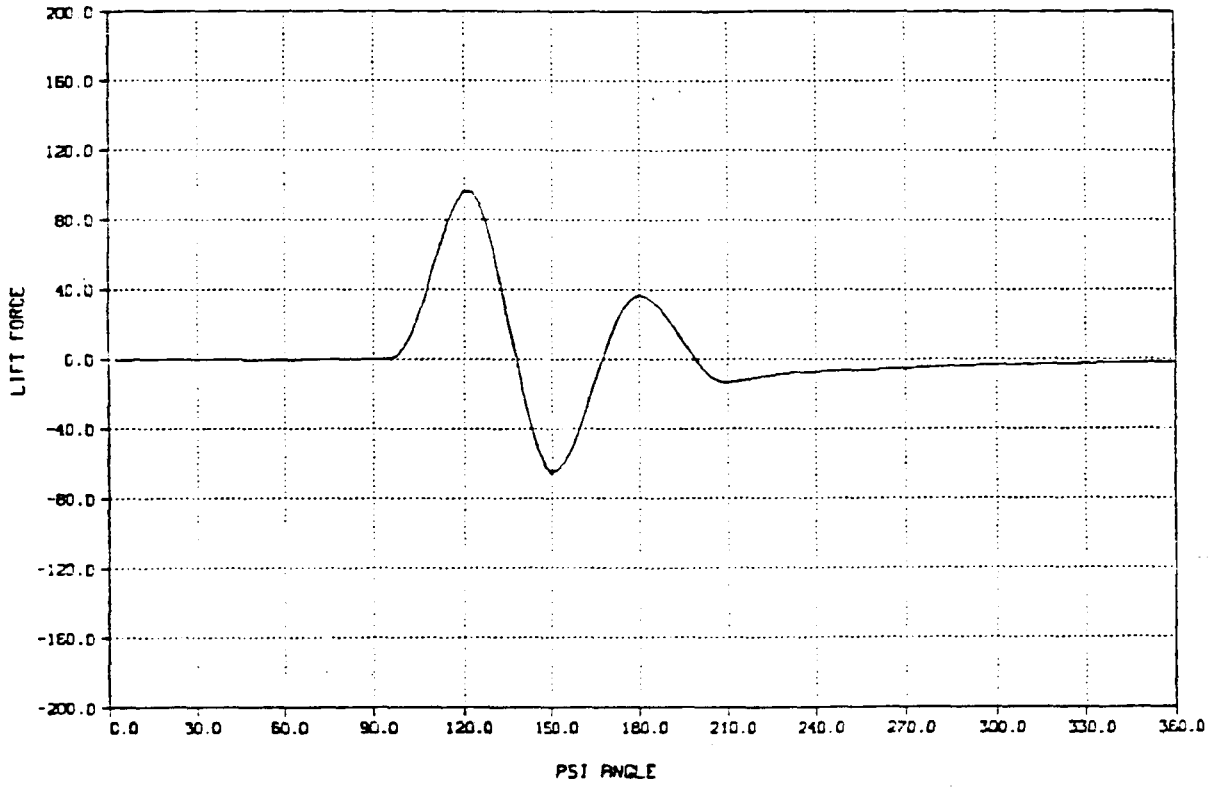

In general, low inertia, and high aerodynamic spring constant, i.e., a large sweep angle, are desirable. In forward flight, one has to define the optimal and suboptimal regions for damping, namely, whether the damping should be optimized on the advancing side or on the retreating side, since it is impossible to achieve the best damping characteristics in all azimuthal locations. Because a lift peak on the retreating side due to the q-effect tends to dominate the oscillatory motions on the advancing side, it is more important to suppress this q-effect by reducing the mechanical damping than to damp out the oscillatory motions on the advancing side.

Friction must be also minimized for effective oscillatory lift suppression. Small positive aerodynamic pitching moment on the airfoil is also desirable for a high mean lift level for the present configurations.

A mechanical spring with a large spring rate degrades the tip performance. However, if the combination of small spring rate and a large pretwist can be obtained, it can replace the constant moment controller.

4. Two Dimensional Analysis of FTR II

4.1. Numerical Model Description.

The numerical model developed for FTR I analysis was used for the FTR II analysis. Since the dihedral effect must be considered, an additional term was included in the external moment.

Equation (2.5) is now rewritten as

$$\frac{d^2\alpha}{dt^2} + \frac{b_\alpha + b_\theta}{J}\frac{d\alpha}{dt} + \frac{k_\alpha + k_\theta}{J}\alpha = \frac{d^2\phi}{dt^2} + \frac{b_\alpha + b_\theta}{J}\frac{d\phi}{dt} + \frac{k_\alpha + k_\theta}{J}\phi + \frac{q_0}{J} + \frac{M_0}{J} + \frac{M_{fe}}{J} + \frac{M_f}{J} + \frac{M_{dh}}{J} \quad (4.1)$$

here, M_{dh} is the moment due to dihedral, which is defined as

$$M_{dh} = D\frac{\ell_{tip}\sin\Gamma}{2}\cos\theta \quad (4.2)$$

where

D = sectional drag on the tip
ℓ_{tip} = tip length
Γ = dihedral angle, positive down

The program with the above modification supersedes the old version on AZIMUTH, and now called FTR2, and the program listing is available on request.

4.2. Aerodynamic Parameters.

All aerodynamic parameters used in the FTR I analysis remain the same.

In addition to these parameters, a relatively large pitching moment increment, Δc_{m_0} was introduced. It ranges from -0.10 to 0.00. It is assumed that this moment was created with a deflection of a small tab at the trailing edge of the tip, resulting in a minimum change in lift and drag characteristics. Therefore, no drag penalty nor lift characteristic change was applied to the model.

The dihedral was assumed to start at the root end of the tip section and the dihedral angle, Γ ranges from -30^o to 0^o.

The inflow angle distribution used for this analysis is the nonuniform downwash (a) shown in Figure 3-1.

4.3. Results.

The performance criterion used in this analysis is the magnitude of longitudinal cyclic control moment (rolling moment) produced by the tip. Its contribution to the lateral cyclic control moment (pitching moment) is also carefully monitored to determine if there is any appreciable effect. The longitudinal cyclic control moment $\mathcal{L}$ was computed as follows.

$$\mathcal{L} = \int_0^{2\pi} \ell(\psi) R_{tip} \sin(\psi) d\psi \tag{4.3}$$

where

$\ell(\psi)$ = sectional lift at ψ (lb/ft)
R_{tip} = radial location of the tip (ft)
ψ = azimuth angle $(rad.)$

Since the first harmonic term of the lift oscillation has the strongest influence on the overall longitudinal cyclic moment, the contribution from

the first harmonic term alone was also computed separately by the following equation;

$$\mathcal{L}_1 = \int_0^{2\pi} \ell_1(\psi) R_{tip} \sin(\psi) d\psi \tag{4.4}$$

where

$$\ell_1(\psi) = a_1 \cos\psi + b_1 \sin\psi \tag{4.5}$$

where a_1 and b_1 are obtained from the harmonic analysis of the lift distribution, $\ell(\psi)$.

In any case, the analysis shows that the contribution from the higher harmonic terms to the longitudinal cyclic control moment is negligible, since the difference between $\mathcal{L}$ and $\mathcal{L}_1$ is always less than 0.01 % of $\mathcal{L}$. The reason why the difference between $\mathcal{L}$ and $\mathcal{L}_1$ is so small is that the "ripples" in the lift distribution due to higher harmonic terms tend to cancel each other when the moment is integrated over the azimuth angle to yield the total longitudinal cyclic control moment.

The moment generated by the dihedral and the airfoil pitching moment is a function of local dynamic pressure, which is a linear function of the tip velocity squared. Therefore, it contains a second harmonic component as shown below.

Using a nondimensional variable for the tip velocity, referred to the rotational tip speed ,ΩR, it can be shown that

$$v_{tip} = 1 + \mu \sin(\Omega t) \tag{4.6}$$

where, μ is the advance ratio and Ω is the angular velocity of the rotor. Then

$$v_{tip}^2 = 1 + 2\mu \sin(\Omega t) + \frac{\mu^2}{2}[1 - \cos(2\Omega t)] \tag{4.7}$$

The last term in the above equation represents the second harmonic component. Since the advance ratio, μ is normally less than 1, the second

harmonic term is always one order smaller than the first harmonic component. However, a harmonic analysis of the lift distribution on the tip was performed to verify its effect.

Figures 4-1 through 4-3 show the resulting lift on a rectangular tip for various Δc_{m_0}. A bar chart for the harmonic coefficients is also included in each figure. They clearly show the potential advantage of Free-Tip to produce the cyclic control moment. Figures 4-4 though 4-6 show the lift on a swept, tapered tip for various Δc_{m_0} Both configurations show a large once-per-revolution lift oscillation, which will result in a longitudinal cyclic moment, as Δc_{m_0} increases. Since the swept, tapered tip has a larger aerodynamic spring, its amplitude of the lift oscillation for a given Δc_{m_0} is smaller than that of the rectangular tip. From this point of view, the rectangular tip is more favorable for FTR II configuration because of its higher potential to generate the longitudinal cyclic moment. Note that the higher harmonic components as well as the first harmonic cosine term (lateral cyclic control moment) are considerably smaller than the first harmonic sine component (longitudinal cyclic control moment).

The amount of longitudinal control moment, $\mathcal{L}$ due to Δc_{m_0} on the rectangular tip is presented in Figure 4-7. It shows that the longitudinal cyclic moment increases almost in a linear fashion with Δc_{m_0}. Although high Δc_{m_0} is desirable to generate a high longitudinal cyclic moment, such a large tab deflection may cause a large drag penalty, which is being ignored in this analysis. This problem can be solved easily by the use of a uniform loading type airfoil, such as a supercritical airfoil. Such airfoils generates a significant negative pitching moment without a trailing edge tab, and their drag characteristics are generally better than a conventional airfoil, especially in high subsonic region.

Effect of dihedral angle on the longitudinal cyclic control moment is presented in Figure 4-8. It is clear that the dihedral is much less effective than the airfoil pitching moment. There are two reasons for the dihedral to be not very effective. First, the drag on the airfoil is already minimized. Therefore, as a result, the desired pitching moment

Figure 4-1a Lift Distribution, Rectangular Tip, $\Delta c_{m_0} = 0.00$.

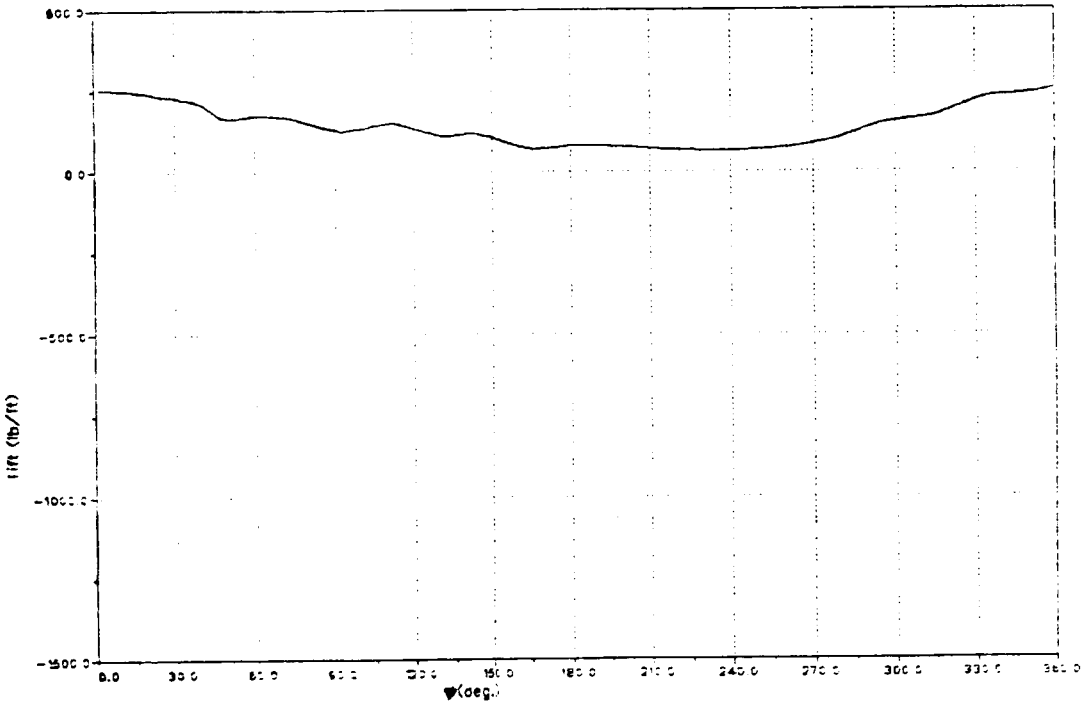

Figure 4-1b Harmonic Contents.

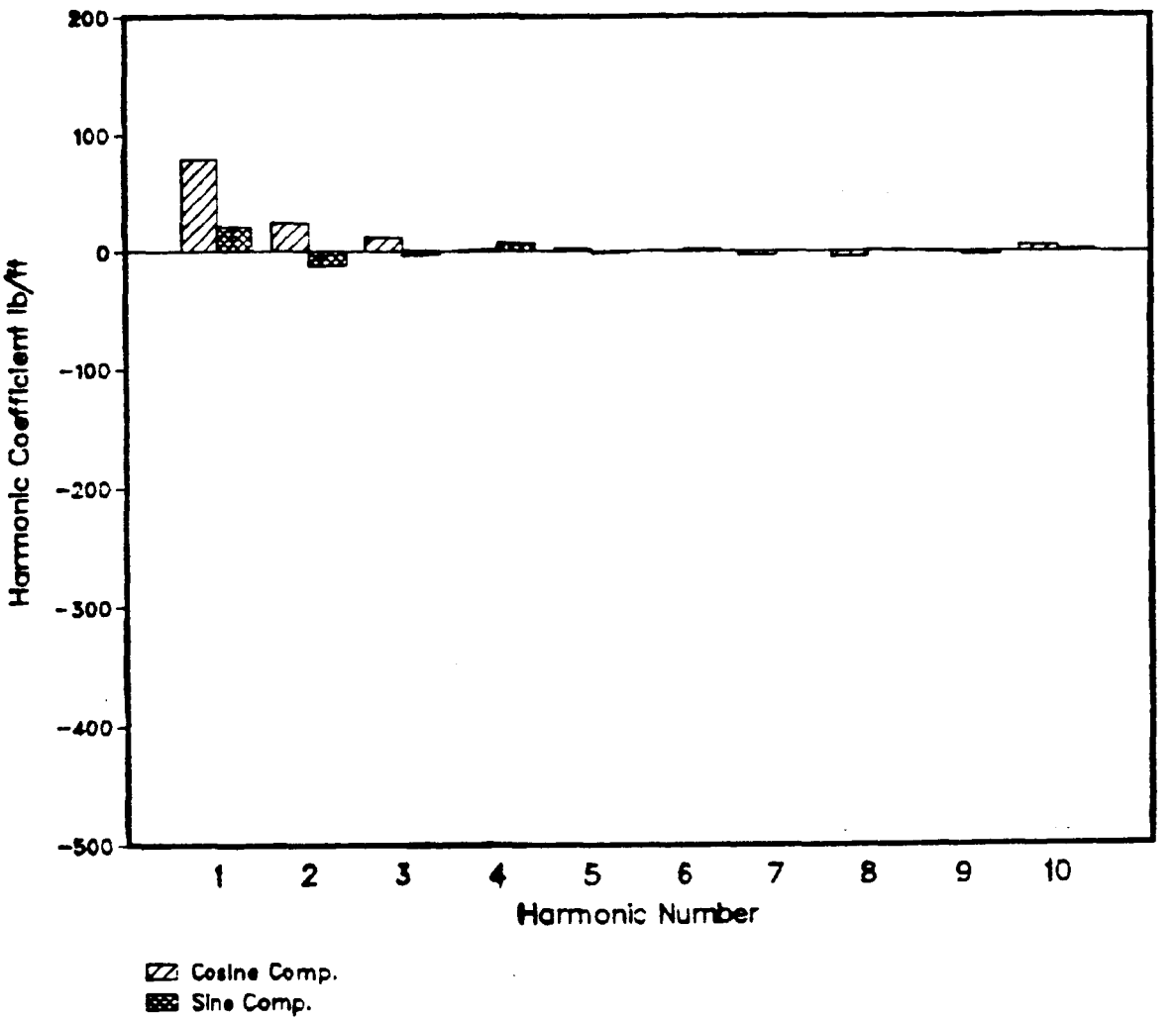

Figure 4-2a Lift Distribution, Rectangular Tip, $\Delta c_{m_0} = -0.04$.

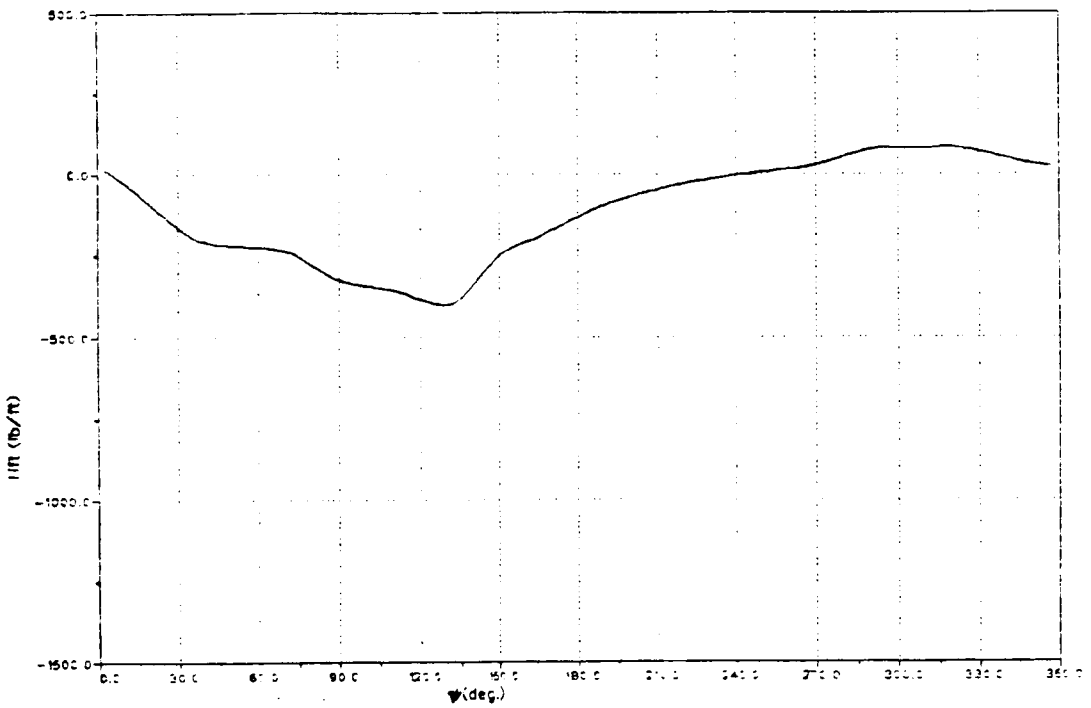

Figure 4-2b Harmonic Contents.

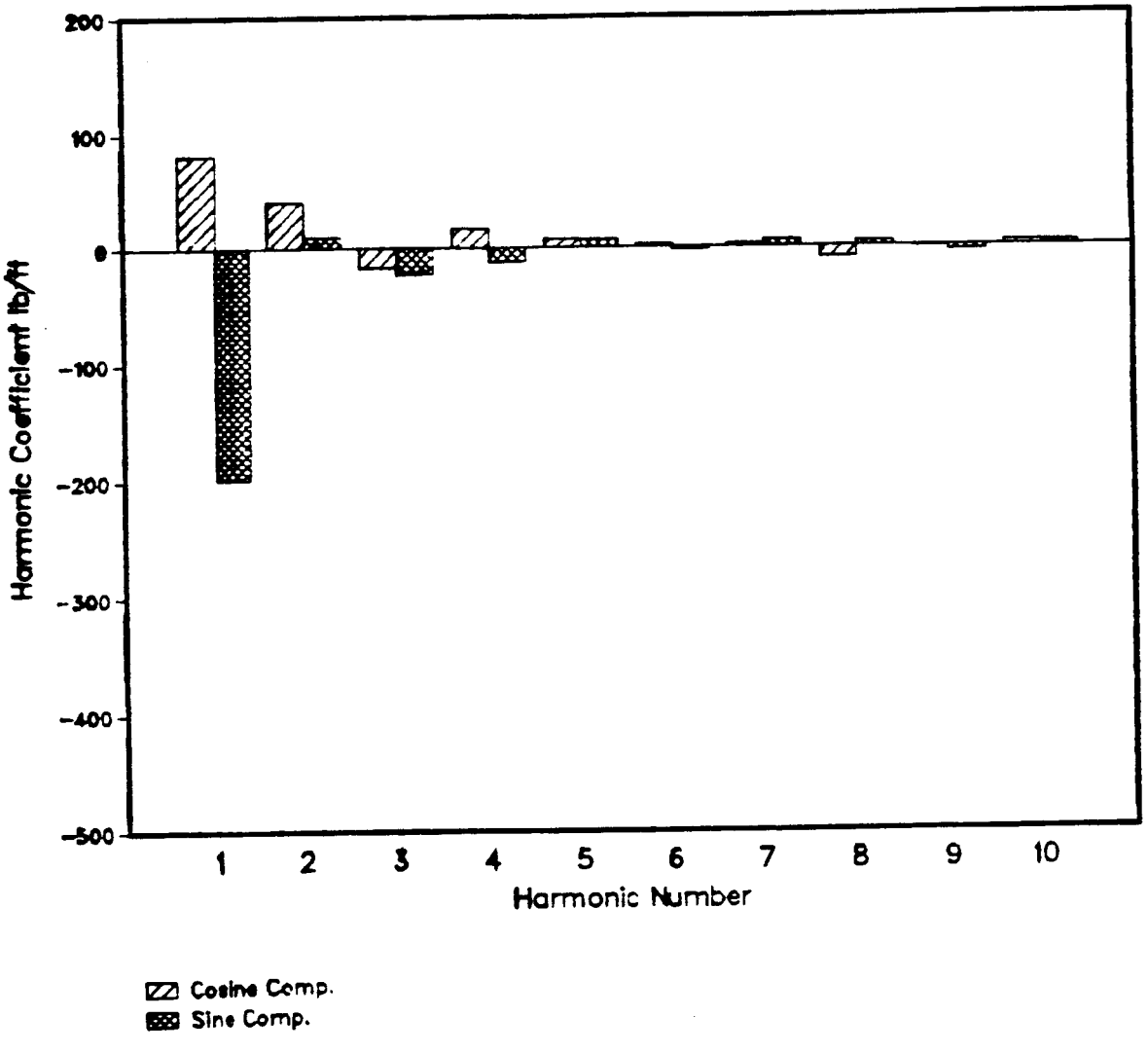

Figure 4-3a Lift Distribution, Rectangular Tip, $\Delta c_{m_0} = -0.08$.

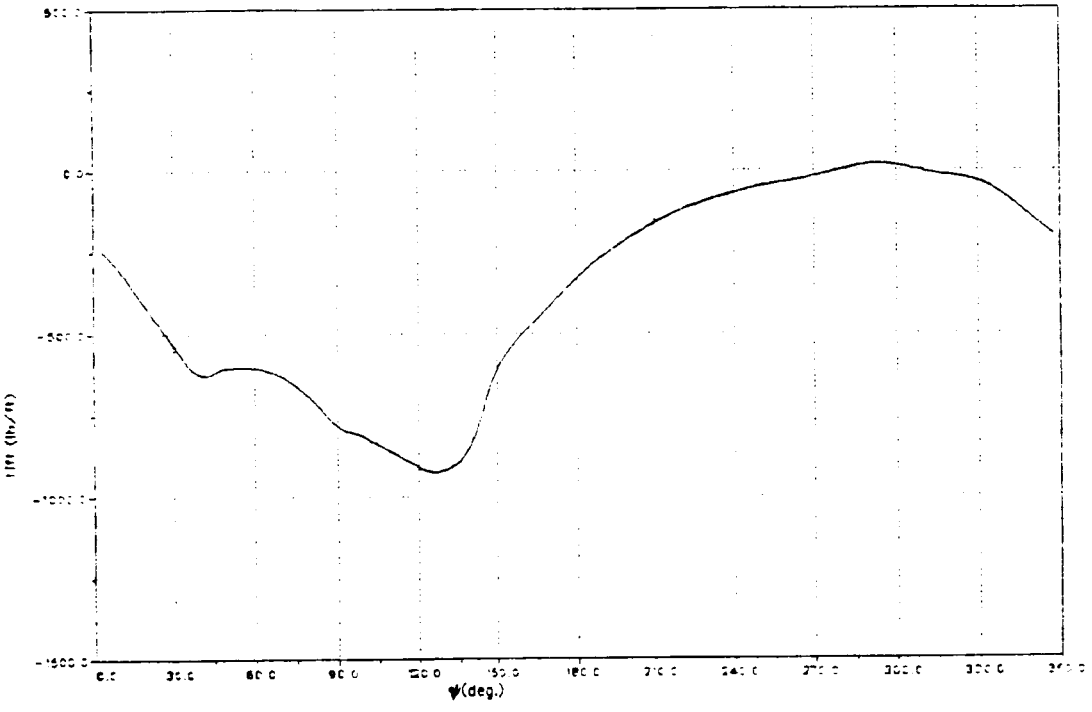

Figure 4-3b Harmonic Contents.

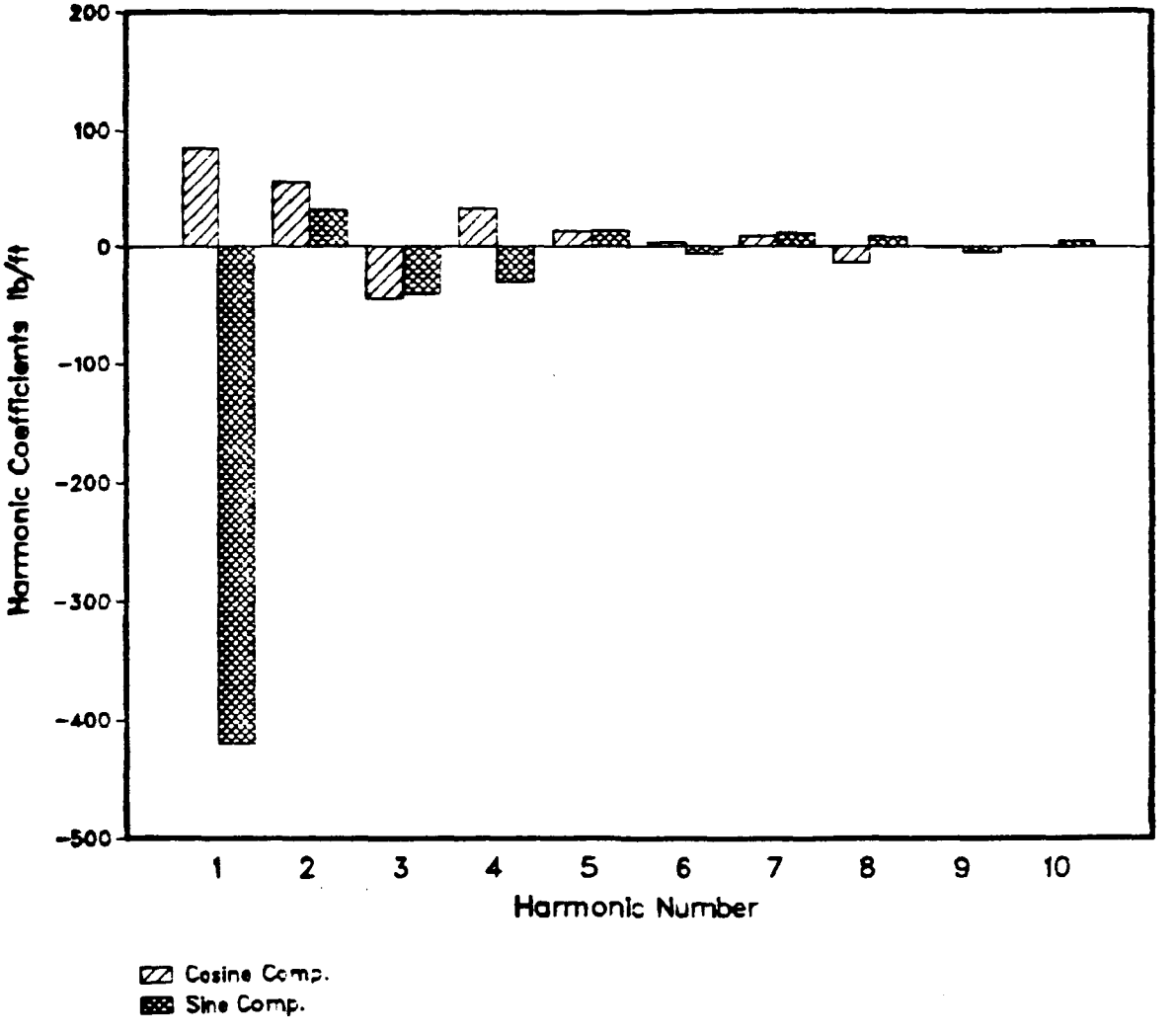

Figure 4-4a Lift Distribution, Swept, Tapered Tip, $\Delta c_{m_0} = 0.00$.

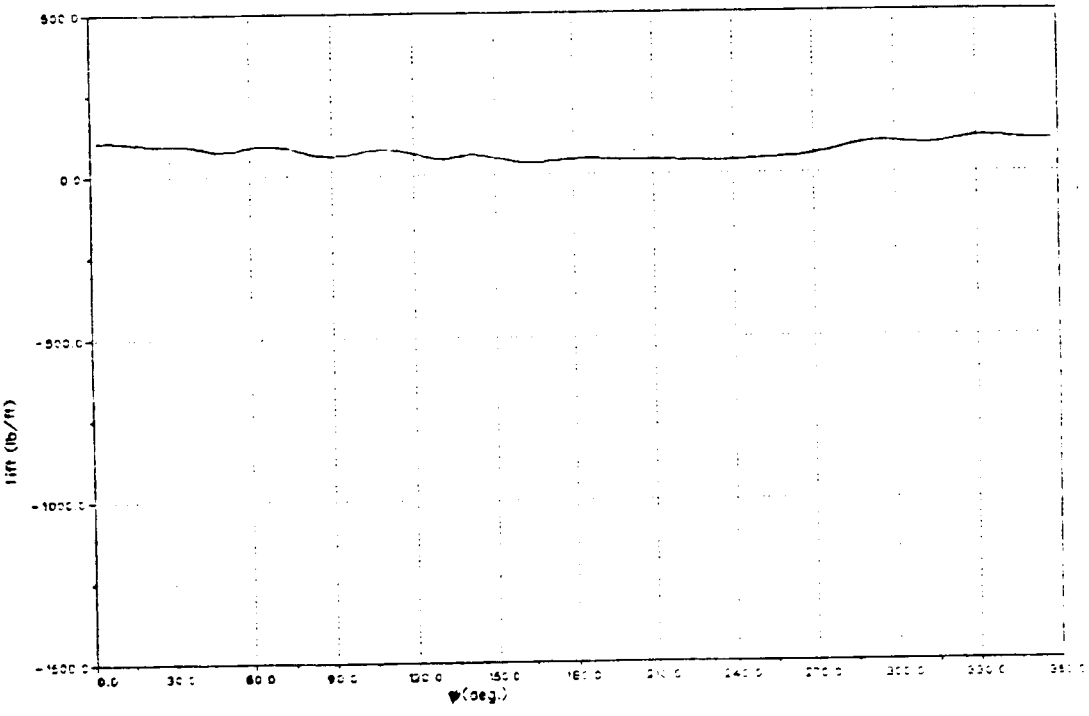

Figure 4-4b Harmonic Contents.

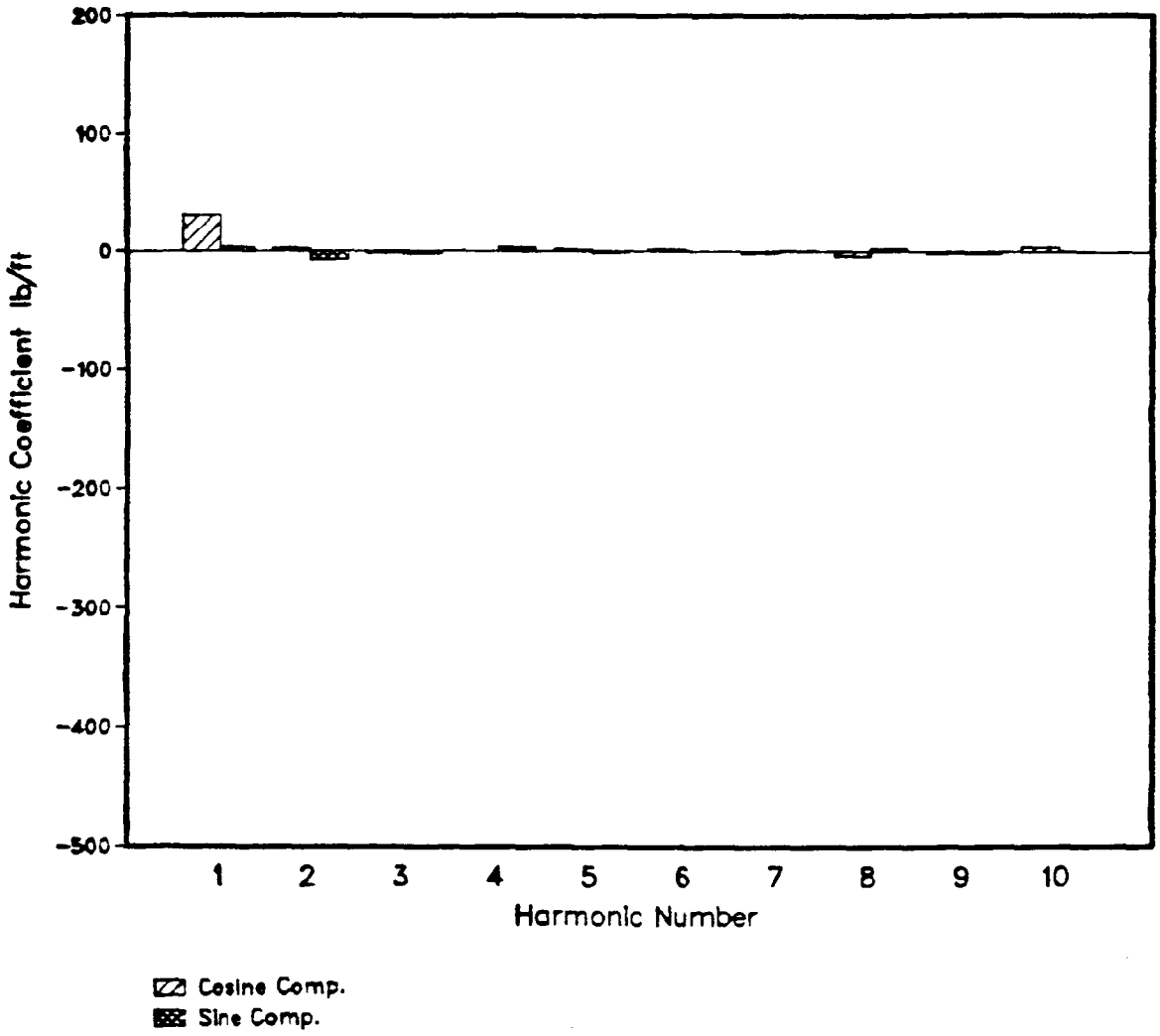

Figure 4-5a Lift Distribution, Swept, Tapered Tip, $\Delta c_{m_0} = -0.04$.

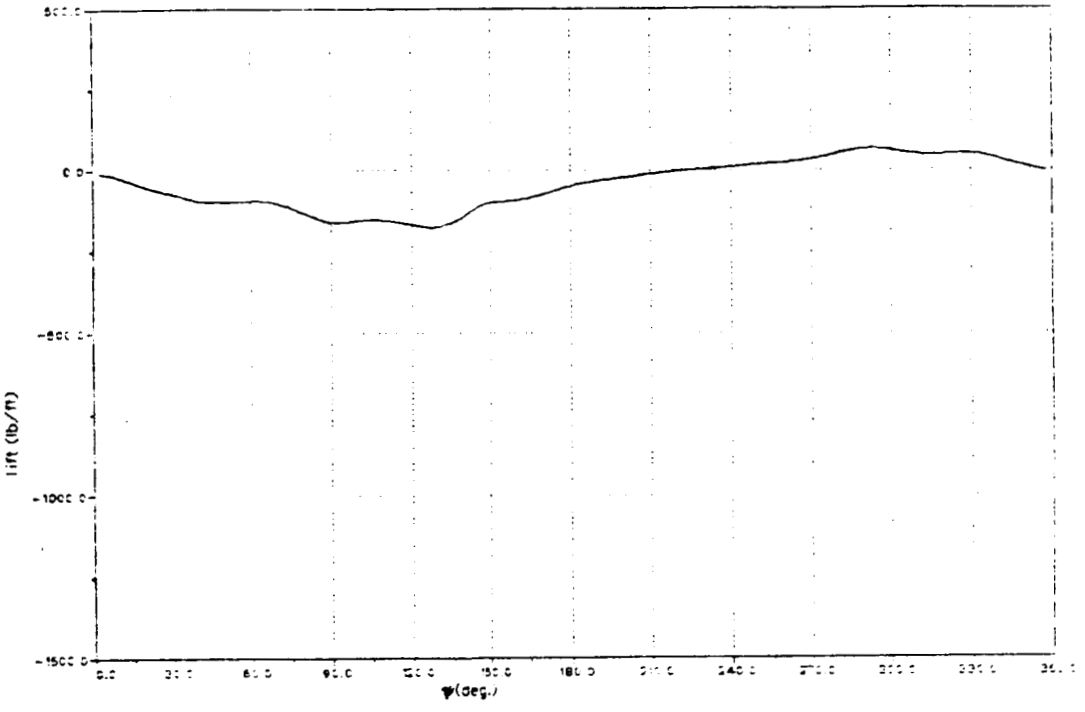

Figure 4-5b Harmonic Contents.

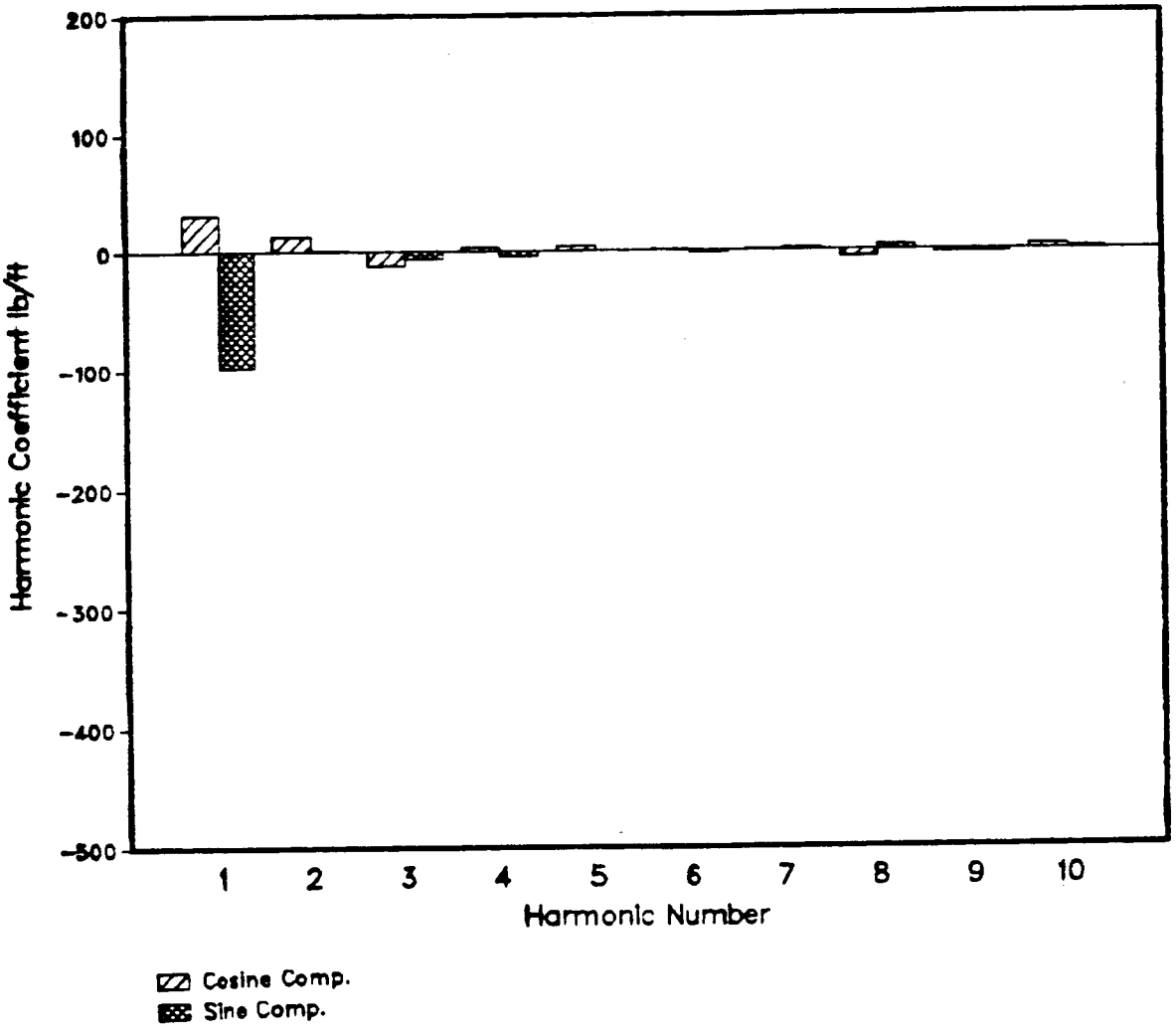

Figure 4-6a Lift Distribution, Swept, Tapered Tip, $\Delta c_{m_0} = -0.08$.

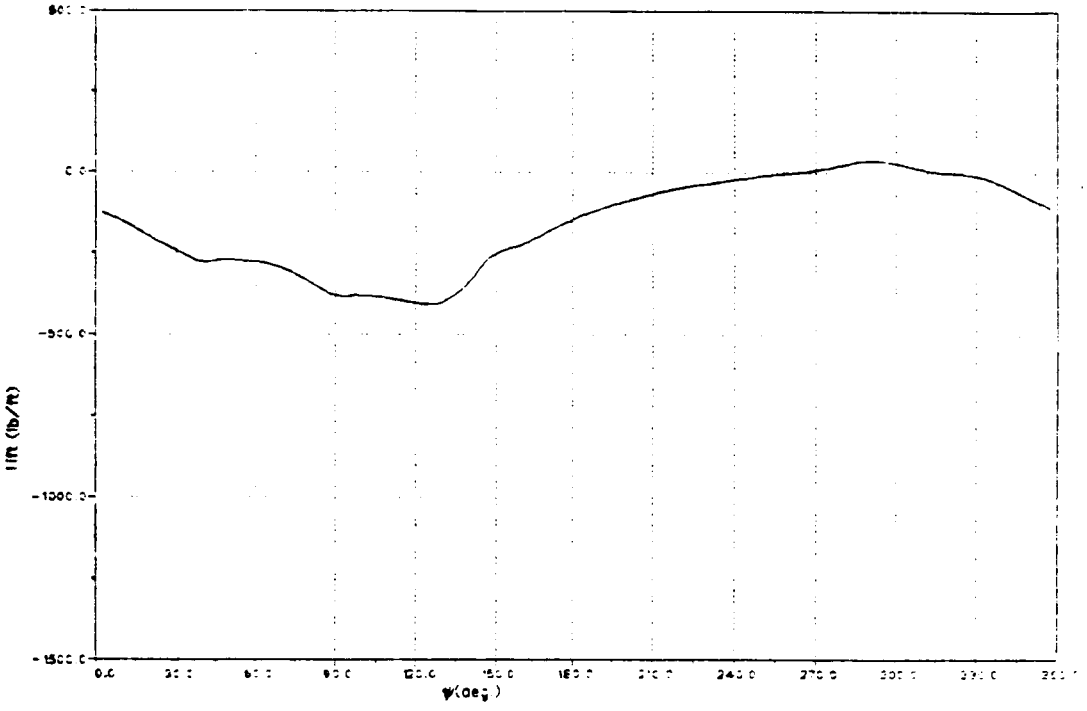

Figure 4-6b Harmonic Contents.

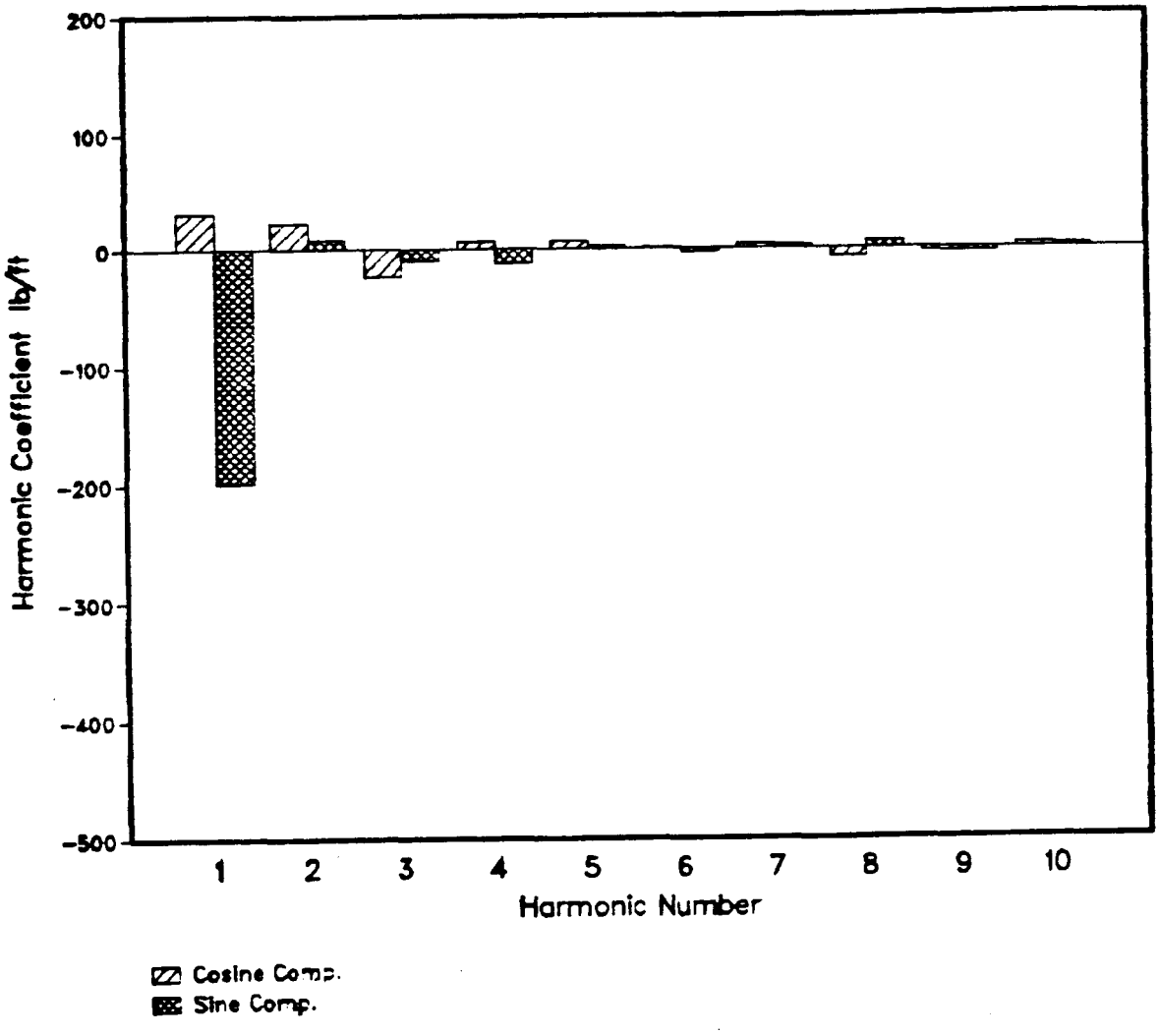

Figure 4-7 Longitudinal Cyclic Control Moment due to Δc_{m_0}.

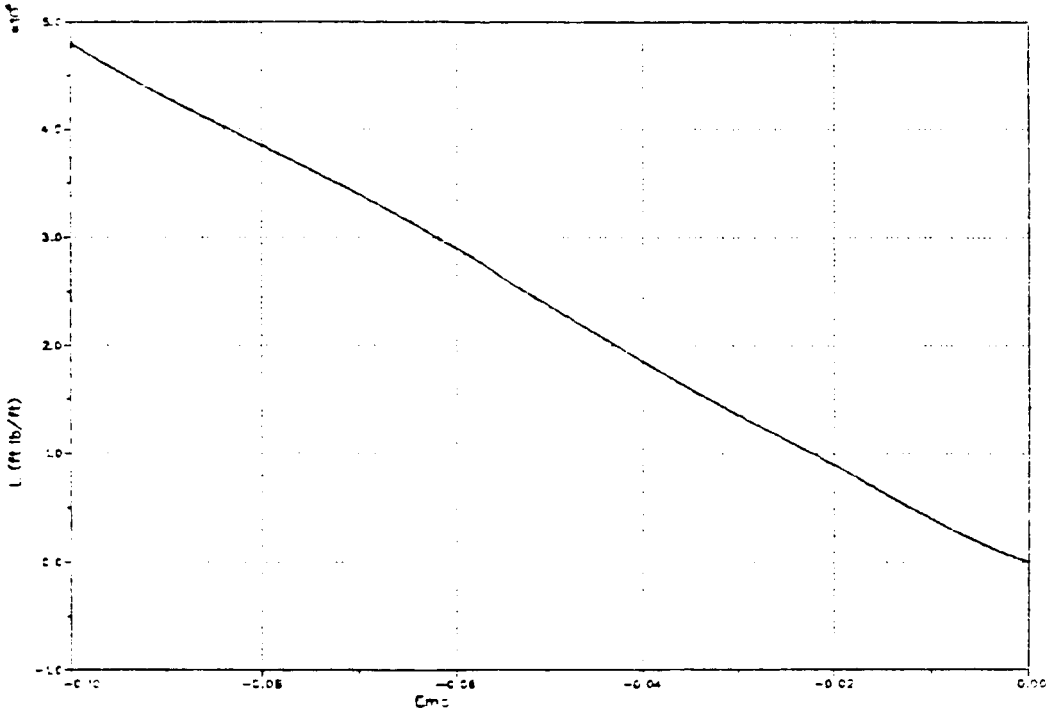

Figure 4-8 Longitudinal Cyclic Control Moment due to Dihedral.

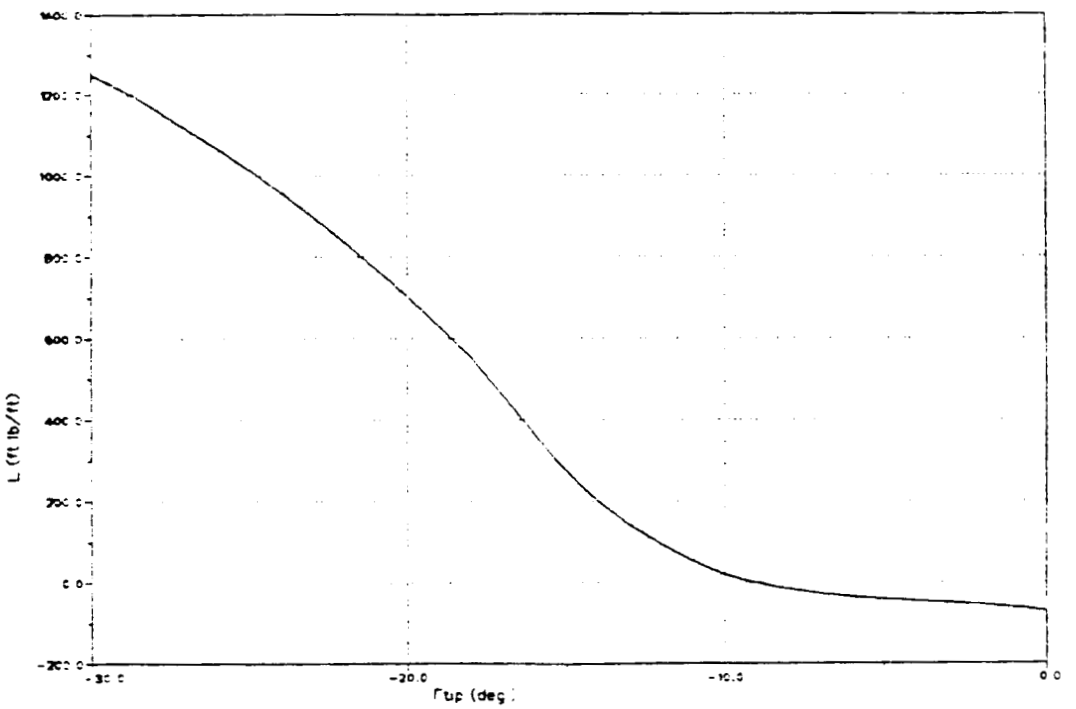

due to drag is also minimized. High drag configuration is obviously not desirable. Second, while the drag is being minimized, the only alternative to obtain the desired pitching moment is to increase the moment arm by increasing the dihedral angle. However, with a large dihedral angle, the aerodynamic force on the tip contributes more to the in-plane forces, namely, H- and Y-forces rather than to the lift (Reference 4). Figure 4-9 shows the longitudinal cyclic control moment with three different levels of airfoil pitching moment and control moment imposed in a rectangular tip. The results on a swept tapered tip are presented in Figure 4-10. As it is clear from these two figures, the rectangular tip produces a larger longitudinal cyclic pitch because of its smaller aerodynamic spring rate. The swept tapered tip seems to respond better to the higher harmonic components of the disturbances. However, judging from the harmonic analysis of the resulting lift distribution, it alone is not enough to justify the use of a swept tip which sacrifices the total longitudinal cyclic control moment. But a swept tip is still favorable from a stand point that it reduces the compressibility effect, since the maximum tip Mach number of the current configuration is in a vicinity of 0.9 (Reference 5).

Figure 4-11 shows the longitudinal cyclic control moment as a function of the mechanical friction level. As the friction level goes higher, it tends to inhibit the tip motion which results in a low longitudinal cyclic control moment. Also, the higher friction level slows down the tip response, especially on the retreating side past $\psi = 270^o$ where the aerodynamic spring rate and aerodynamic pitching moment are small. Therefore, the tip tends to carry the high lift longer than a low friction configuration. This will contribute to the nose-down pitching moment (lateral cyclic control moment). This trend (a decrease in longitudinal cyclic control moment and an increase in lateral cyclic moment) can be best shown by the ratio of the harmonic coefficients, $\left|\frac{b_1}{a_1}\right|$, and it is given in Figure 4-12.

Effects of mechanical spring is shown to be very similar to that in the FTR I performance, namely, a spring with an excessive spring constant will deteriorate the tip movement, which results in small lon-

Figure 4-9 Longitudinal Cyclic Control Moment, Rectangular Tip.

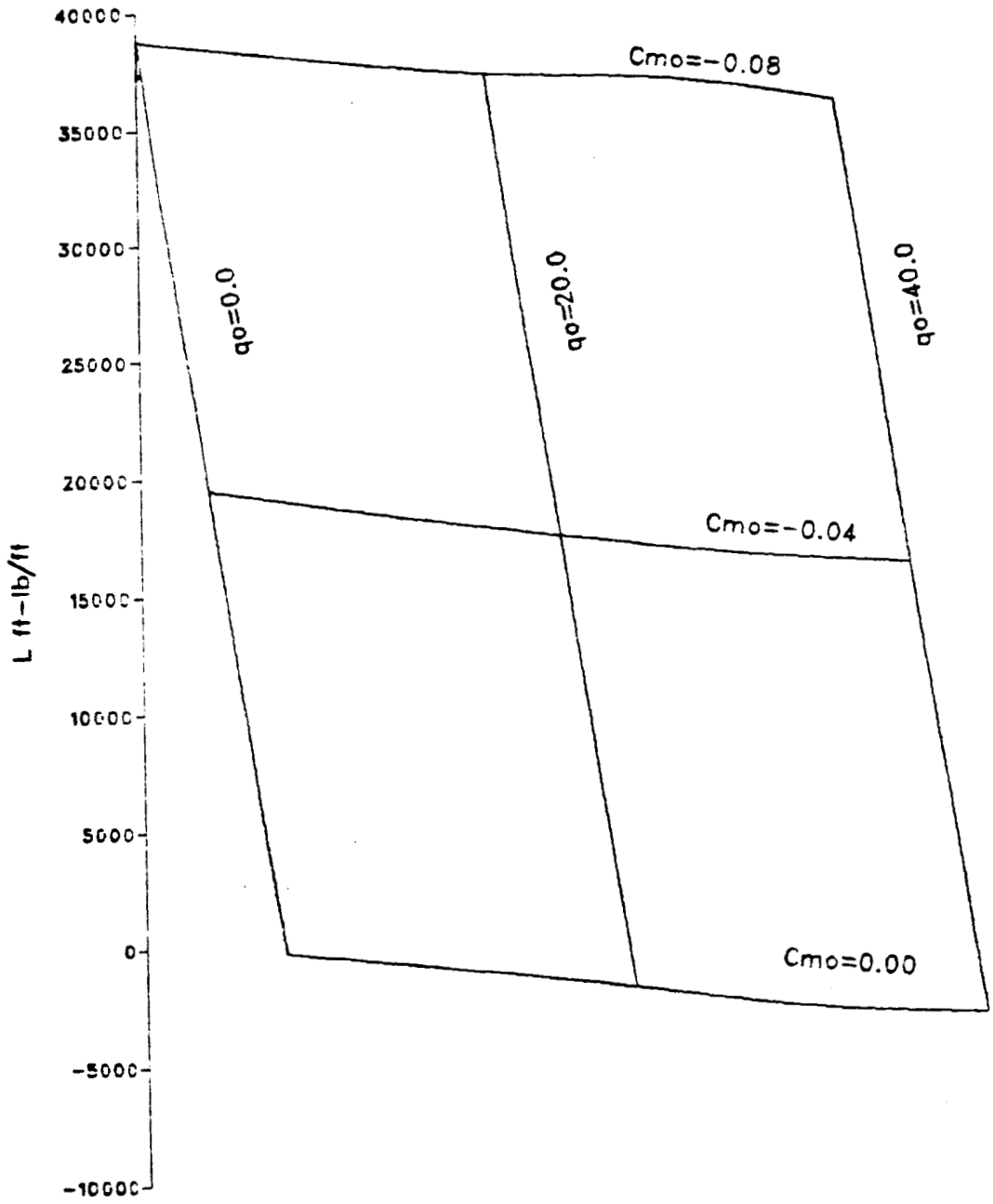

Figure 4-10 Longitudinal Cyclic Control Moment, Swept, Tapered Tip.

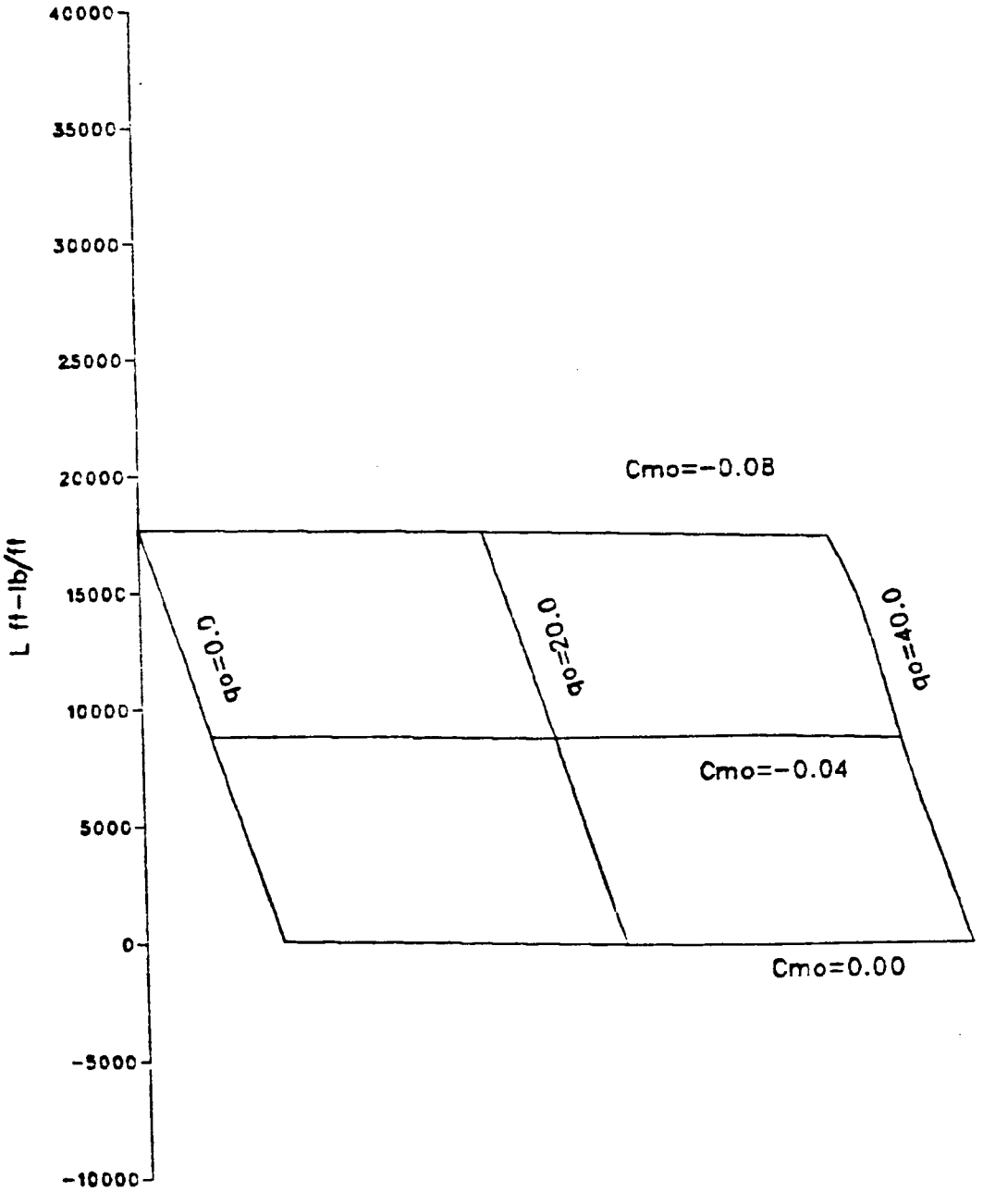

Figure 4-11 Effect of Friction

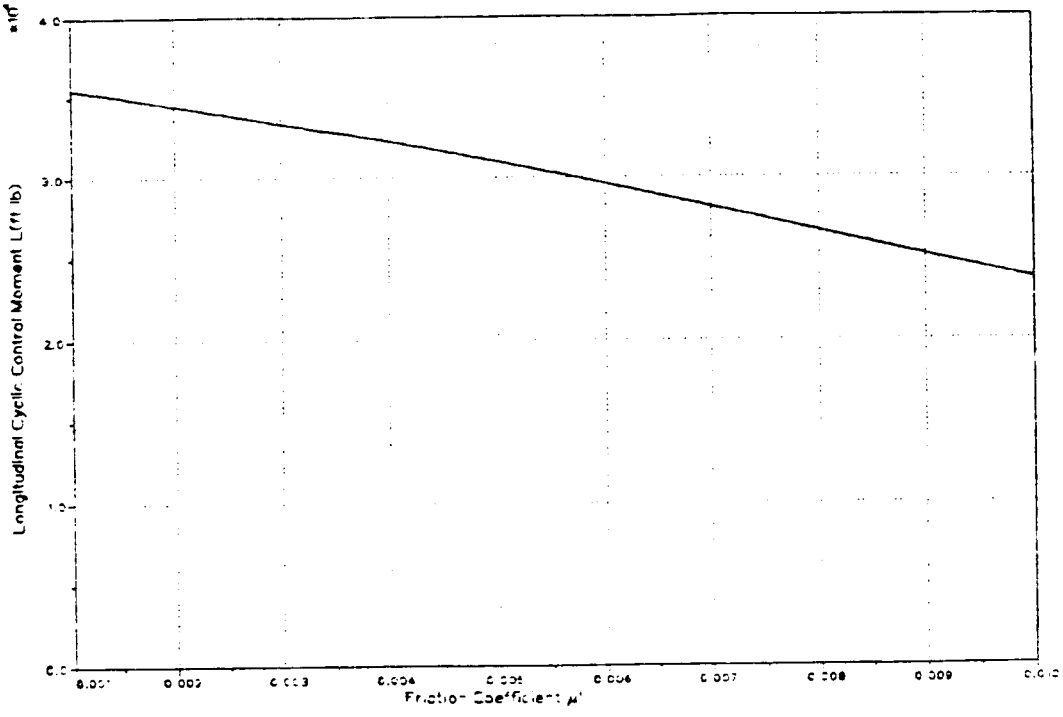

Figure 4-12 Effect on Lateral Cyclic Control Moment.

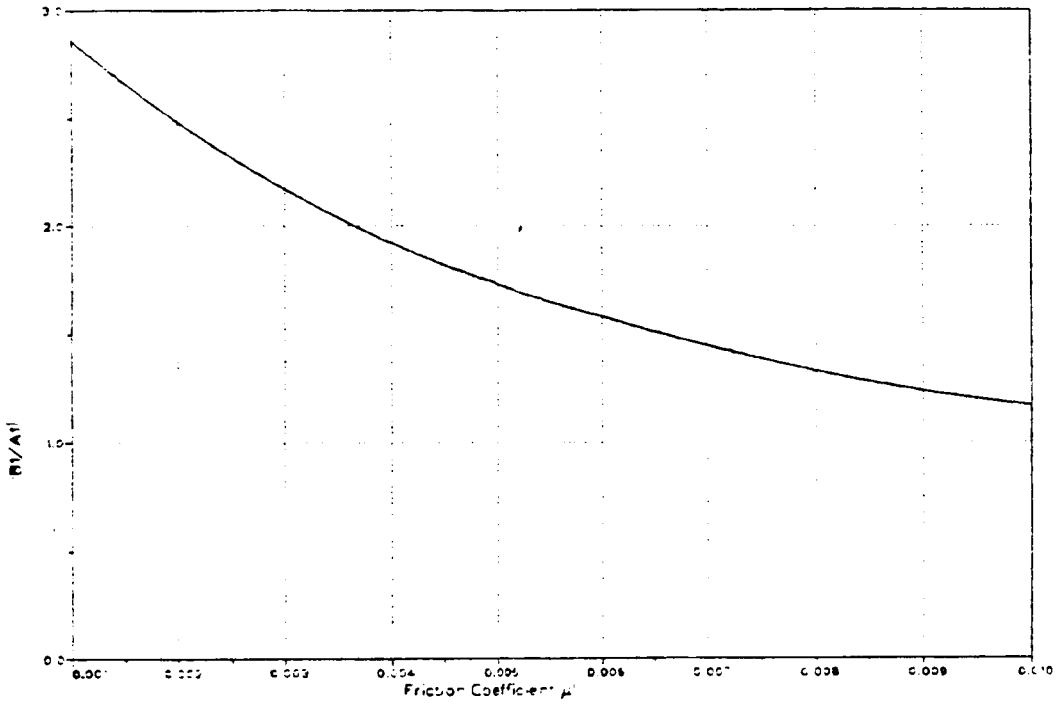

gitudinal cyclic control moment. However, the system can tolerate a small spring constant . This behavior is presented in Figure 4-13.

Since the performance deterioration due to a mechanical spring is very small as long as the spring rate is low, ($k_\theta < 50 ft\ lb$), it is feasible to replace the constant control moment by a pre-twisted spring with a low spring rate. Figure 4-14 shows the longitudinal cyclic control moment generated by the tip with various combination of spring rate and pre-twist angle. The pre-twist was adjusted so that the spring yields a pitch-up moment of $40 ft\ lb$ at the tip pitch angle, $\theta = 0^o$. The asterisk in the figure at $k_\theta = 0$ indicates the longitudinal cyclic control moment with a constant moment controller.

4.4. Conclusions.

FTR II demonstrated a potential to generate a longitudinal cyclic control moment without the aid of an active control device. Once- per-revolution oscillation of the free-tip, which results in the longitudinal cyclic control moment, can be generated easily by the use of an airfoil with a large negative pitching moment due to its camber or a tab deflection.

The dihedral angle of the tip was proven to be inefficient to produce such tip oscillation.

A rectangular tip showed a favorable result over a swept, tapered tip because of its small aerodynamic spring rate which enables the tip to have a larger amplitude of once-per-revolution oscillation, resulting in a larger longitudinal cyclic control moment. However, a swept tip can be employed to reduce the compressibility effect if the aerodynamic spring rate was kept small by shifting the tip pitch axis rearward, closer to 25 % chord line (Reference 5). This configuration is recommended for a further analysis.

Mechanical spring and friction should be minimized. A simplified con-

Figure 4-13 Effect of Mechanical Spring.

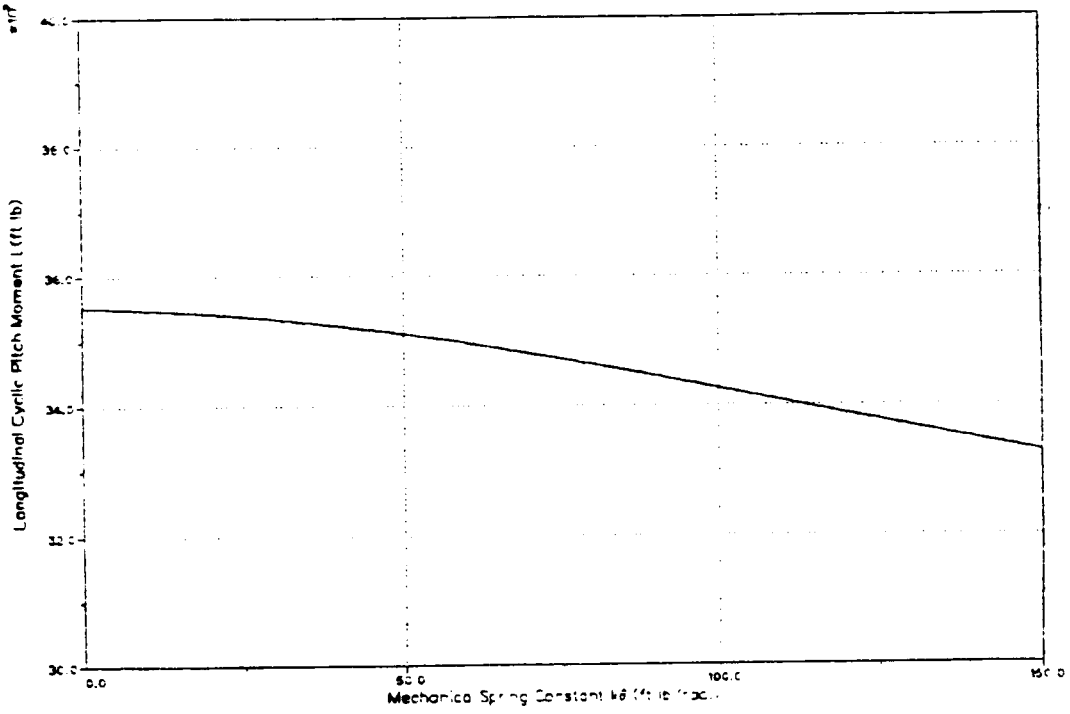

Figure 4-14 Simplified Controller.

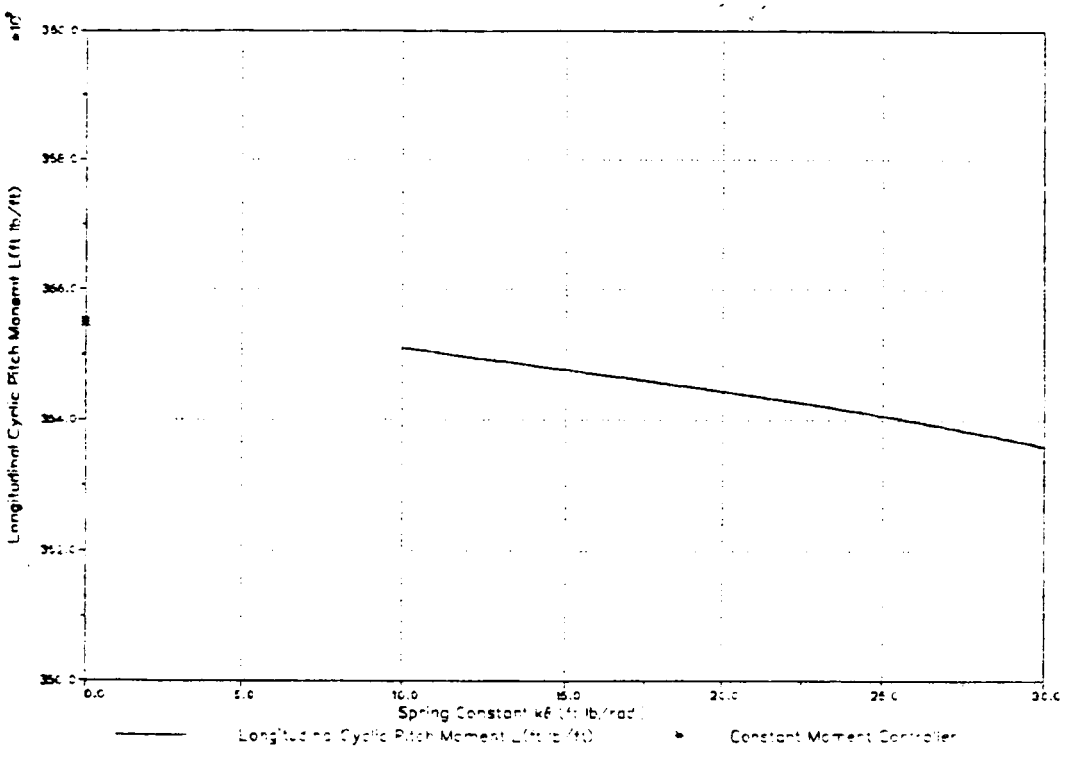

troller consists of a torsional spring with small spring rate and a large pre-twist can replace the constant moment controller, since the system can tolerate a small spring rate.

5. Performance Analysis of FTR II

5.1. Numerical Model Description.

A rotor performance prediction program used in this analysis is Boeing Vertol B-65 program, which is a modified version of B-67. It is a three dimensional rotor performance analysis program for a single or a twin rotor system. But it does not account for a fuselage, tail or tail rotor.

These programs are proprietary programs developed by Boeing Vertol Company, and detailed information can be obtained from Boeing Vertol only on request (Reference 6). What follows in this section is a brief description of the program. The limitations of the program are also discussed.

5.1.1. Structural Coupling

The program allows blades to be flexible. The structural properties of the blade are prescribed in terms of mode shapes. One can specify the only first and second elastic flapwise bending and first elastic torsion. Therefore, the blade is rigid in lagwise bending and chordwise bending.

5.1.2. Aerodynamics

A basic aerodynamic theory used in the program is the blade element theory (Reference 7 and 8), which requires the empirical data for each airfoil section. The data of the airfoil aerodynamic characteristics, namely, c_ℓ, c_d and c_m as functions of angle of attack and Mach number, are supplied in a separate data file called "airfoil look-up table", or simply, "airfoil

table". The program allows one to use up to five different airfoils along the blade. Note that the data contained in the airfoil table represents steady and two dimensional aerodynamic characteristics. The program also utilizes Theodorsen's function to account for the unsteady effects (Reference 9). The same theory is used to make a correction in pitching moment.

There is an empirical correction factor for the tip section which takes care of the three dimensional effect of the tip region.

Although the actual aerodynamic parameters are being computed by the blade element theory, the program also includes the wake effect, as an inflow angle distribution.

Initially, the downwash component at the blade is assumed to be uniform. Then the program computes aerodynamic parameters at each computation station, and iterates for a given trim condition. This process is called uniform downwash iteration. The discussion on the trim iteration will be given later.

The computation is continued to include non-uniform downwash effect. Once the lift distribution on the blade is computed, one can obtain the circulation strength on a given segment. Placing the vortex of the same strength on the semi-prescribed wake geometry (straight segments laid over the helical path), Biot-Savart law can be applied to compute the downwash component at a given computation point to yield a new inflow angle. This process is iterated until the circulation strength of each bound element converges.

Here, it should be noted that this procedure is similar to the lifting line theory. However, resulting vortex array does not necessarily satisfy the tangency condition on the airfoil surface, because it is being calculated from the empirical airfoil data.

Once a converged solution is obtained for the vortex strength, trim parameters are calculated. If the resulting trim does not match the prescribed trim condition, blade pitch control input is adjusted, and the entire process is iterated. This process is called the nonuniform downwash

iteration.

5.1.3. Trim Condition

The user can specify the desired thrust and side force, then the program performs an iterative process to match the thrust and side force for a fixed shaft angle and a convergent flapping level (β-iteration). The user can also prescribe the collective pitch and lateral cyclic pitch instead. In this case, the program computes thrust and side force resulting from the given control input without the trim iteration except for the β-iteration.

In the current version of B-65, the propulsive force trim is not operational. Therefore a user must trim the rotor manually by changing the longitudinal cyclic pitch control on a trial and error basis.

5.1.4. Free-Tip Pitching Motion

Pitch angle of the free-tip is described by a second order nonlinear ordinary differential equation used in the AZIMUTH program, given in equation (3.1). For simplicity, the term representing the feathering moment, which has a very small effect, was omitted.

The controller was formulated as a helical screw (Reference 10). However, this configuration was proven to be an inefficient design (Reference 3) due to high friction level. Here a small value was prescribed for the surface friction coefficient to model a controller with improved performance which is now being designed at NASA Ames and Boeing Vertol, which dose not gave a highly loaded surface contact. The helix angle α_{HELIX} was determined by a fixed amount of tip mass and desired control moment level. Its formula

is

$$q_0 = \frac{m_{tip}\Omega^2 R_{tip}}{3}\left(\frac{d_i^3 - d_o^3}{d_i^2 - d_o^2}\right)\left[\frac{\tan\alpha_{HELIX} - \mu' \operatorname{sign}\left(\frac{d\theta}{dt}\right)}{1 + \mu' \tan\alpha_{HELIX} \operatorname{sign}\left(\frac{d\theta}{dt}\right)}\right] \qquad (5.1)$$

where

m_{tip} =mass of the Free-Tip
Ω =rotor angular velocity
R_{tip} =radial station of the Free-Tip c.g.
d_i, d_o =inner and outer diameters of the helical screw
α_{HELIX} =helical screw angle
μ' =coefficient of surface friction
$\frac{d\theta}{dt}$ =pitch rate of the Free-Tip

This configuration is shown schematically in Reference 10.

5.1.5. Boeing Vertol C-60 Program

To check the validity of B-65 program, C-60 program was used, together with the wind tunnel test data. C-60 program utilizes the same aerodynamic theory as B-65. However, it does not include three dimensional tip relief effect. Its wake model is even cruder than that of B-65. It has trailing vortices only from the root and tip of the blade. It utilizes the finite element method to compute the elastic deformation of the blade. Since there is only one element in chordwise direction, the blade is rigid in chordwise bending.

A detailed discussion is given in Reference 11.

5.2. Geometric and Aerodynamic Parameters.

The basic model used in this analysis is the CH-47C model rotor used in the 1981 wind tunnel test at Boeing Vertol. Its various parameters are given below.

$$\begin{aligned}
\text{Radius} &= 8.4\ (ft) \\
\text{Number of Blades} &= 4 \\
\text{Chord} &= 6.73\ (in,\ \text{constant}) \\
\text{Solidity} &= 0.085 \\
\text{Twist} &= -9.45^{o}\ (\text{linear}) \\
\text{Airfoil} &: \text{V23010-1.58 (constant, tip and inboard)} \\
\text{Blade Cutout} &= 0.1825\ (r/R) \\
\text{Flapping Hinge} &= 0.031\ (r/R) \\
\text{Blade Weight Moment} &= 34.5\ (ft\,lb,\ \text{around flapping hinge}) \\
\text{Blade Moment of Inertia} &= 4.55\ (slug\,ft^2,\ \text{around flapping hinge})
\end{aligned}$$

The first elastic mode shape for flapwise bending and chordwise torsion as well as the corresponding natural frequencies are supplied for B-65. The mode shape for flapwise bending and torsion are presented in Figures 5-1 and 5-2 respectively.

For C-60 program, mass, moment of inertia about the pitch axis, flapwise bending rigidity and torsional rigidity of each segment were prescribed.

All experimental data used in this analysis for the comparison were taken in the Boeing Vertol's wind tunnel with the Dynamic Rotor Test Stand (DRTS) which incorporates an electrical power supply and six-component balance.

Figure 5-1 First Elastic Mode Shape of Flapwise Bending

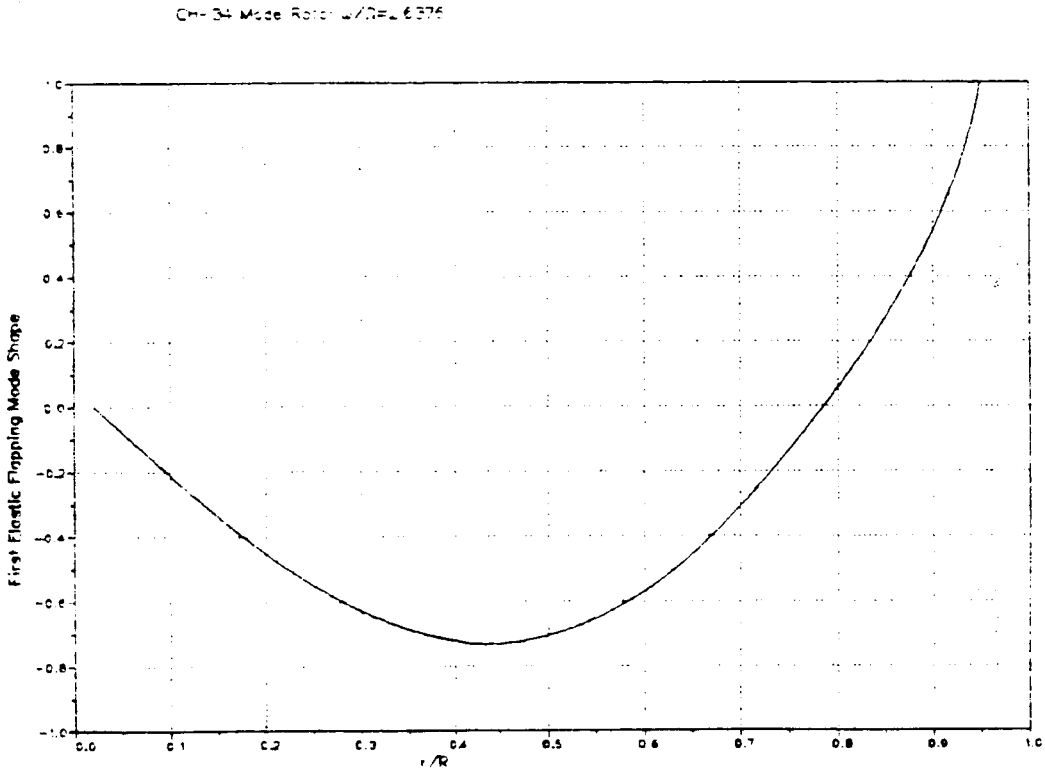

Figure 5-2 First Elastic Mode Shape of Torsion

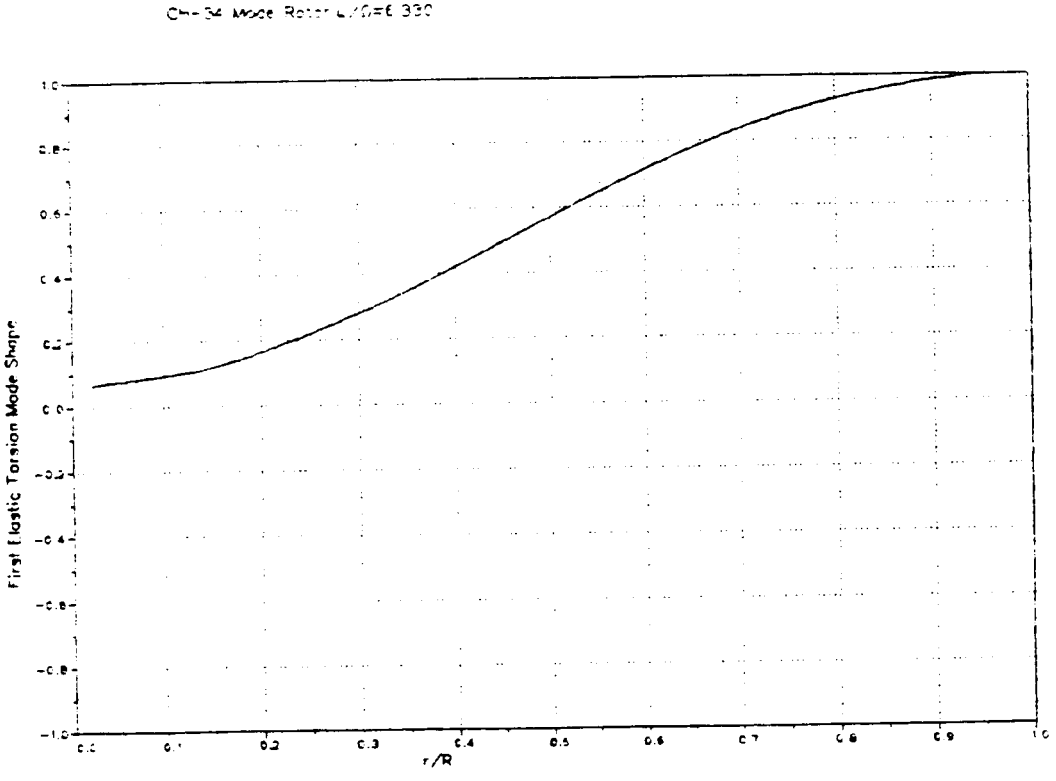

5.3. Airfoil Selection.

An airfoil section of a rotor blade must operate efficiently in a very wide spectrum of operating condition. The critical operating condition can be classified in three regions as illustrated in Reference 12. These three regions are; Region I with high Mach number and small lift coefficient for advancing blade, Region II with low Mach number and maximum lift coefficient for retreating blade and Region III with moderate Mach number and moderate lift coefficient for hovering.

Each region has different aerodynamic requirements. For example, the most important requirement in Region I is the good drag-rise characteristics, while in Region II, it is the high maximum lift coefficient for hover with high gross weight, and in Region III, it is the gentle stall characteristics.

Since the blade tip is the only consideration in this discussion, one can concentrate in the airfoil performance in Region I. General requirements for a conventional rotor tip airfoil in this region are

1. The airfoil should have a high drag divergence Mach number.

2. Low drag in all operating range.

3. Relatively constant pitching moment coefficient.

4. Small pitching moment.

There are two special requirements for FTR II tip section airfoil. They are

1. Significant negative pitching moment coefficient.

2. Capability to carry a significant negative lift.

It should be emphasized here that the significant negative pitching moment of the airfoil is the key element of the FTR II performance, as shown in section 4. The significant airfoil pitching moment (negative or positive) is unacceptable for a conventional tip because it creates a periodic elastic blade twist during the forward flight which eventually generates undesirable vibrations.

To meet the above stated requirements, a uniform loading type airfoil, such as a supercritical airfoil or its derivative is an ideal candidate for FTR II tip section. However, as of October 1983, all high speed series (HS-series) NASA supercritical airfoils were still classified. The only available data (airfoil coordinates and aerodynamic data) are for the low speed series (LS-series), medium speed series (MS-series) and some airfoils from the early works (Reference 13 though 21).

With the limited alternatives, MS(1)-0313 airfoil was selected for this feasibility study because of its relatively high design Mach number (0.72) and drag divergence Mach number (0.76) (Reference 15 & 16).

Even for this airfoil, the available aerodynamic data are limited to a small range of operating conditions (such as $M \leq 0.4$ for $-8^o \leq \alpha \leq 8^o$,or $-2^o \leq \alpha \leq 2^o$ for $M \approx 0.8$). Such a small range of conditions is not enough to construct an airfoil table for B-65 program.

In the Boeing's airfoil table, it requires the airfoil data for $M = 0.0$ to $M = 1.0$ including the stall condition.

For the present purpose, a numerical method was employed to obtain the necessary data set to construct a new airfoil table. The computer program used was NYU program version H (Reference 22 through 25). The program is a two dimensional subsonic/transonic airfoil analysis program and it is available on CRAY 1/S at NASA Ames Research Center.

Unfortunately, this program cannot produce results for large angles of attack which cause a significant pressure peak near the lead-

ing edge and/or a flow separation over a large area due to stall. However, B-65 program showed that the tip section does not experience a large angle of attack. Therefore, the range of angles of attack covered by NYU program is wide enough for the present application.

Figures 5-3 through 5-5 present a comparison of the numerical results and experimental data at low Mach number. It shows good accuracy of the program. These figures also show typical aerodynamic characteristics of the MS(1)-0313 airfoil. Its airfoil coordinates are presented in Figure 5-6.

The airfoil table for MS(1)-0313, which was set up by this program, is presented in Appendix B.

The airfoil used for the wind tunnel model, designed by Boeing Vertol, is V23010-1.58, which is basically NACA 23010 with its leading edge modified so that it has a significant leading edge camber. It also has a trailing edge tab so that its pitching moment can be adjusted to a desired level by a tab deflection. Therefore, it is possible to generate a significant negative pitching moment coefficient by the tab, However a deflection of trailing edge tab corresponds to an airfoil with a trailing edge camber which tends to create a very high drag.

Although V23010-1.58 has some disadvantages stated above, this airfoil was also used in the analysis for comparison purpose since it was the airfoil of the wind tunnel model, which serves as a base line model. Its typical aerodynamic characteristics and coordinates are presented in Reference 26.

5.4. B-65 Program Verification.

Before the program was applied to the Free-Tip configuration, the numerical results of B-65 were compared with the Boeing Vertol's wind tunnel test data for a conventional rotor, which also serves as a base line

Figure 5-3 Typical Lift Characteristics of MS(1)-0313

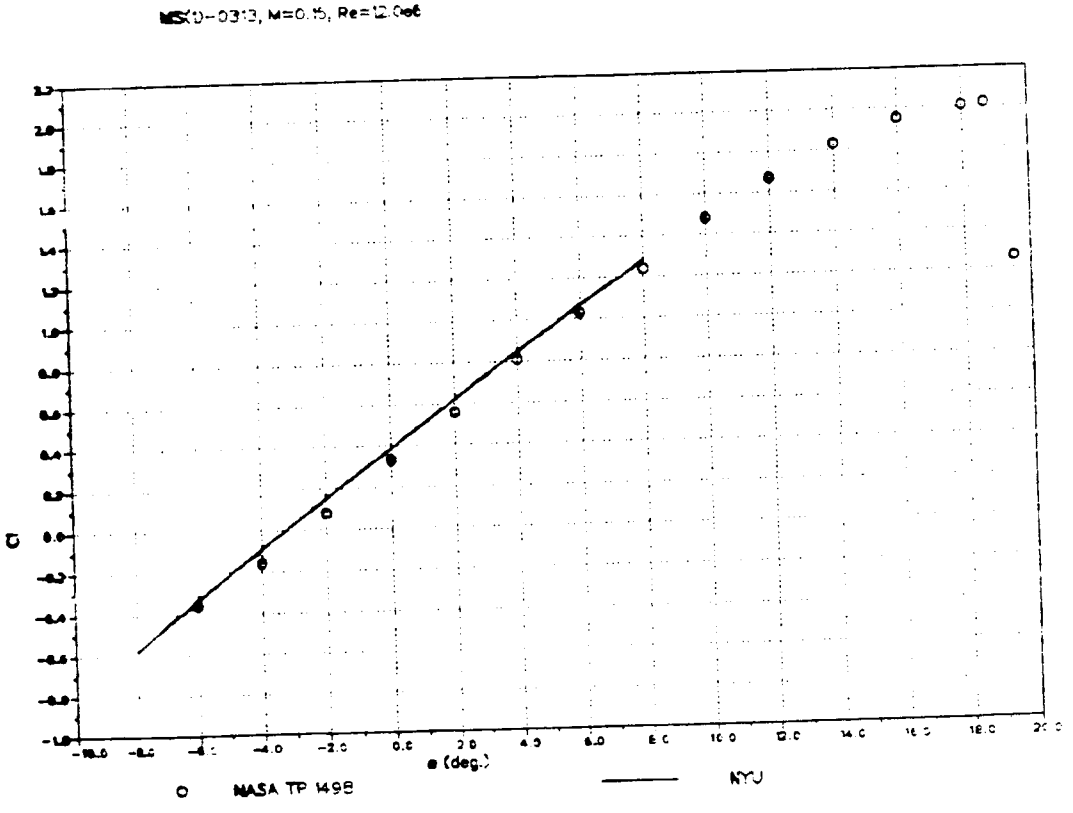

Figure 5-4 Typical Drag Characteristics of MS(1)-0313

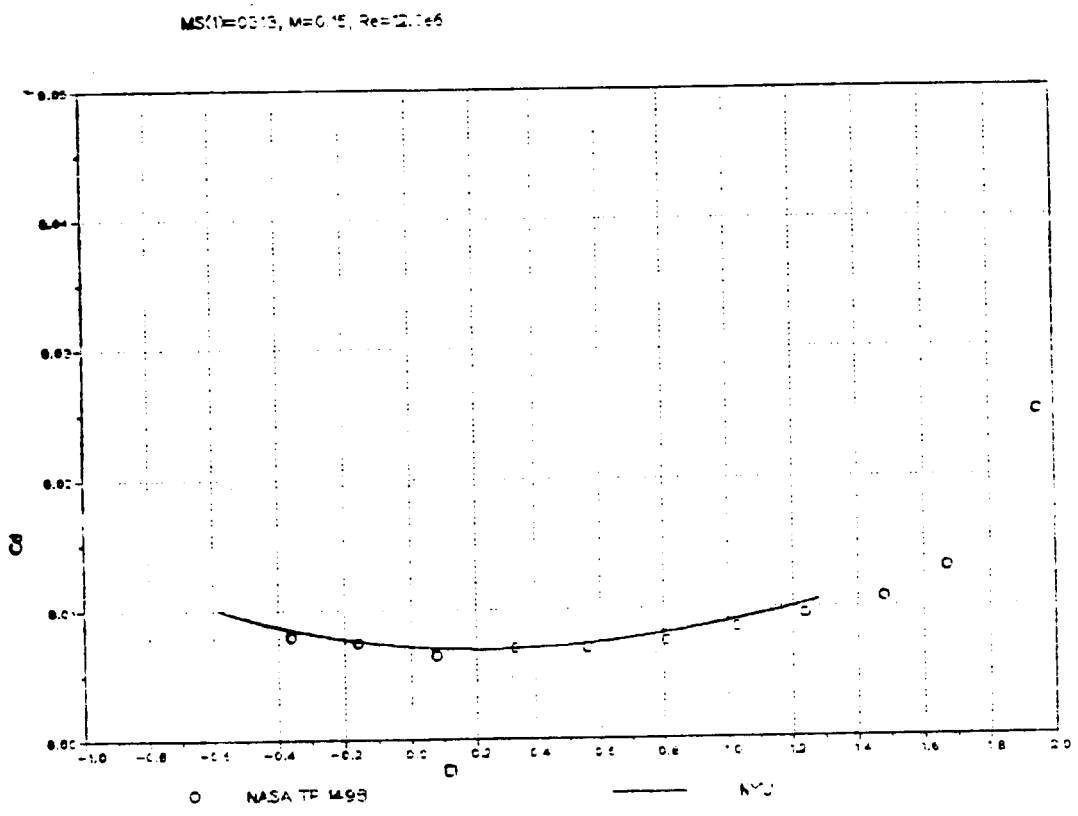

Figure 5-5 Typical Moment Characteristics of MS(1)-0313

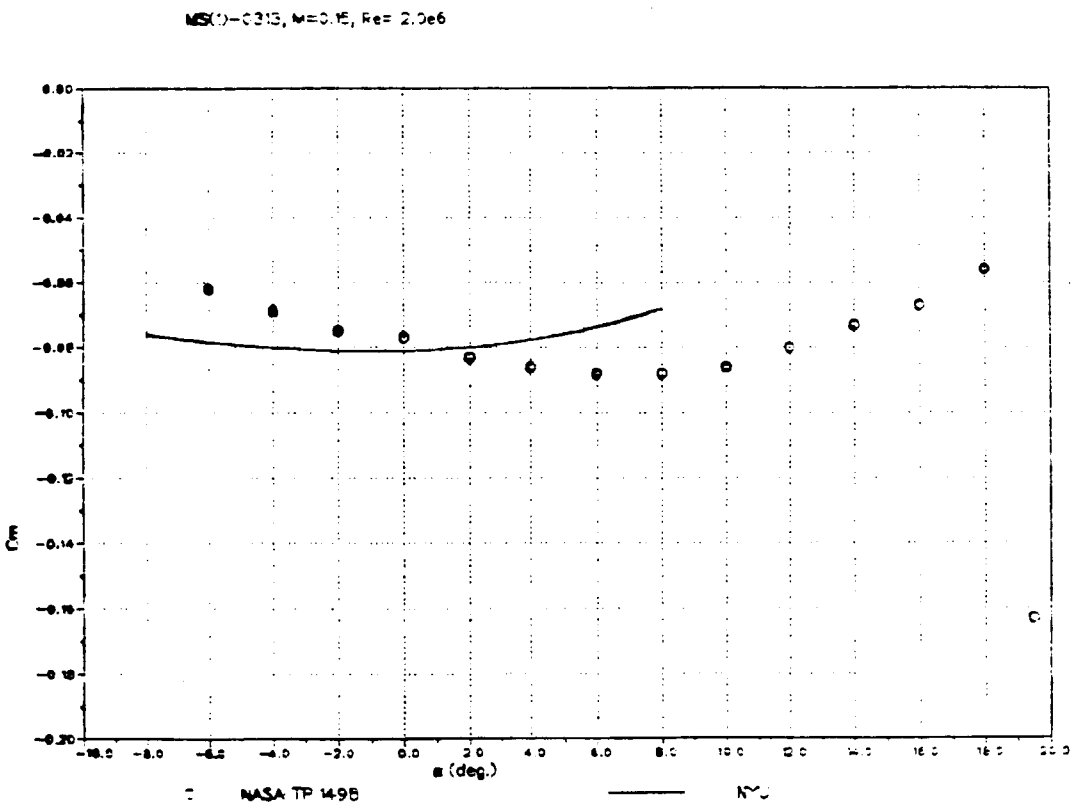

Figure 5-6 Airfoil Coordinates of MS(1)-0313

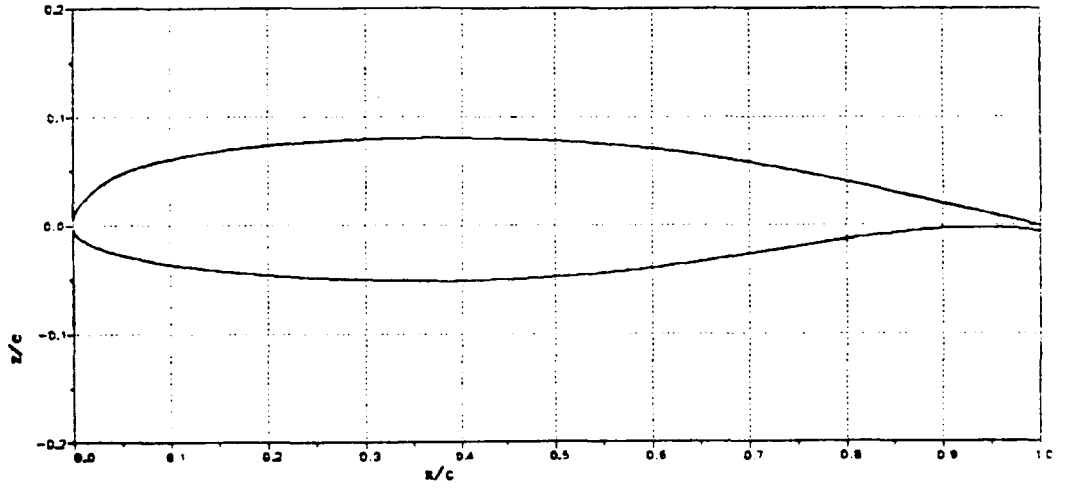

configuration for the FTR performance assessment. C-60 program was also used to confirm the results.

The wind tunnel test was performed with the following flight condition.

$$
\begin{aligned}
V &= 124.76 \quad (kts) \\
\Omega &= 766 \quad (r.p.m.) \\
\mu &= 0.3 \\
\rho &= 0.00270 \quad (slug/ft^3) \\
a &= 1131.32 \quad (ft/sec.)
\end{aligned}
$$

The trim parameters are

$$
\begin{aligned}
\alpha_{shaft} &= -2^o \\
T &= 859 \text{ to } 2500 \quad (lb) \\
Y &= -47.88 \text{ to } -12.99 \quad (lb) \\
X &= -26.60 \text{ to } 23.44 \quad (lb).
\end{aligned}
$$

The Free-Tip was locked in place during the test so that it resembles a conventional rotor.

It should be noted that the control input (collective and cyclic pitch), obtained from the numerical method which gives the identical trim condition (trim for dimensional forces, namely, T-, X- and Y-forces shown above) given in the experiment, cannot be compared with the actual control input of the wind tunnel model, since the inflow model in the numerical model is purely hypothetical. Therefore, the comparison of the numerical results and experimental data must be done by other parameters which ralate to total rotor performance. The power coefficient, C_P/σ and the equivalent lift-drag ratio L/D for a given thrust coefficient, C_T/σ were selected as the performance criteria.

Figures 5-7 and 5-8 show the results of B-65 and C-60 as well as experimental data for various thrust levels. There is a considerably large discrepancy between the numerical results and the wind tunnel

Figure 5-7 Conventional Rotor Power Requirement, $\mu \approx 0.3$, $\alpha_{shaft} \approx -2^{o}$

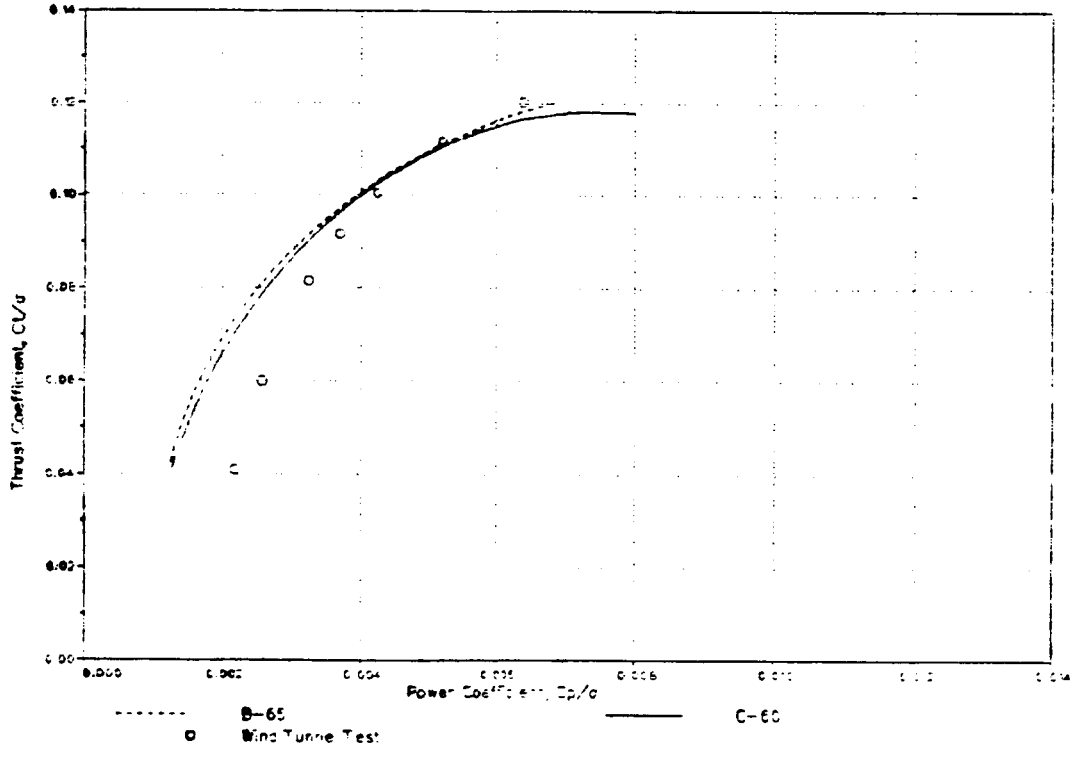

Figure 5-8 Conventional Rotor Lift-Drag Ratio $\mu \approx 0.3$, $\alpha_{shaft} \approx -2^o$

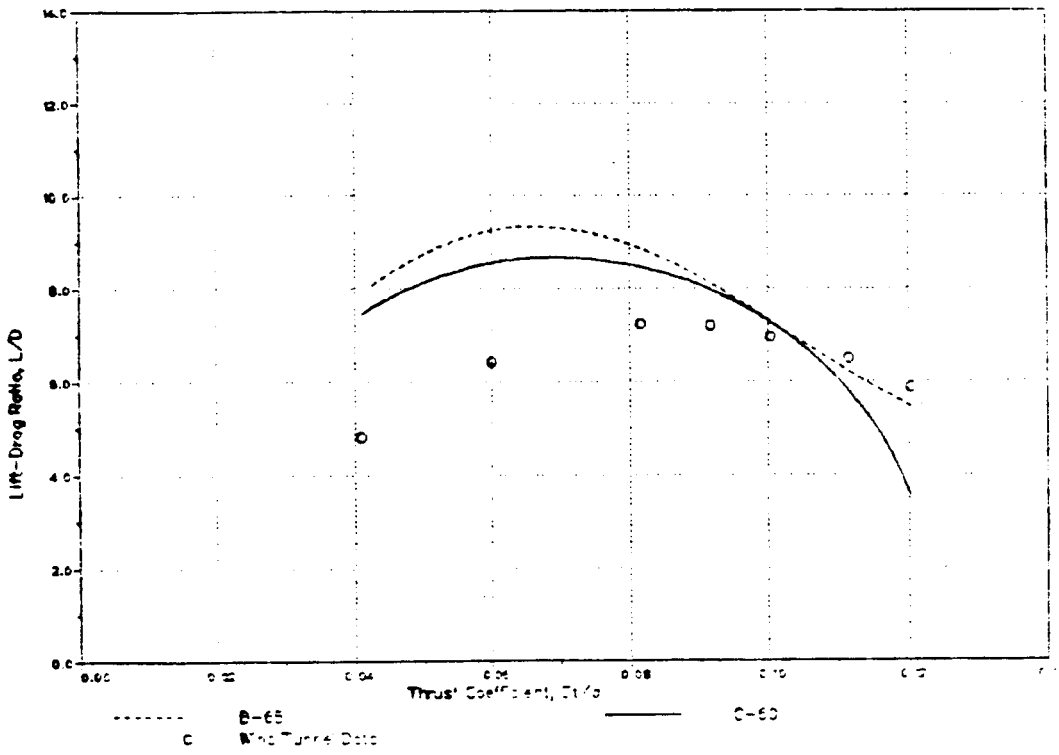

data. and both programs have the same tendency. That is, in low thrust region, they tend to underestimate the power requirement and overestimate the resulting lift-drag ratio. In high thrust region, they tend to overestimate the power requirement and underestimate the lift-drag ratio.

There are three possible reasons which cause this discrepancy. They are

1. Difference in structural property between theories and the actual rotor blade used in the test
   The experimental data was taken with a set of modified blades which accommodates the Free-Tip and its controller. Although the blade is conventional in terms of aerodynamics because the tip is locked in place, it differs from a conventional blade in terms of structure. For example, it has a relatively large mass (controller and Free-Tip shaft) around $\frac{1}{8}$-chord in the inboard section adjacent to the tip. The mode shape used in B-65 was generated for a conventional blade. C-60 cannot account for such chordwise mass distribution because it only allows one chordwise element. Because of these reasons, certain effects associated with the extra mass, such as torsional acceleration of the blade due to flapping, etc., have not been accounted for in the analysis.

2. Simplified wake model
   Since the wake model used in the analysis is primitive, it should have some contributions to the discrepancy. The discrepancy due to the vortex model becomes more severe in high thrust region because of high vortex strength. This effect has been exaggerated for C-60, whose vortex model is even cruder than that of B-65.

3. Reynolds number effect
   The airfoil tables used by both programs contain c_l, c_d and c_m for a full scale blade. Therefore, a correction factor is necessary when they are applied to a small scale model rotor, particularly for drag

coefficient.

Reference 6 indicates that the Reynolds number effect must be included when the airfoil table is used for an analysis of a rotor with small chord, and the program accommodates the drag coefficient compensation factors for this purpose. The drag coefficient is adjusted in the program by the following linear function.

$$c_d(\text{computation}) = a\, c_d(\text{airfoil table}) + b \tag{5.2}$$

For the present configuration, the average Reynolds numbers at the tip are

2.5×10^6 for model rotor
7.0×10^6 for full scale rotor.

Note that the model rotor is a tip Mach number scale model. Therefore, the difference in Reynolds numbers comes from the physical size of the rotor alone.

Although the aerodynamic data for V23010-1.58 for the above mentioned Reynolds numbers were not available, the data for NACA 23012 with Reynolds numbers of 3.0×10^6 and 8.0×10^6 were obtained from Reference 27.

Figure 5-9 presents the drag coefficient with the low Reynolds number ($c_{d_{RL}}$) as a function of the drag coefficient with high Reynolds number ($c_{d_{RH}}$) for a given angle of attack. With these data three linear models were generated by the linear regression.

$$c_{d_{RL}} = a\, c_{d_{RH}} + b \tag{5.3}$$

The first model, obtained by using all data points, yields $a = 1.7437$ and $b = -0.004$. Since the last data point seems to be a dominating factor in this model, the second model was obtained without this data point. It gives $a = 1.5385$ and $b = -0.0025$. The third

Figure 5-9 Drag Compensation Models

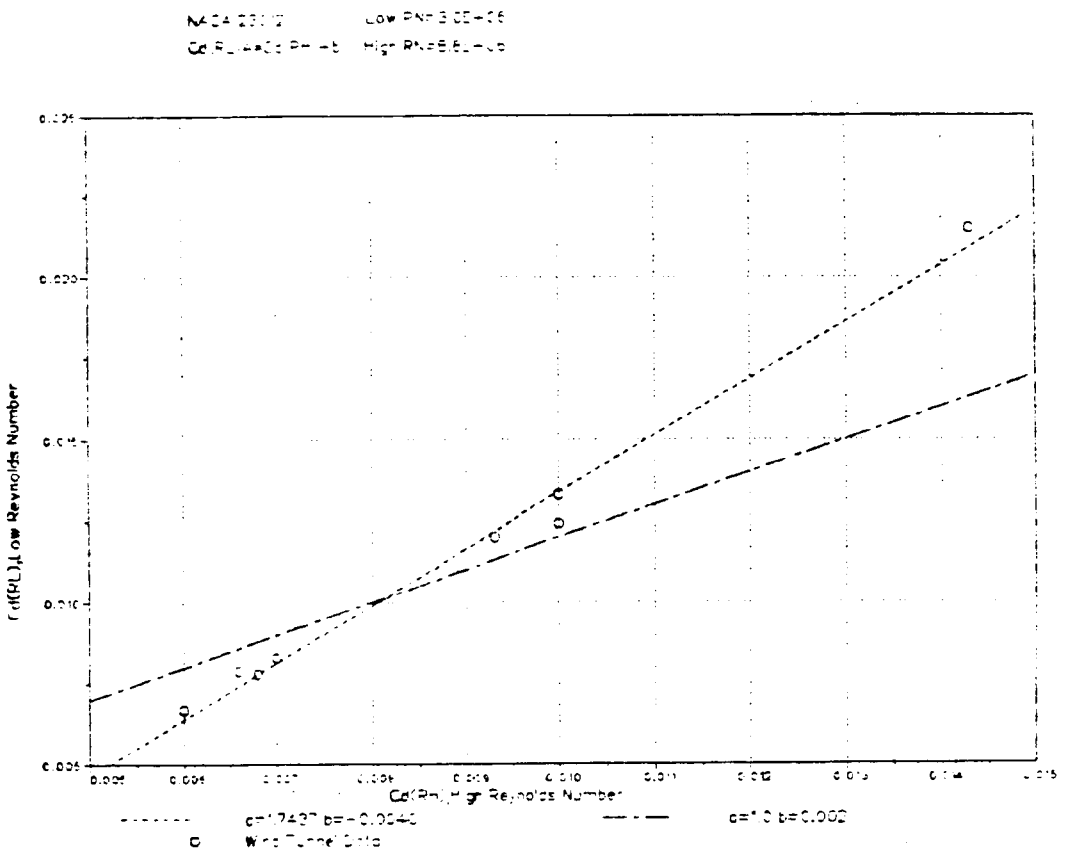

model was designed with $a = 1.0$. It yields $b = 0.002$. This is an average value of two models with and without the last data point.

Figures 5-10 and 5-11 show the results for B-65 which correspond to each drag compensation model. It definitely shows an improvement in correlation. It appears that the last model (with a constant Δc_d shift) yields the most reasonable results.

The same drag compensation model was applied to C-60. The results given in Figures 5-12 and 5-13 show a reasonably good correlation with B-65 results and experimental data, although, C-60 still tends to overestimate the power and underestimate lift-drag ratio in high thrust region.

To make any further improvement, structural properties of the particular blade used in the wind tunnel test data must be used. Also, the wake measurement must be performed experimentally. Only then the numerical model can be improved. However, such data are not available at this moment.

To re-confirm the accuracy of B-65, the data correlation analysis was again performed with a different trim condition. The rotor shaft was tilt more forward to result in a larger propulsive force.

$$\alpha_{shaft} = -7^{o}$$
$$T = 855 \text{ to } 2220 \quad (lb)$$
$$Y = -41.24 \text{ to } -5.12 \quad (lb)$$
$$X = 47.62 \text{ to } 198.39 \quad (lb)$$

The constant drag shift, $\Delta c_d = 0.002$ was maintained. The results of B-65 are shown in Figures 5-14 and 5-15 together with the wind tunnel test data and C-60 results.

Judging from these result obtained for two different flight conditions, it can be concluded that B-65 can predict the power requirement and lift-drag ratio reasonably well for a given trim condition. Because the error in the

Figure 5-10 Power Requirement for Various Drag Models

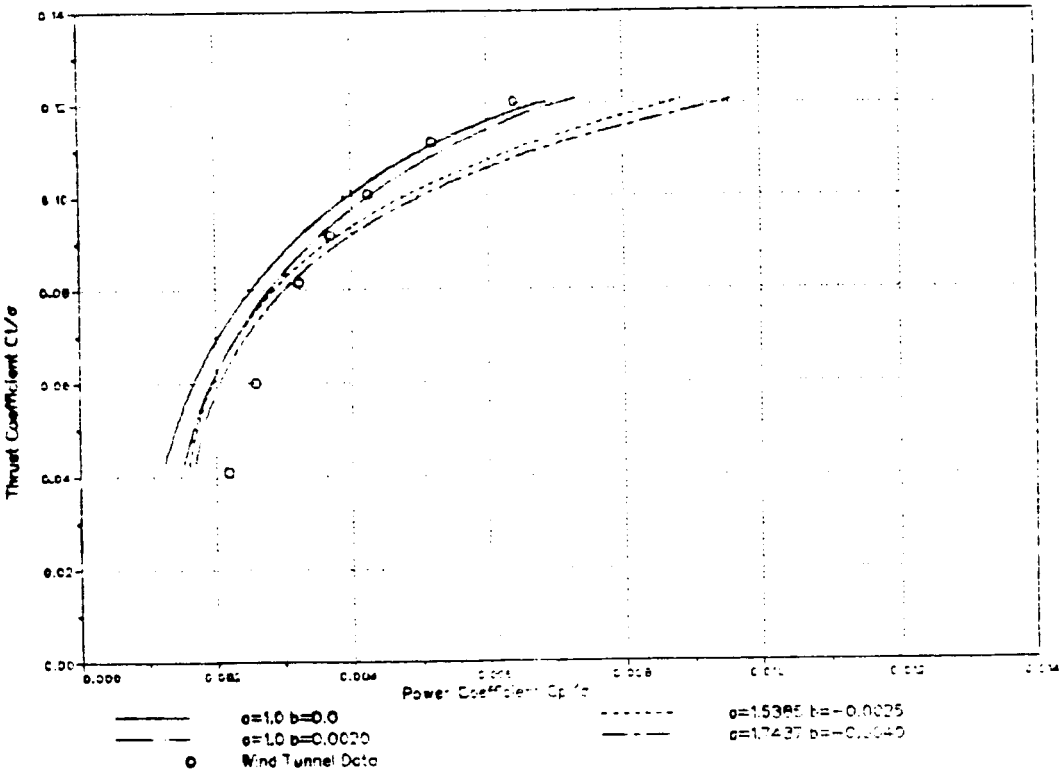

Figure 5-11 Lift-Drag Ratio for Various Drag Models

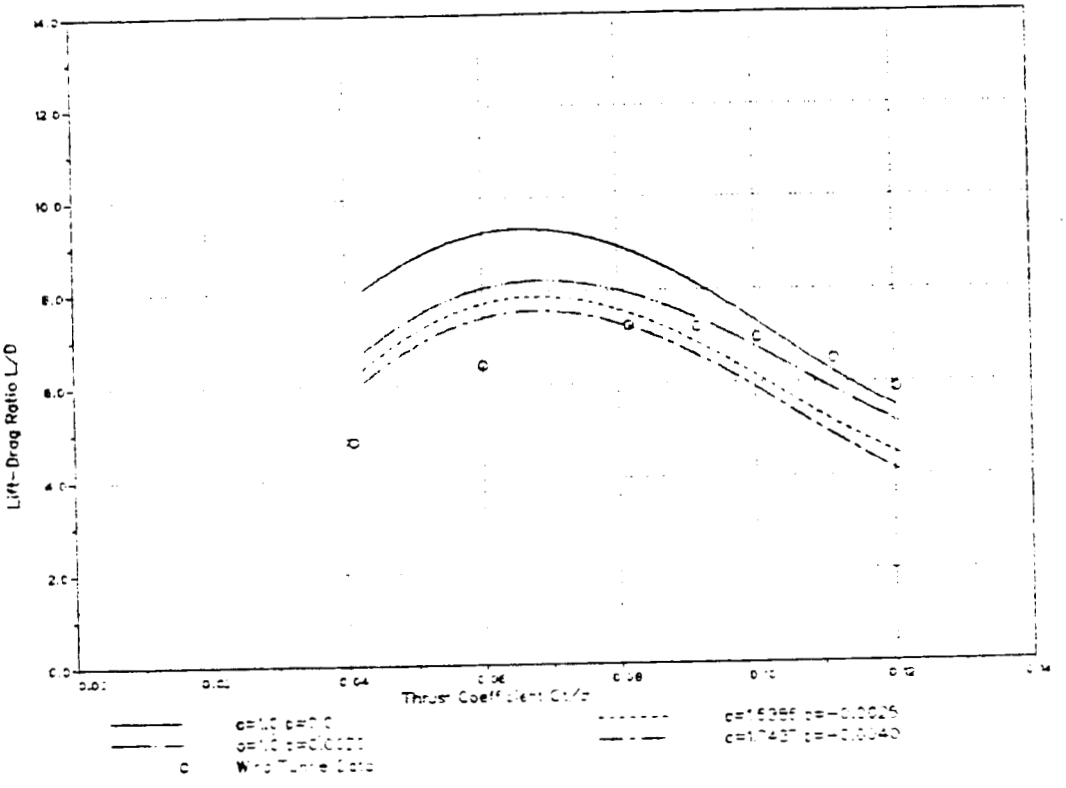

Figure 5-12 Comparision of B-65 and C-60, Power Requirement

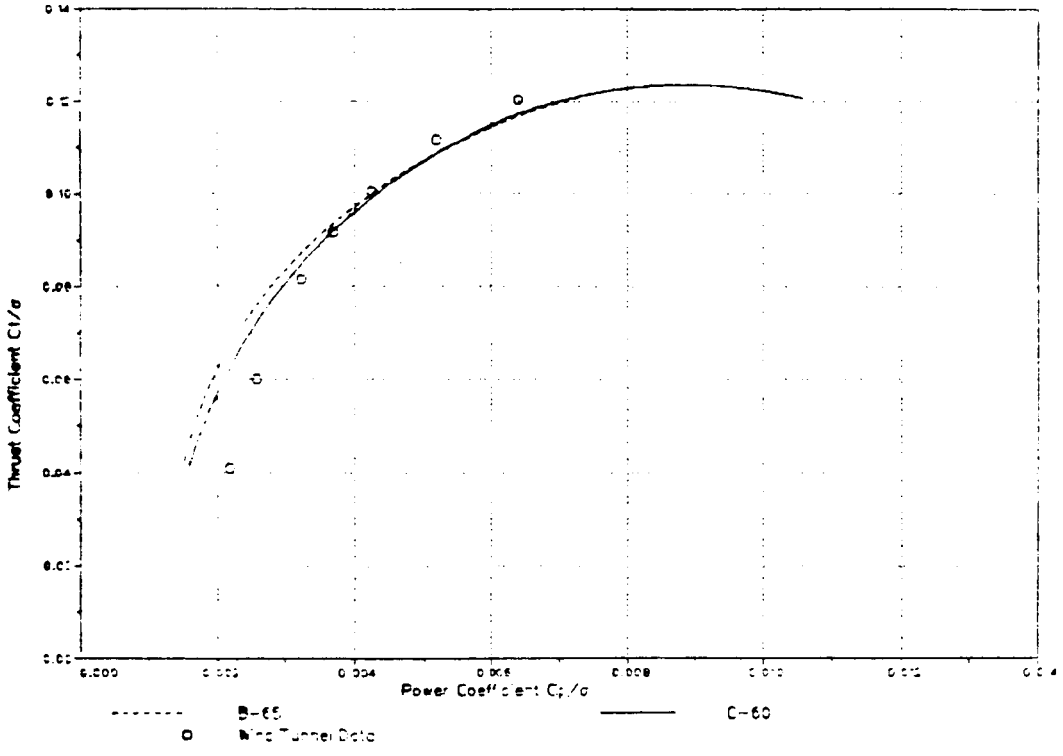

Figure 5-13 Comparision of B-65 and C-60, Lift-Drag Ratio

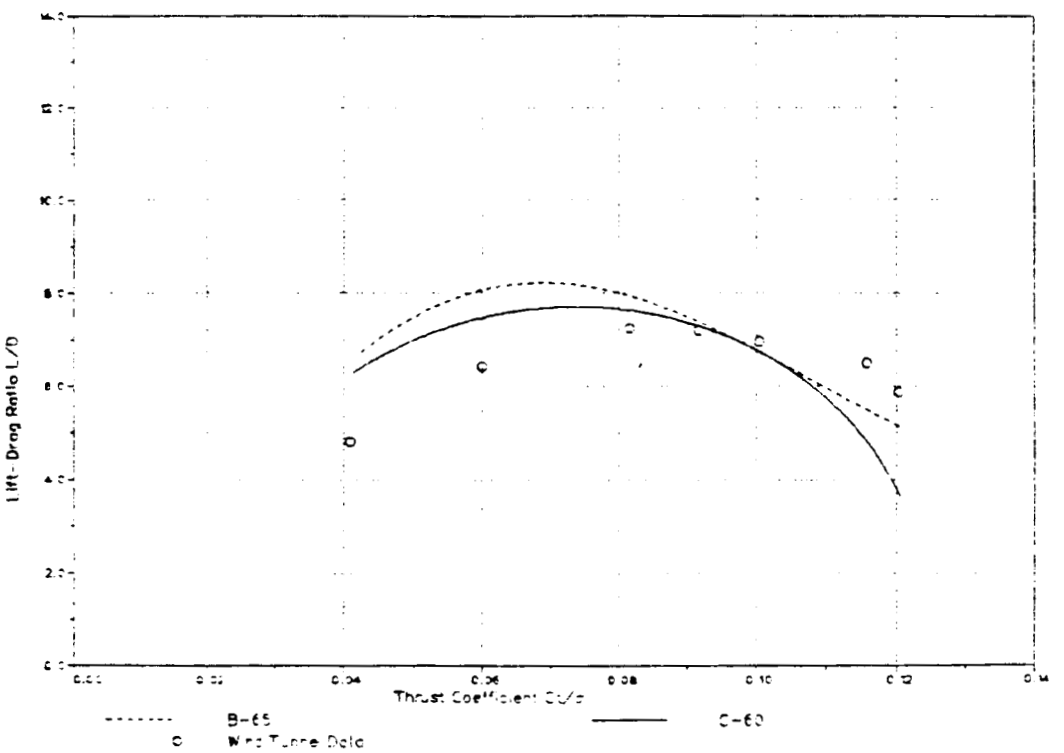

Figure 5-14 Conventional Rotor Power Requirement $\mu \approx 0.3$, $\alpha_{shaft} \approx -7^o$

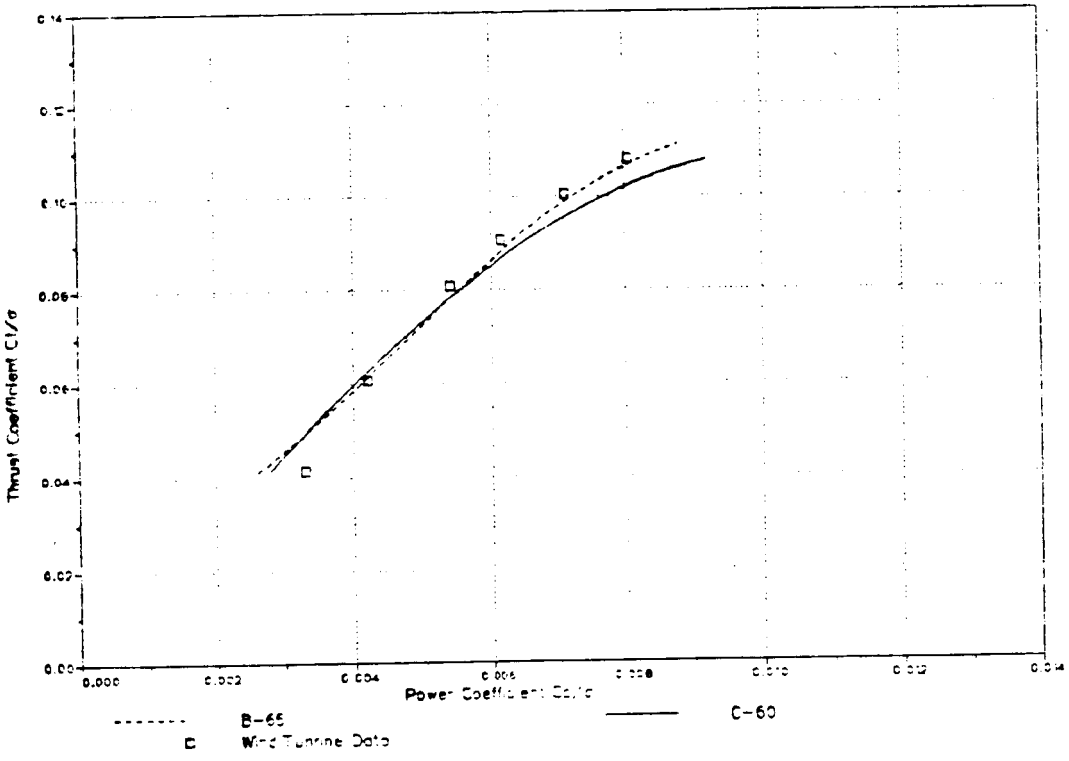

Figure 5-15 Conventional Rotor Lift-Drag Ratio $\mu \approx 0.3$, $\alpha_{shaft} \approx -7^o$

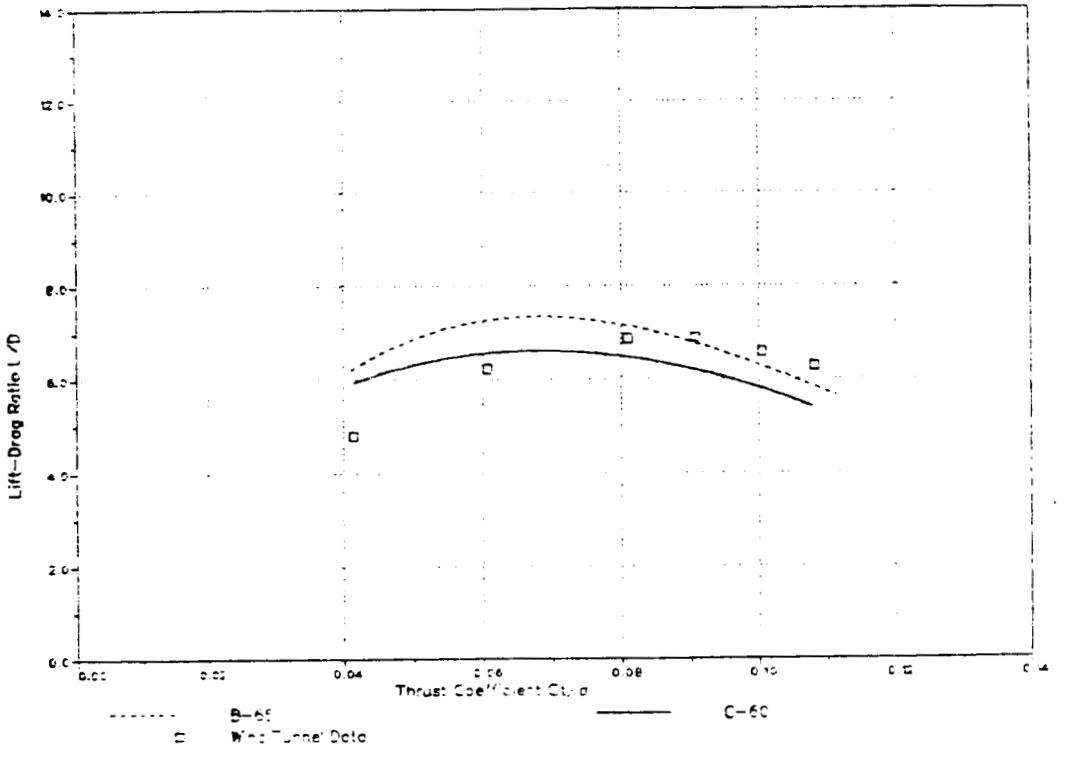

prediction becomes larger in low and high thrust regions, the analysis of the Free-Tip and comparisons of its results with the conventional rotor for the FTR performance assessment should be done in the moderate thrust region ($0.06 \leq C_T/\sigma \leq 0.10$).

5.5. Results.

For the FTR II performance assessment, the above trim conditions with $C_T/\sigma \approx 0.08$ were selected for a base line configuration. The trim parameters are

$$\begin{aligned} T &= 1717.47 \quad (lb) \\ X &= 132.98 \quad (lb) \\ Y &= -27.36 \quad (lb) \end{aligned}$$

The corresponding control input is

$$\begin{aligned} \theta_{0.75} &= 10.621^o \\ \theta_{1c} &= -0.255^o \\ \theta_{1s} &= 5.120^o \end{aligned}$$

Its resulting flapping and performance parameters are

$$\begin{aligned} \beta_0 &= 4.411^o \\ \beta_{1c} &= 2.095^o \\ \beta_{1s} &= 1.280^o \\ C_P/\sigma &= 0.00533 \\ L/D &= 7.240 \end{aligned}$$

Figure 5-16 shows a lift distribution over the blade at $\psi = 90^o$ and $\psi = 180^o$. The lift distribution on the tip around the azimuth is given in Figure 5-17.

For the first series of analysis, V23010-1.58 airfoil ,which is the airfoil used in the base line configuration, was used with a tab deflection to

Figure 5-16 Spanwise Lift Distribution, Conventional Rotor

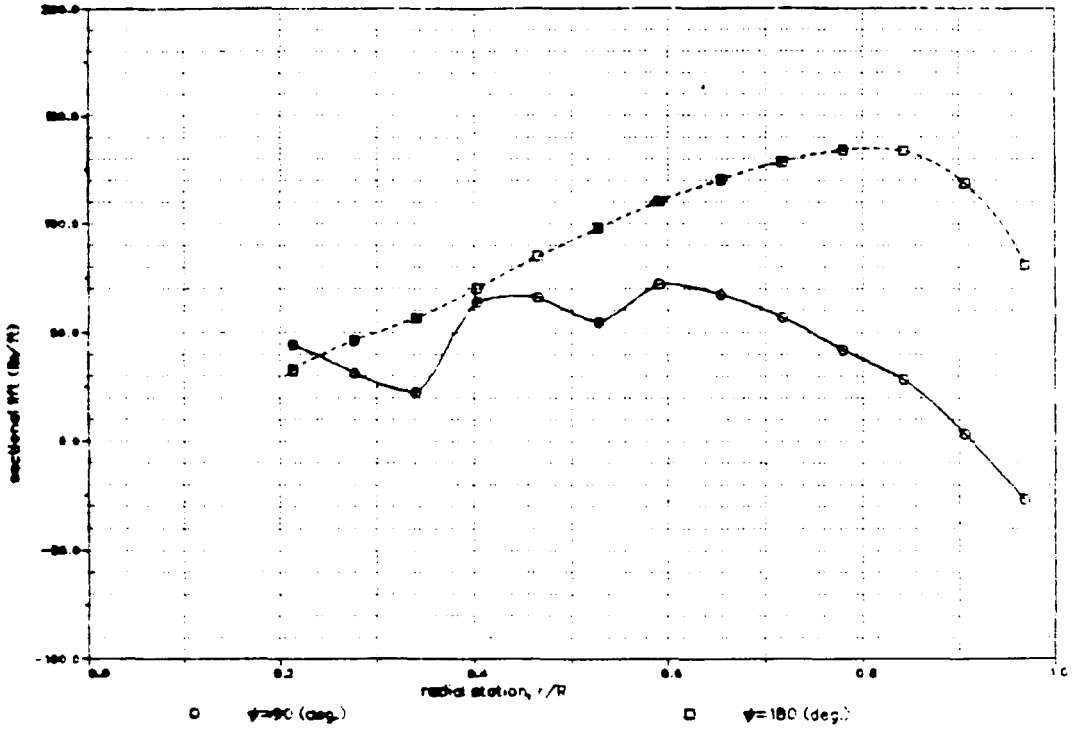

Figure 5-17 Azimuthal Lift Distribution, Conventional Tip

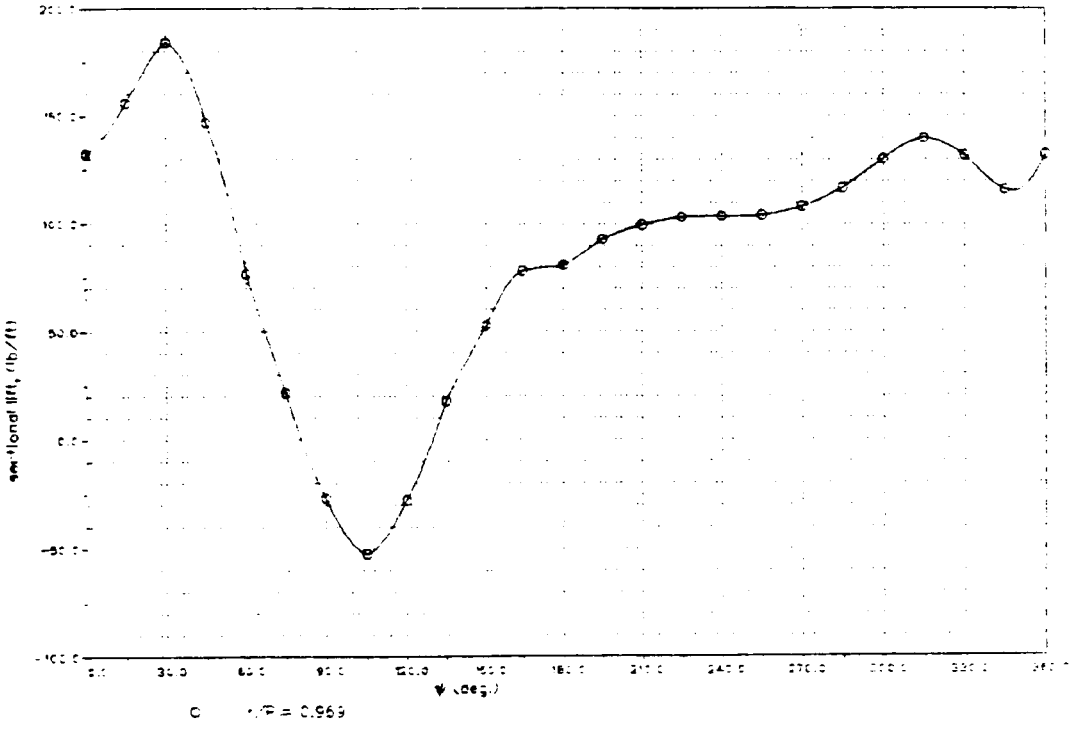

show the effect of airfoil pitching moment. In this analysis, neither drag penalty, nor a lift curve slope correction due to the tab deflection were applied. Three levels of control moment were imposed on the tip. The helix angle of the controller was adjusted so that its resulting moment output corresponds to $q_0 = 5$ $(ft\ lb)$, $q_0 = 7.5$ $(ft\ lb)$ and $q_0 = 10$ $(ft\ lb)$. All parameters that define the physical size of the inboard section were unchanged. Cyclic and collective pitch were adjusted until the rotor reaches the same trim conditions described in the previous section.

Figures 5-18 and 5-19 present the effect of Δc_{m_0} on the power coefficient and lift-drag ratio. The dashed line merely indicates the level of C_P/σ and L/D respectively for a rotor with a conventional tip and does not represent a tip with variable Δc_{m_0}.

For a given amount of control moment, there is one value of Δc_{m_0} which optimizes C_P/σ and L/D. When Δc_{m_0} is small, the tip does not produce enough cyclic moment for a longitudinal trim. As Δc_{m_0} increases, the longitudinal cyclic pitch requirement for the inboard section becomes small due to the increased cyclic moment, generated by the tip. This reduces the sectional drag on the inboard section, which leads to a lower C_P/σ and higher L/D. When Δc_{m_0} exceeds the optimum point, the pitch angle of the tip becomes more negative, which results in a higher sectional drag and more negative mean lift on the tip. And as a result, the power requirement increases and lift-drag ratio decreases.

However, in all three cases with different control moment, the performance of the FTR II at the each optimum point is inferior to the conventional rotor.

Its reason can be seen in Figure 5-20, which presents a longitudinal cyclic pitch control requirement of the inboard section, θ_{1s}. It shows that the cyclic moment generated by the tip does contribute to reducing the inboard section cyclic pitch requirement. However, the amount of the cyclic moment contribution from the tip is not large enough to reduce the inboard section cyclic pitch below the level of the conven-

Figure 5-18 Free-Tip Rotor Power Requierment, V23010-1.58

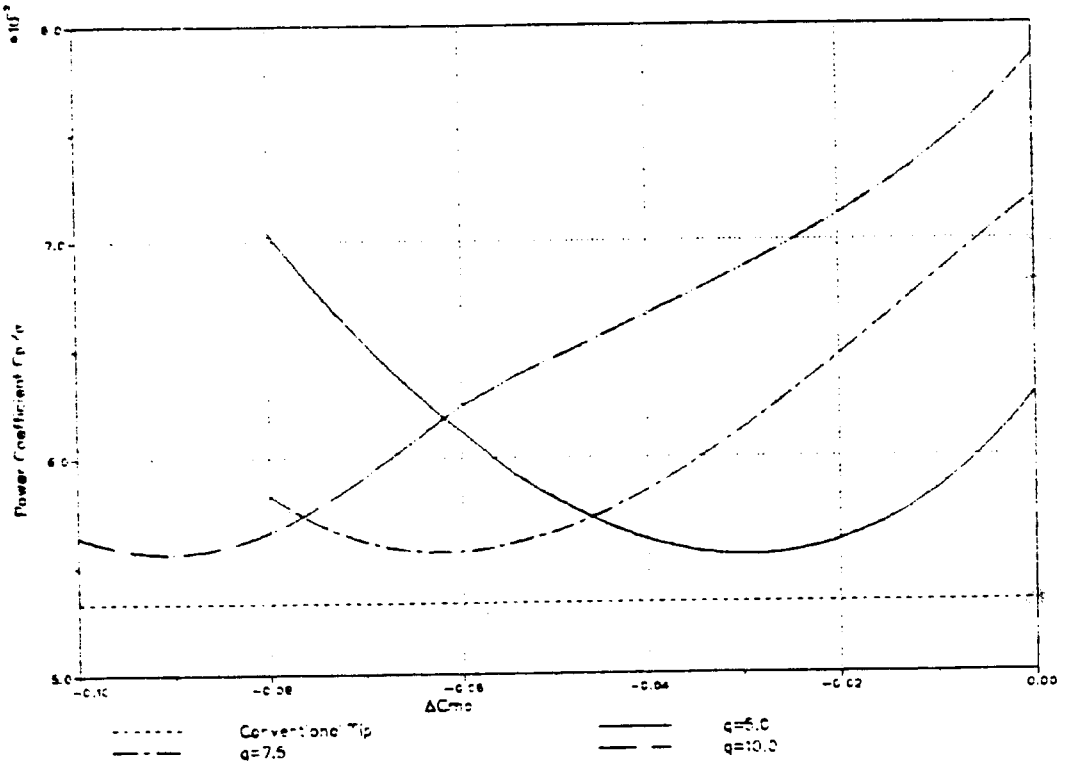

C-2

Figure 5-19 Free-Tip Rotor Lift-Drag Ratio, V23010-1.58

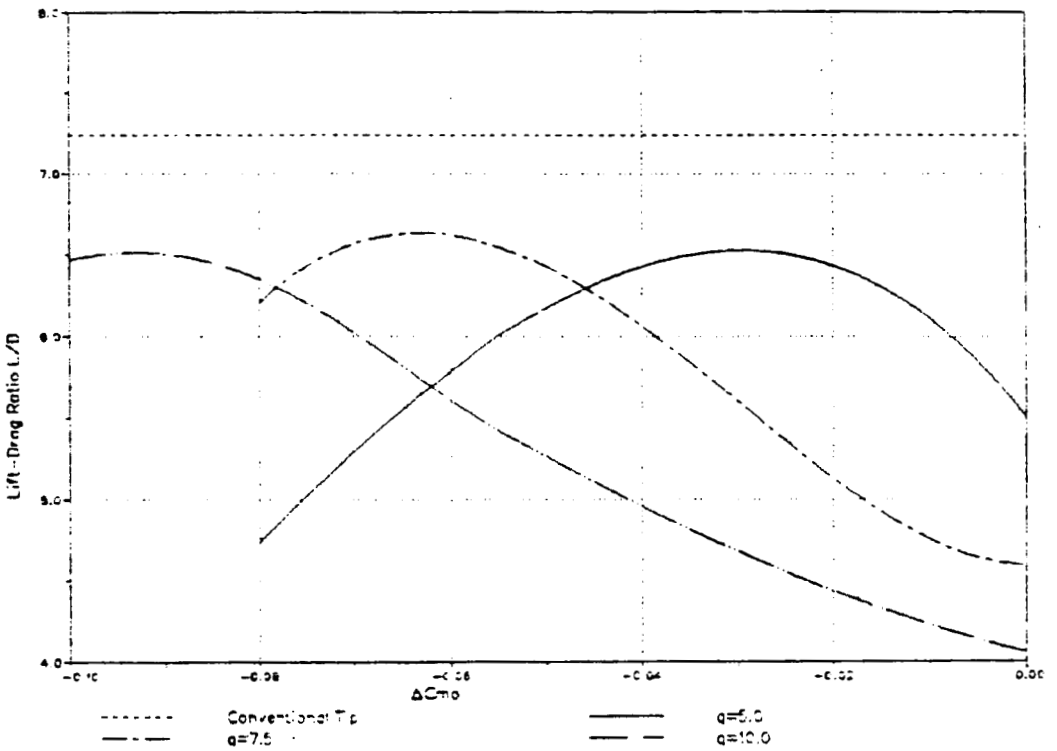

Figure 5-20 Inboard Section Longitudinal Cyclic Pitch Control Input

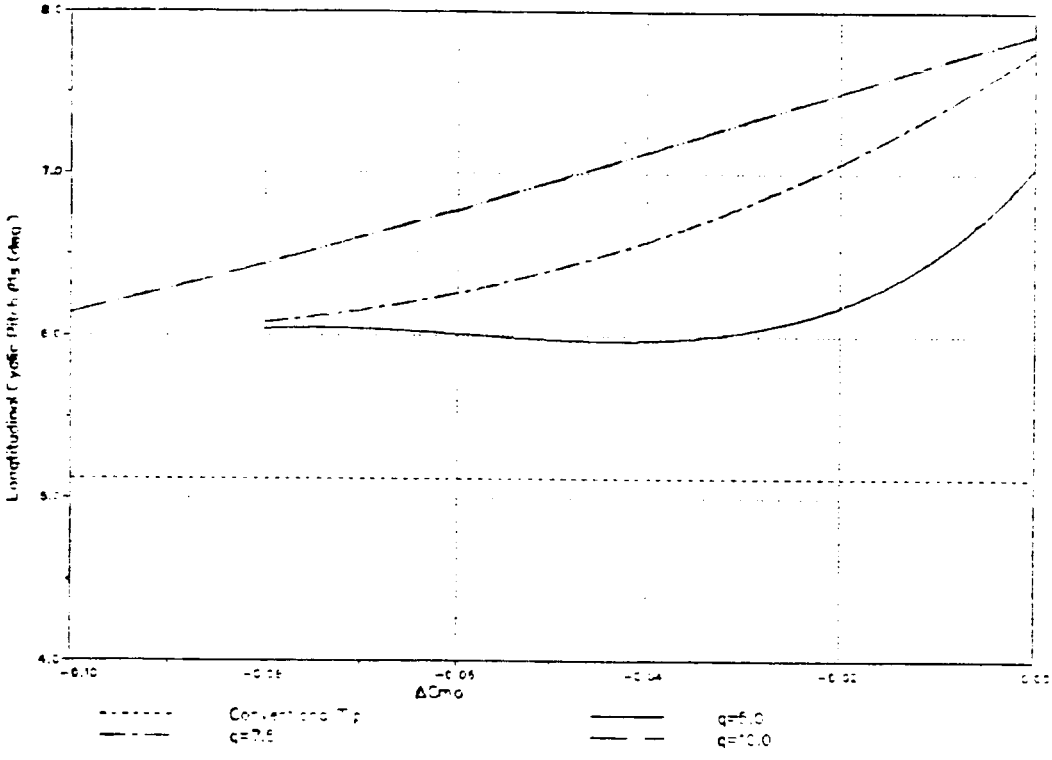

tional rotor. This results in a higher sectional drag on the inboard section.

The lift distribution on the tip with $\Delta c_{m_0} = -0.04$ around the azimuth is presented in Figure 5-21. The lift variation around the azimuth, which results in the cyclic moment, is much less than what was expected from the results of two dimensional analysis. (See Figure 4-2a. Note that there are differences in the physical dimensions and the flight condition between two models.)

It was found that the lift distribution on the tip was strongly influenced by the shed vortices from the junction of the tip and the inboard section, which was ignored in the AZIMUTH and FTR2 programs. The influence of the shed vortices can be best described by an induced velocity distribution over the blade. Figure 5-22 shows an azimuthal distibution of the induced velocity component normal to the airfoil chord line, v_N (positive down) for a conventional blade at the radial computation points at $r/R = 0.906$, which is the most outboard station on the inboard section, and at $r/R = 0.969$, the station on the tip. Note that the difference in the downwash component between two points is small. The downwash distribution for the FTR II at the same computation stations is given in Figure 5-23. It shows a strong upwash component at the tip, which is being generated by the trailing vortices shed from the junction between the inboard section and the tip. This upwash makes the local angle of attack at the tip more positive, so that the tip cannot carry enough negative lift to produce the cyclic moment.

The tip itself is a wing with a small aspect ratio. Therefore, when the tip pitches down to create the negative lift, its own contribution to the upwash is also large.

The amount of the upwash may be exaggerated because of the primitive wake model. As it was described in the previous section the airfoil surface boundary condition is not being checked in the program. In addition to that, the vortex element used in the downwash computation does not have a finite sized core. Therefore, the induced velocity computation in the vortex core proximity is unrealistic (Reference 28). Since the Free-Tip

Figure 5-21 Azimuthal Lift Distibution on a Free-Tip

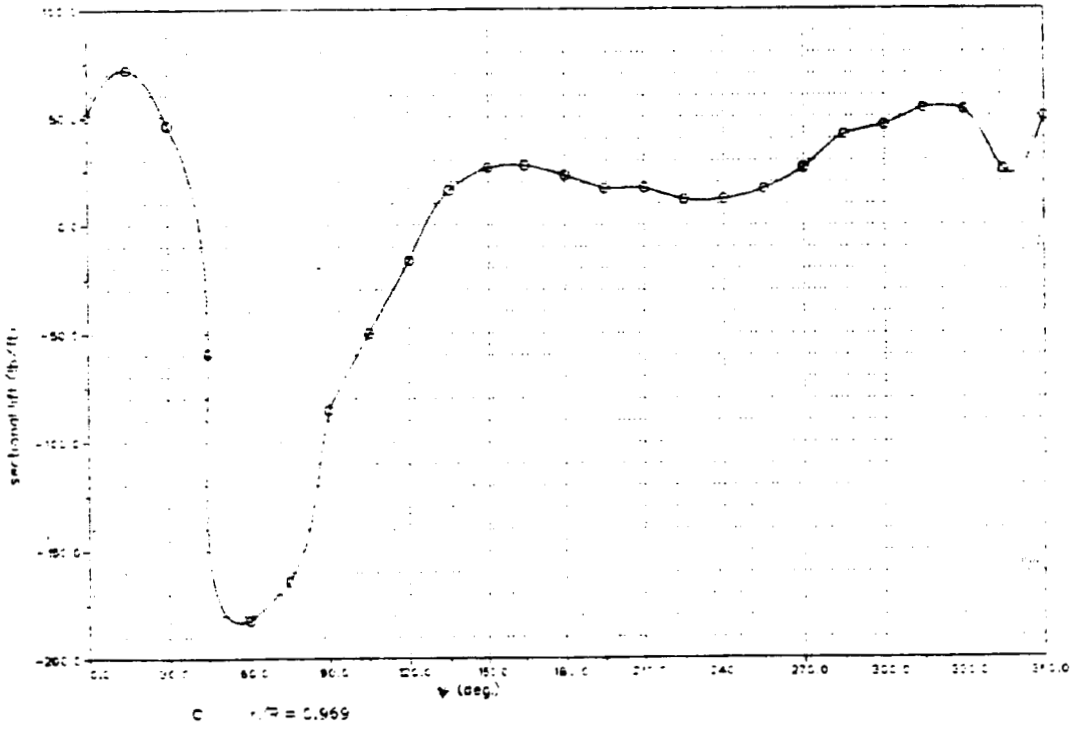

Figure 5-22 Downwash Component, Conventional Tip

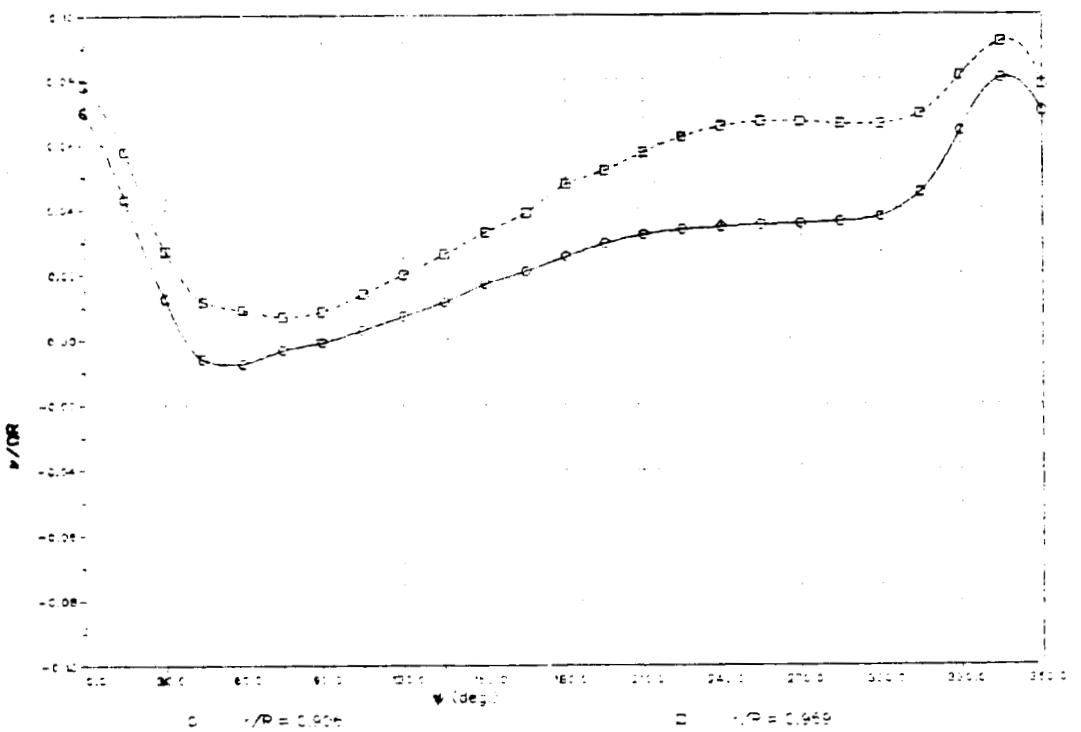

Figure 5-23 Downwash Component, Free-Tip

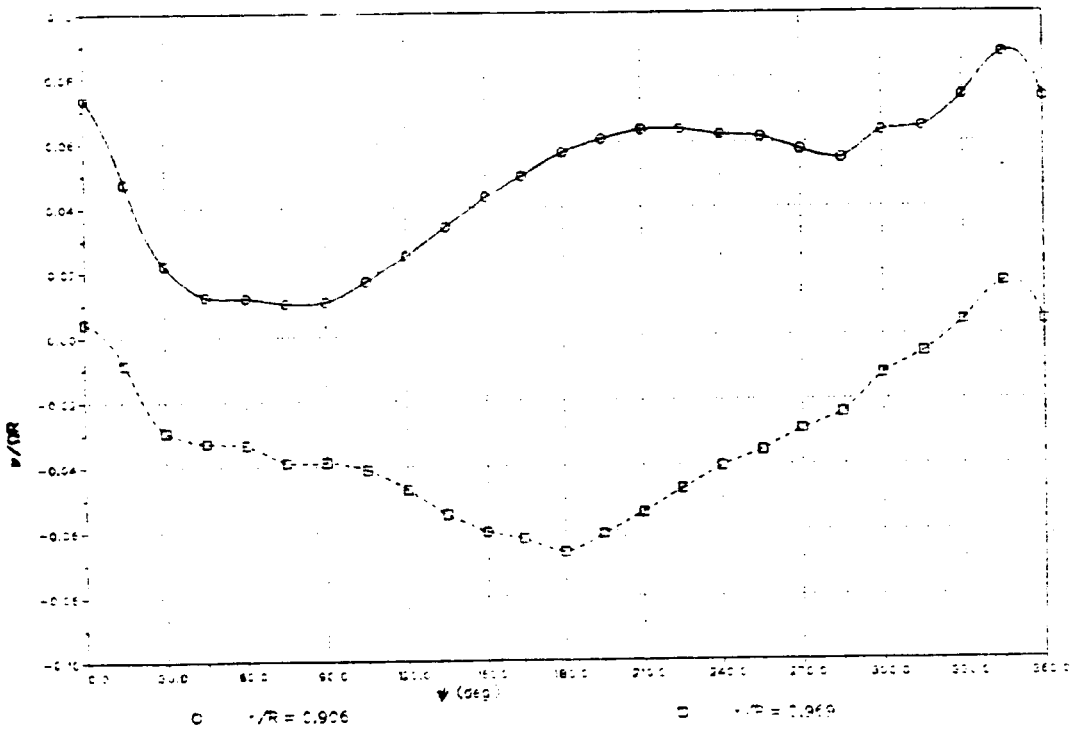

is located next to the strong vortex shed from the junction, the upwash component computed in the program may be much larger than that in reality.

This vortex model seems to be good enough to compute the rotor performance parameters of a conventional rotor in low thrust region because such a local inaccuracy (inaccuracy in local blade section) tends to be negligible. This is perhaps because in the absence of a control surface in the proximity of strong shed vortices, any modeling inaccuracy in the tip region would be much smaller than that of the FTR configuration.

To verify the downwash distribution model, a comparison with the experimental data is desirable. However, the downwash distribution over the rotor disk largely depends on the physical configuration, flight condition and trim parameters (Reference 29). In other words, the wake measurement for this particular configuration is necessary.

Since such experimental data were not available, it was decided that the current parametric study should be continued with the present wake model because it should still indicate the effects of some important parameters, although the cyclic moment generated by the Free-Tip may be somewhat less than what can be expected in reality.

V23010-1.58 airfoil on the tip section was replaced by MS(1)-0313 airfoil. The results with three levels of control moment are shown in Figures 5-24 and 5-25. The maximum L/D and minimum C_P/σ were slightly improved, although, the conventional rotor still shows a superior performance. The maximum performance can be achieved with no tab deflection and the lowest control moment.

To show the Δc_{m_0} effect due to the tab deflection, the longitudinal flapping, β_{1c} and the resulting propulsive force, X are presented in Figures 5-26 and 5-27 respectively. The longitudinal cyclic pitch control input of the inboard section was fixed to $\theta_{1s} = 6.91^o$. Note that the shaft of the rotor is being tilted forward for approximately 7^o. The contribution of the tip, which tilts the rotor disk to generate the higher propulsive force, can be seen.

Figure 5-24 Free-Tip Rotor Power Requirment, MS(1)-0313

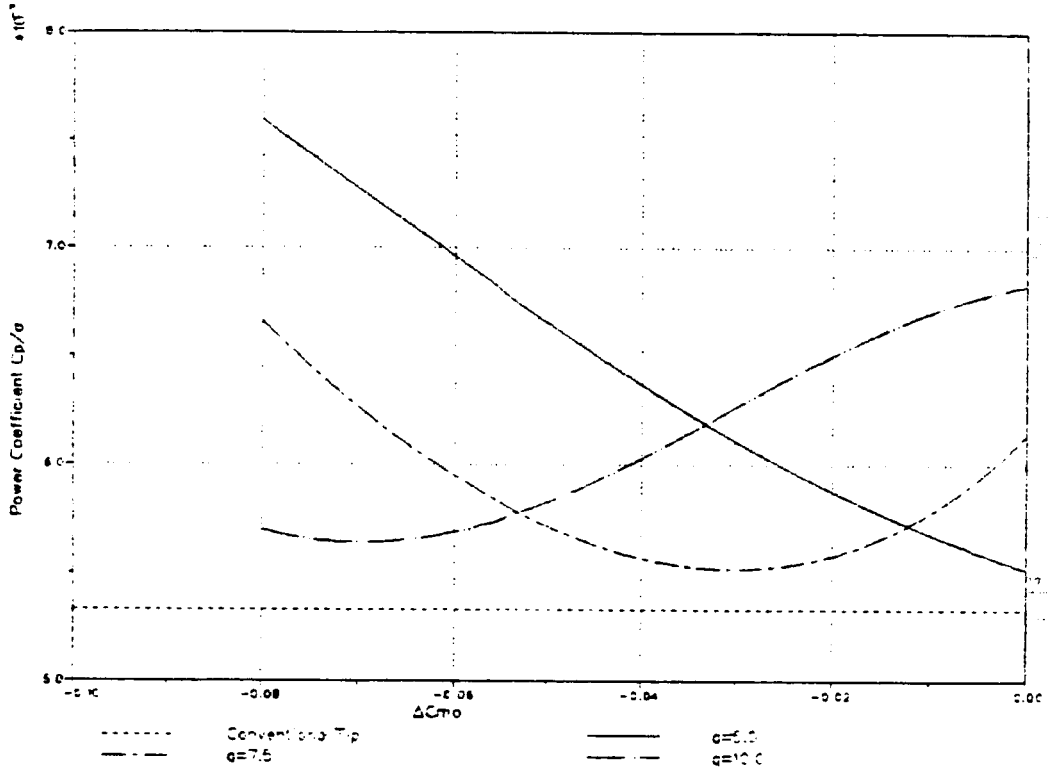

Figure 5-25 Free-Tip Rotor Lift-Drag Ratio, MS(1)-0313

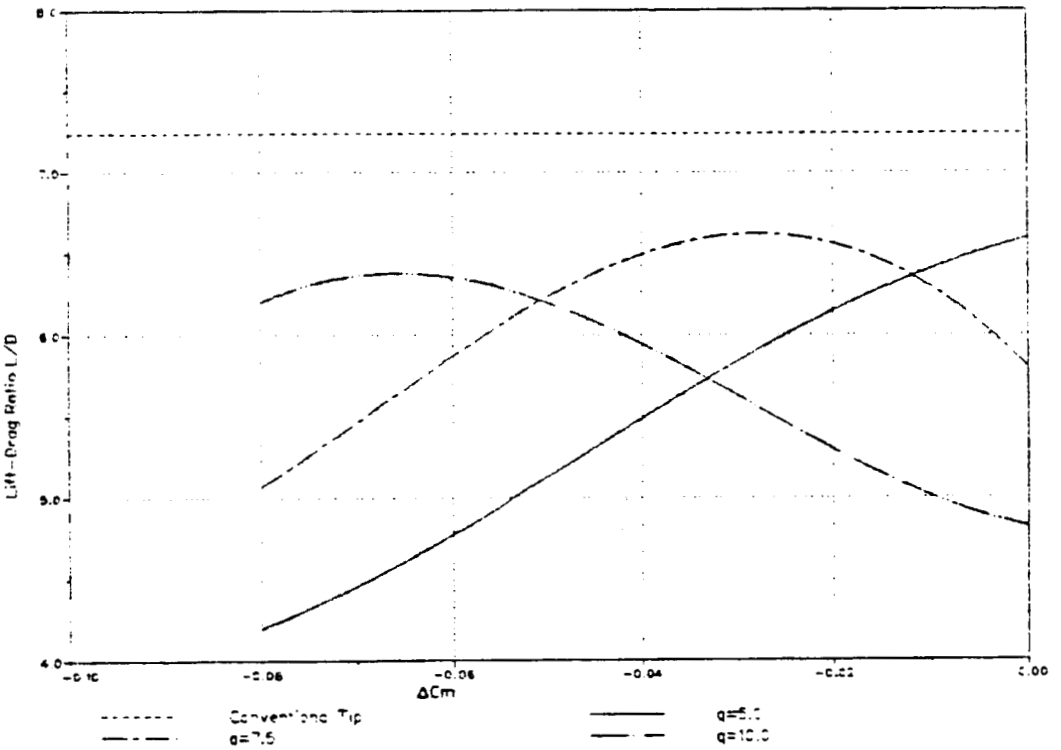

Figure 5-26 Longitudinal Flapping due to Free-Tip

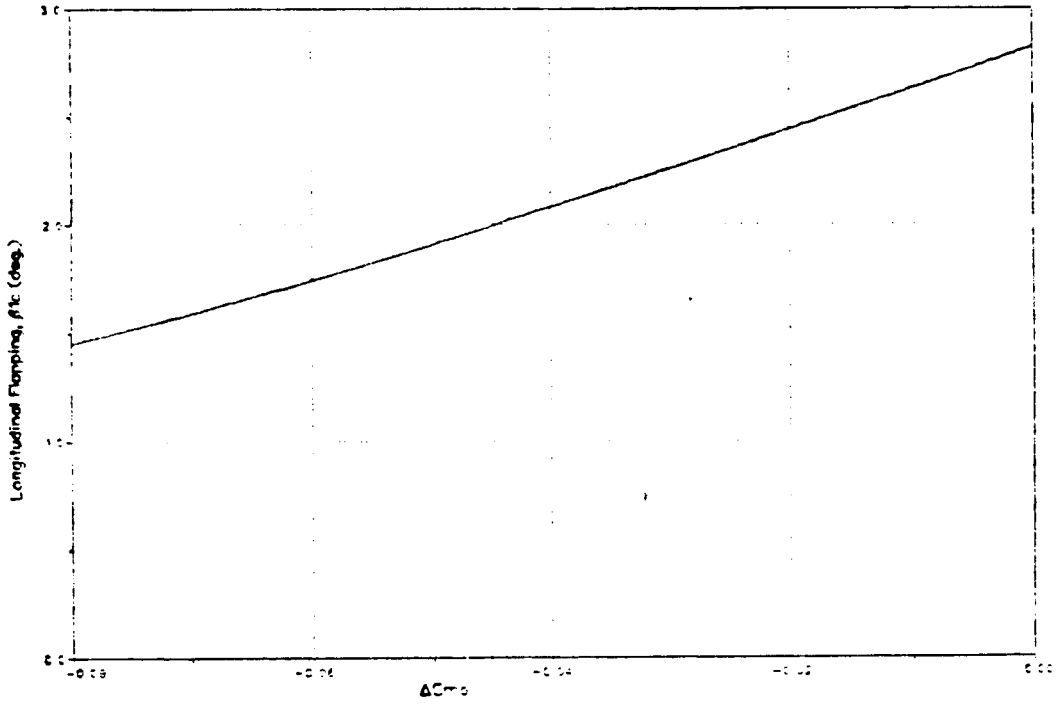

Figure 5-27 Propulsive Force due to Free-Tip

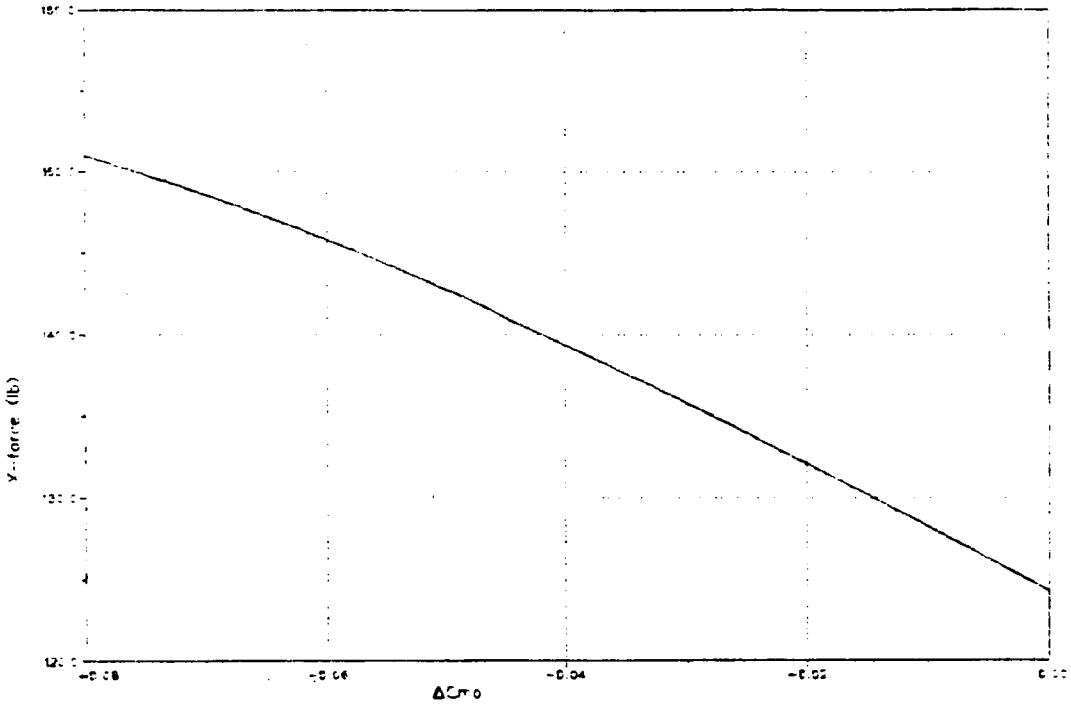

The original blades has a linear twist of -9.45^o. Generally speaking, a large blade twist improves the total rotor performance by delaying the stall (Reference 30). Since the FTR II configuration has a structurally decoupled tip, the twist of the inboard section can be increased significantly without introducing a oscillatory lift loading with a large amplitude on the tip.

A larger twist also contributes to reduce the strength of the trailing vortex shed from the outboard end of the inboard section by making the local angle of attack at that section smaller. The amount of upwash, ν_N, is shown in Figure 5-28 as a function of the linear blade twist angle, θ_{tw}. It shows that the reduction of upwash levels off beyond $\theta_{tw} = -14^o$. When the twist was increased to -15^o, the sectional lift on the most outboard computation point of the inboard section becomes near zero as indicated in Figure 5-29. Therefore, it is considered that the maximum linear twist that can be applied to be $\theta_{tw} = -15^o$.

Figures 5-30 through 5-33 show the results of C_P/σ and L/D for $\theta_{tw} = -13^o$ and $\theta_{tw} = -15^o$. An improvement on C_P/σ and L/D is clearly shown. With $\theta_{tw} = -15^o$, $q_0 = 5(ft\ lb)$ and $\Delta c_{m_0} = 0.00$, the power requirement of FTR II is 3.2% less than that of a conventional rotor, while its L/D was improved by 0.5%.

A large twist not only improves C_P/σ and L/D but also alleviates the blade bending moment by shifting the lift inboard. Since the current configuration employs an articulated rotor, a change in the average blade bending moment can be seen as a variation of the coning angle, β_0. The coning angle is shown as a function of the blade twist in Figure 3-34 which indicates the reduction of the coning angle as the blade twist becomes more negative.

A nonlinear blade twist was also applied to the inboard section. It is a combination of two linear twist distributions which was adjusted as follows. From 0% to 60% of the blade, it has a linear twist of $\theta_{tw} = -9.45^o$. At 90% of the blade, the geometric pitch angle of the blade

Figure 5-28 Downwash Variation due to Inboard Twist

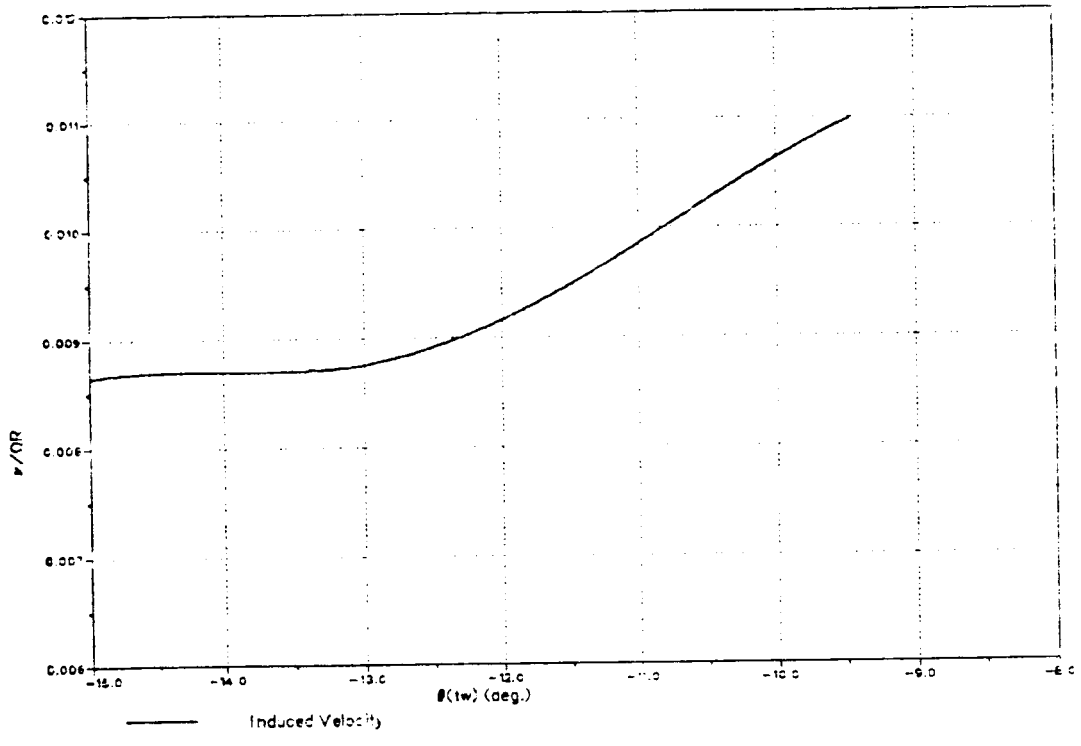

Figure 5-29 Spanwise Lift Distribution, Free-Tip, $\theta_{tw} = -15^o$

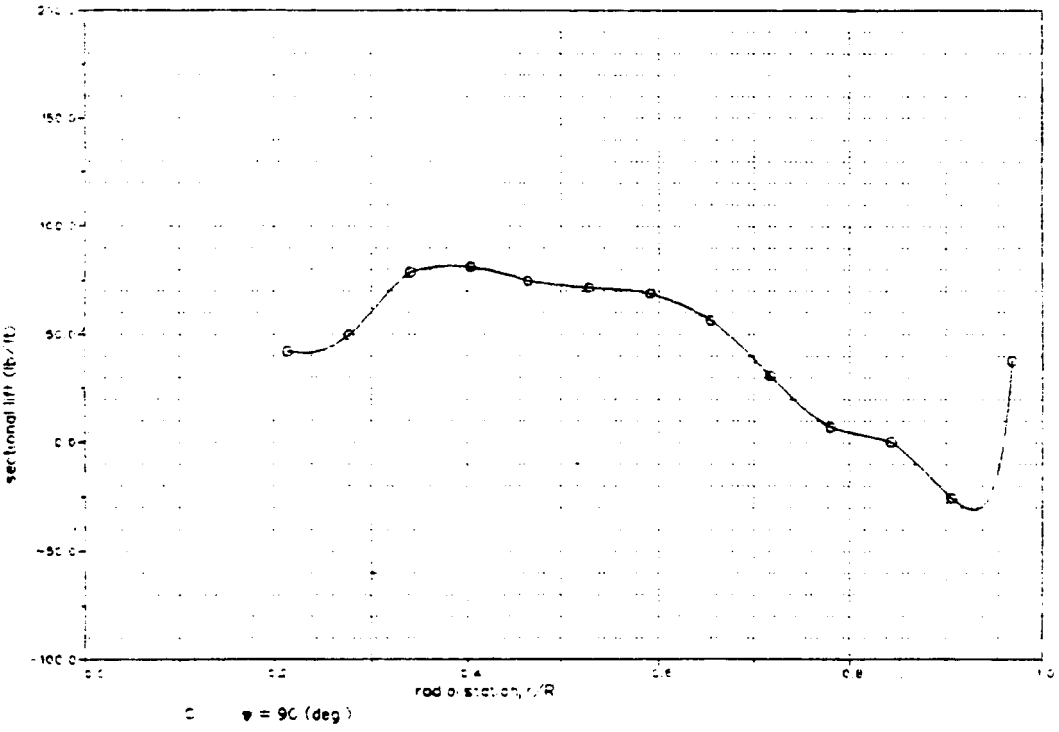

Figure 5-30 Power Requierment, $\theta_{tw} = -13^o$, MS(1)-0313

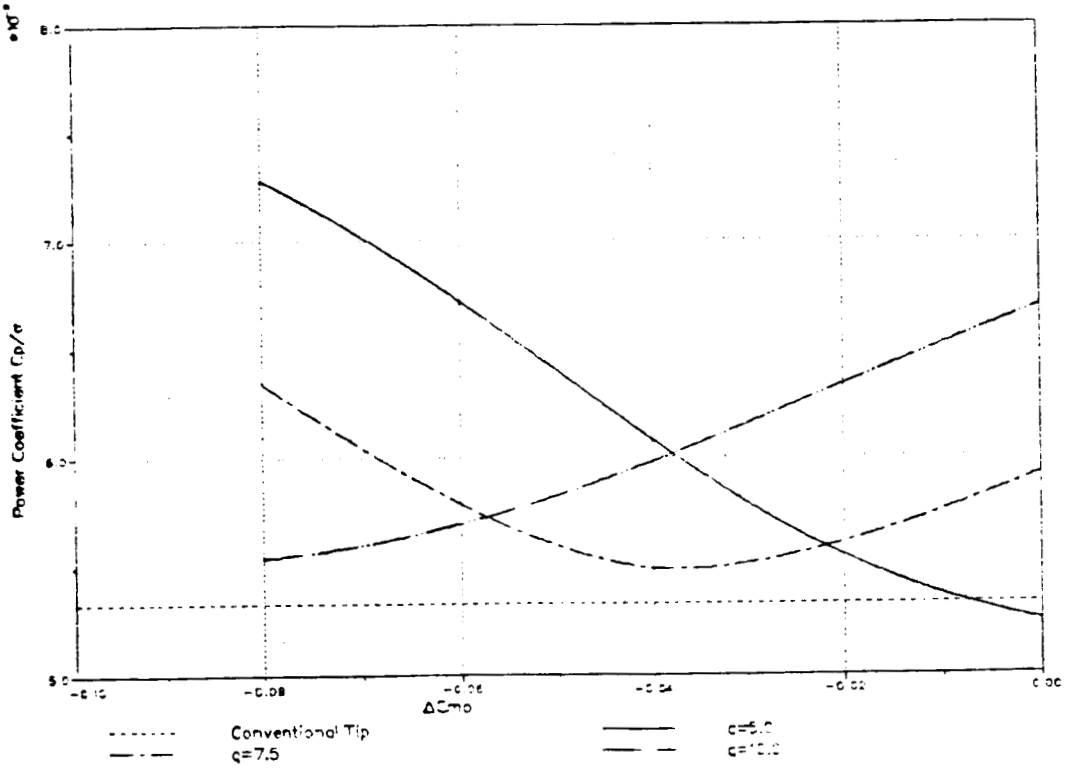

Figure 5-31 Lift-Drag Ratio, $\theta_{tw} = -13^o$, MS(1)-0313

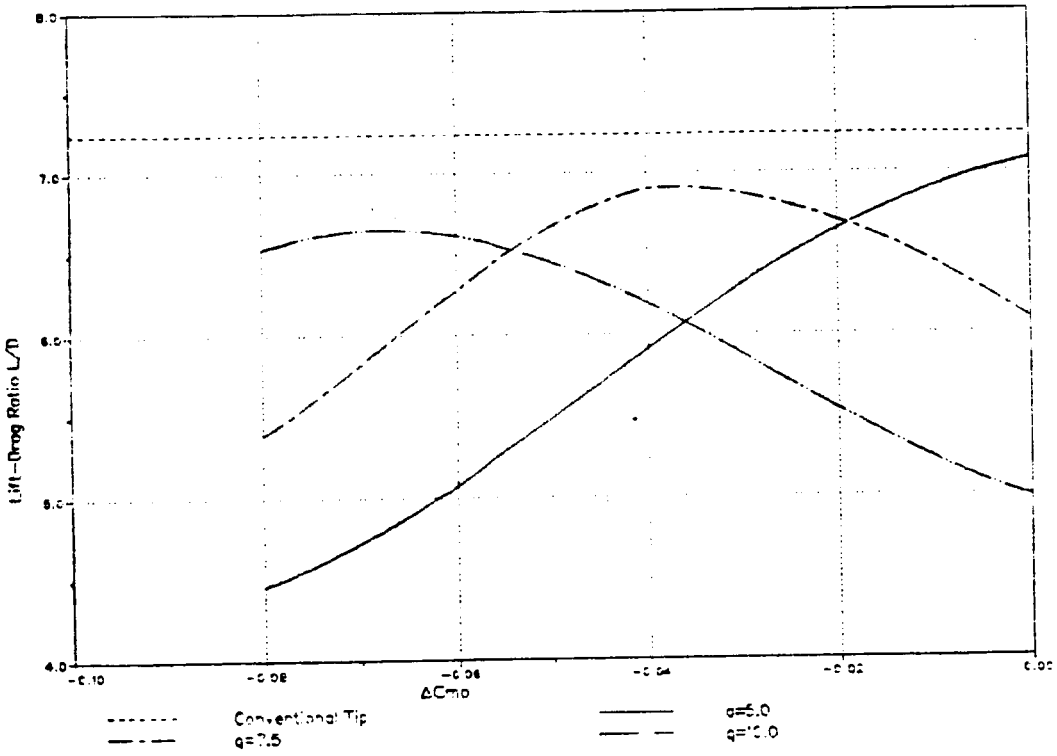

Figure 5-32 Power Requierment, $\theta_{tw} = -15^{o}$, MS(1)-0313

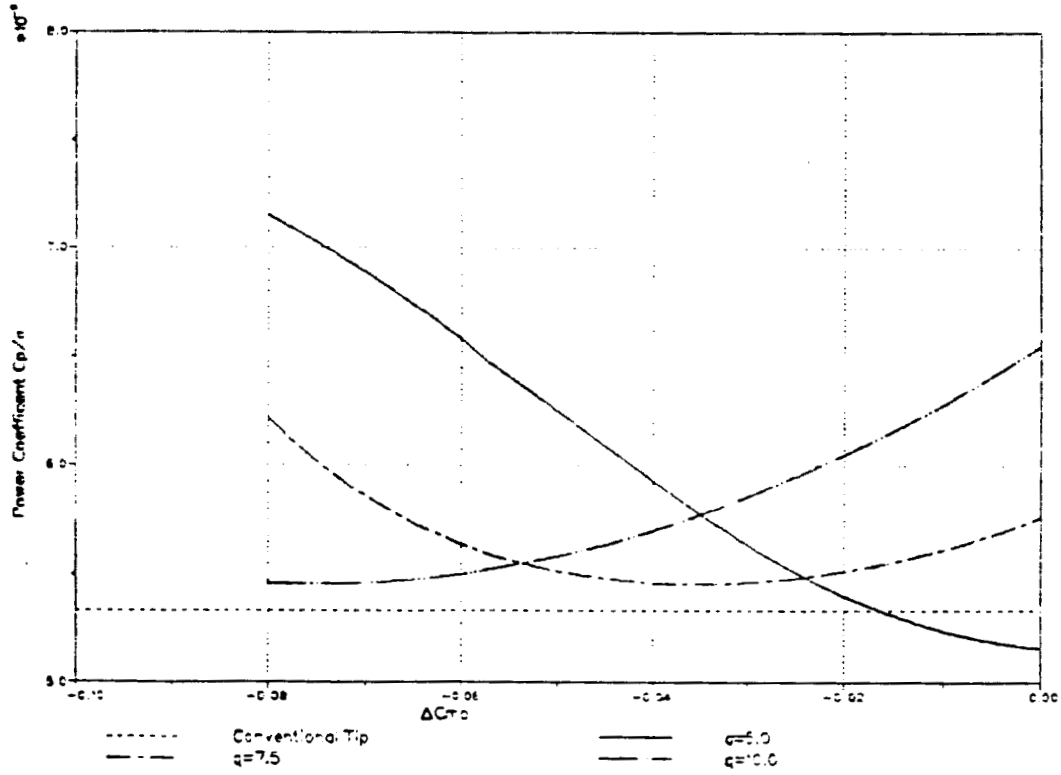

Figure 5-33 Lift-Drag Ratio, $\theta_{tw} = -15^{o}$, MS(1)-0313

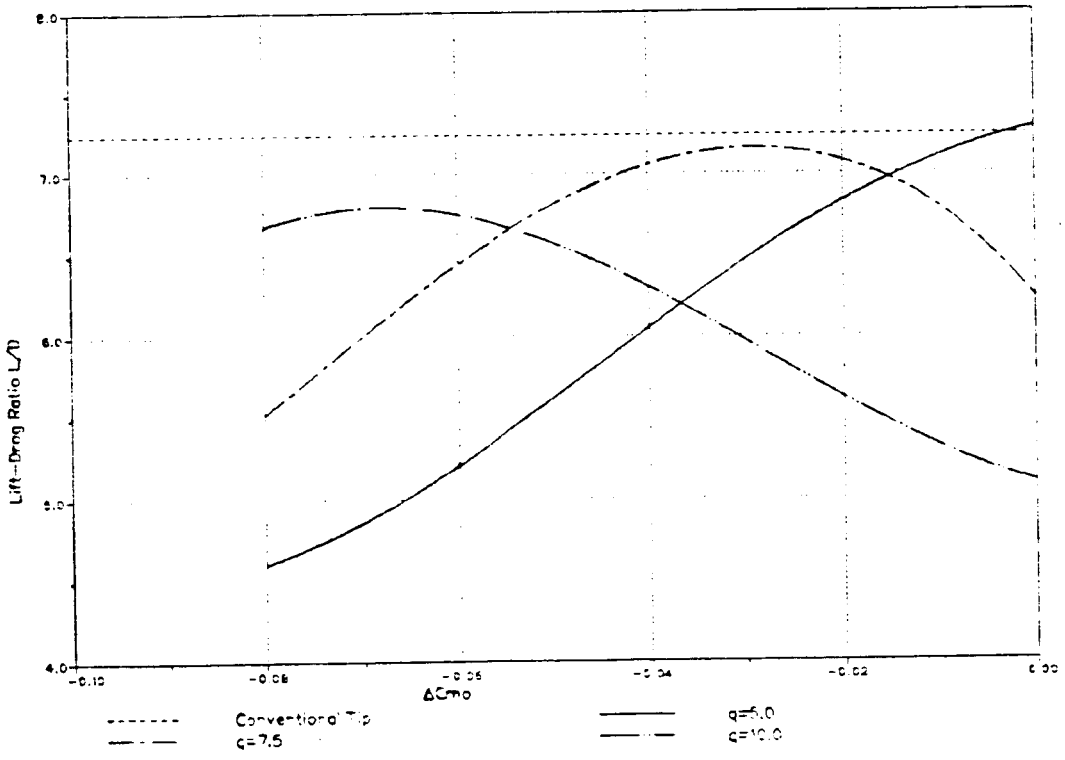

Figure 5-34 Effect of Inboard Twist on the Coning Angle

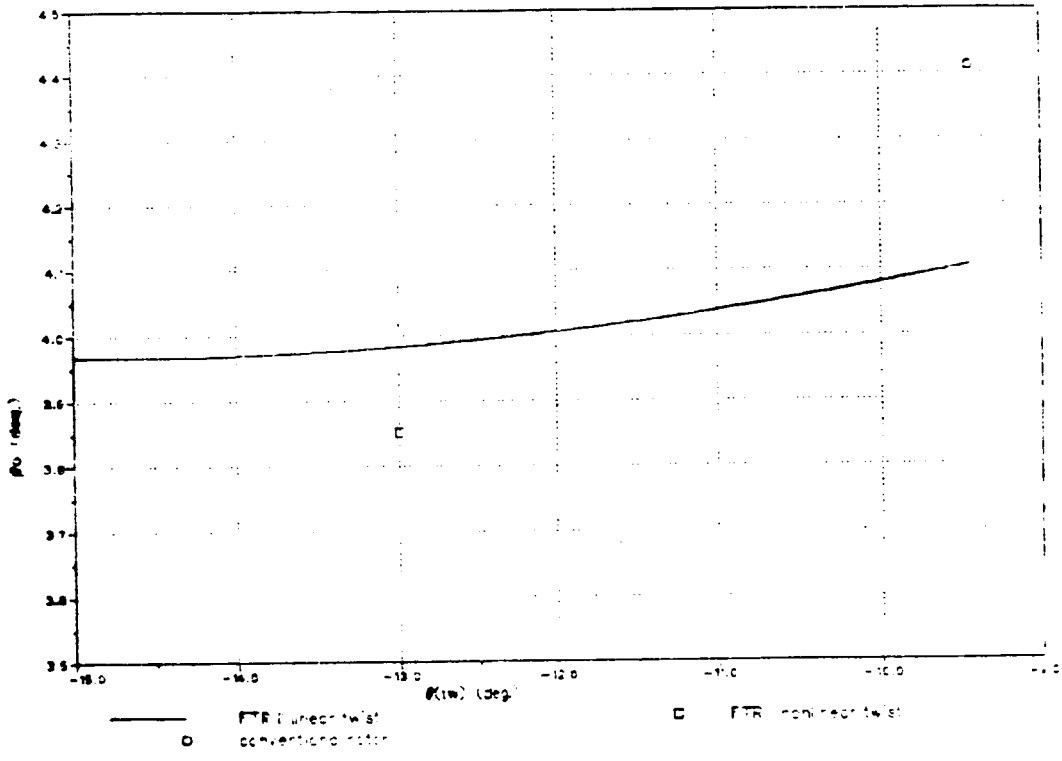

section was set to be the same as the blade with $\theta_{tw} = -15^o$. The twist between 60% and 90% blade stations was obtained by a linear interpolation. This twist distribution is shown in Figure 5-35 together with the three linear twist distributions used in the previous analysis.

It was found that the performance of the blade with this nonlinear twist distribution is very similar to the one with $\theta_{tw} = -13^o$, as indicated in Figures 5-36 and 5-37. The resulting coning angle, β_0 was smaller than any linear twist because this particular twist distribution shifts the lift loading even further. The amount of coning angle is indicated in Figure 5-34.

A difficulty was encountered in flapping convergence when the flight speed was increased ($\mu \approx 0.5$) or when the Free-Tip span was increased more than 10%. In both cases, the moment generated by the Free-Tip becomes greater and it causes a "flapping instability". This "instability" should not be confused with the flap-lag elastic instability or the flapping divergence due to high μ. In this case the blade takes a different path each time it revolves because the lift on a tip, which results in the cyclic moment, is coupled with the flapping, particularly, $\frac{d\beta}{dt}$. Therefore, it is impossible to define a steady tip path plane. Since B-65 is not designed for a transient motion analysis, when it happens, the program yields no solution.

5.6. Conclusions.

The analysis indicated that the numerical result of the FTR II performance index may be somewhat less than reality because of the problem associated with the primitive model of the trailing vortex shed from the junction of the Free-Tip and the inboard section.

It was shown that the uniform-loading type airfoil is a suitable airfoil for the tip section because it gives a sufficient amount of pitching moment which induces a once-per-revolution pitching motion of the tip

Figure 5-35 Twist Distributions

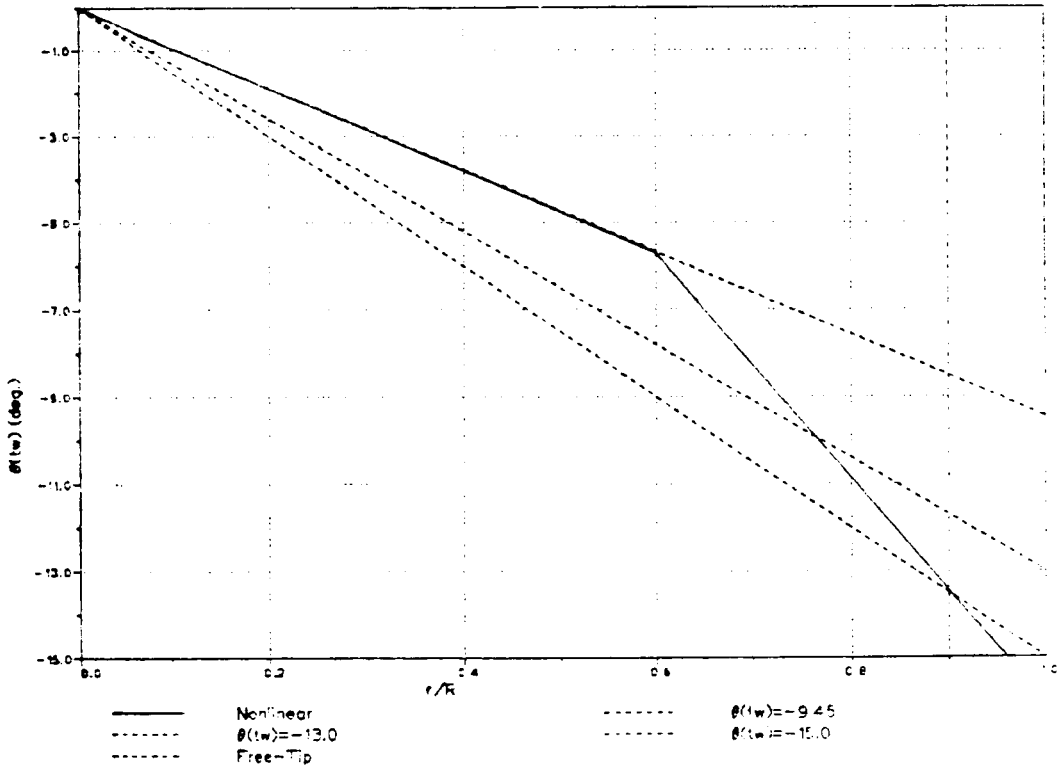

Figure 5-36 Power Requirement, Non-linear Twist

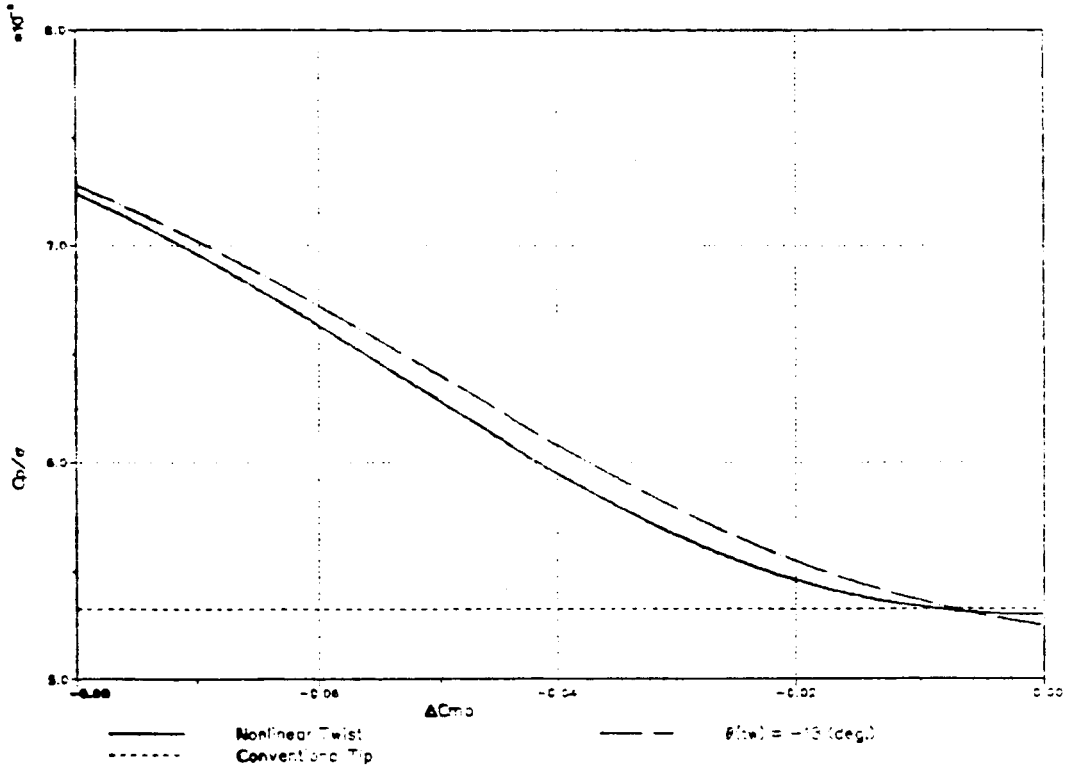

Figure 5-37 Lift-Drag Ratio, Non-linear Twist

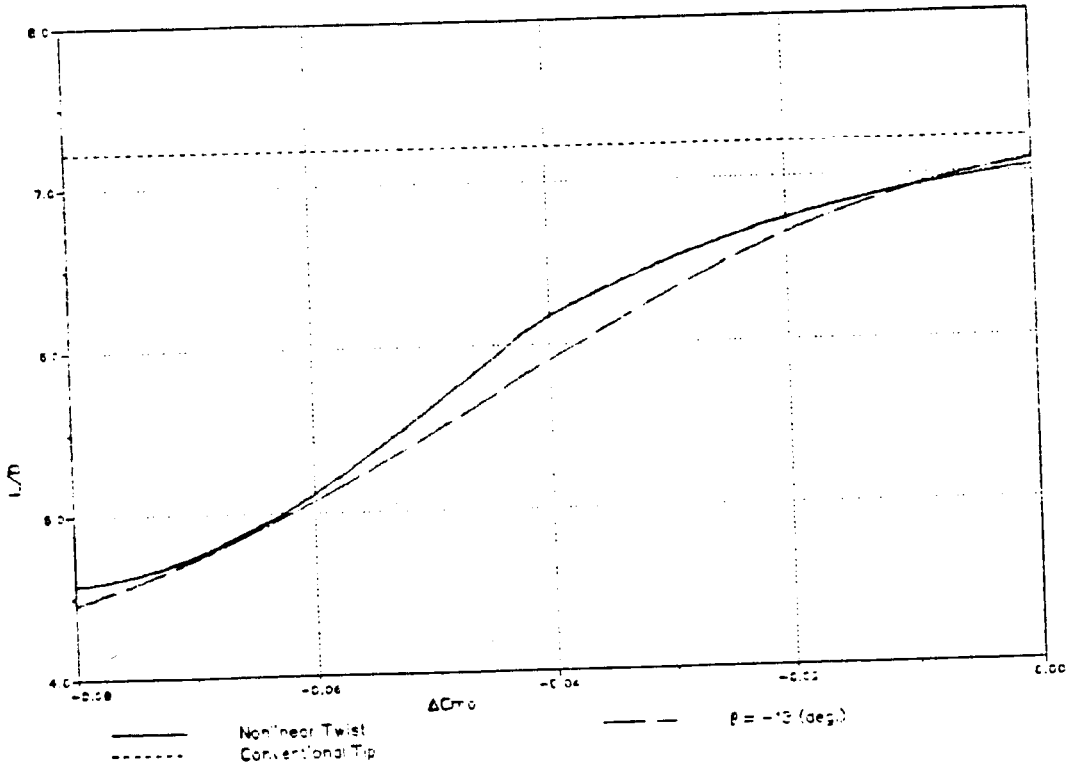

to generate the cyclic moment. It also has a lower drag in all operating range and higher drag divergence Mach number than a conventional airfoil.

The FTR II configuration allows a large twist on the rotor blade inboard section, without complication of vibratory load on the tip. The higher twist rate also alleviates the blade bending moment by shifting the lift loading inboard. A nonlinear twist can be used to lessen the bending moment even further.

The final configuration, which has MS(1)-0313 airfoil and a rectangular planform for the tip with the inboard section with its twist being -15^{o}, resulted in a performance improvement over a conventional rotor for 3.2% in power requirement and 0.5% in lift-drag ratio.

6. Concluding Remarks and Recommendations

A parametric study of Free-Tip Rotor was performed by means of numerical analysis. The tip response analysis of the Constant Lift Tip Rotor (Free-Tip Rotor I, FTR I) showed its high potential to eliminate the negative lift on the advancing tip and the vibratory lift loading on the tip around the azimuth.

This analysis also indicated a possibility of utilizing the Free-Tip configuration to generate a longitudinal cyclic moment for the longitudinal trim. The tip response analysis of this application, called Passive Cyclic Control Device (Free-Tip Rotor II, FTR II), showed that the Free-Tip with an airfoil which has a significant negative pitching moment is capable of generating a large once-per- revolution lift oscillation which results in the cyclic moment useful for longitudinal trim.

The performance analysis of the FTR II using a three dimensional model indicated that the trailing vortices shed from the junction between the tip and inboard section has a large effect on the FTR II performance. The trailing vortices shed from the junction creates a large upwash at the tip. This upwash component prevents the advancing tip from carrying negative lift, and results in much less longitudinal cyclic moment than expected. Since the numerical model utilizes an infinitesimal vortex core, this effect may be exaggerated. Experimental analysis is necessary to verify its true effect.

Assuming that the wake model in the program is valid, the final configuration resulted in a performance improvement of 3.2 % in power requirement and 0.5 % in lift-drag ratio over a conventional rotor.

The following recommendations are made for the future research.

1. Improvement of wake model of the existing program

The vortex model should have a finite size core.

2. Application of lifting surface theory
   The lifting surface theory has better accuracy in predicting the aerodynamic load distribution. Since the local phenomenon (lift on the advancing tip) plays more important role in the FTR configuration than in a conventional rotor, a possibility of applying the lifting surface theory to the FTR should be investigated (Reference 8).

3. Experimental verification of the wake model
   The wake measurement for a conventional rotor and FTR configuration should be peformed to verify the numerical model and to improve it if necessary.

4. High subsonic/transonic airfoil wind tunnel test
   This is required to construct more realistic airfoil tables. More supercritical type airfoil should be tested. Investigation of unsteady effect on each airfoil is also desirable.

5. Improvement on the inboard section
   Usage of a rotor airfoil, designed by a supercritical airfoil scheme, such as NLR-1, Lockheed Georgia, etc. (Reference 12, 31 & 32) should be considered. These airfoils tend to have less drag due to compressibility effect while a low level of pitching moment is maintained.

6. Wind tunnel test of FTR II
   Finally, experimental investigations of FTR II performance must be performed.

Appendix A References

1. Stroub, R.H., "An Analytical Investigation of the Free-Tip Rotor for Helicopters.", NASA TM 81345 February 1982

2. Lan, C. E., "Some Applications of the Quasi Vortex-Lattice Method in Steady and Unsteady Aerodynamics", NASA SP-405 "Vortex Lattice Utilization", pp 385 - 406, 1976

3. Stroub, R. H., "An Experimental Investigation of a Free-Tip Rotor Configuration in a Forward Flight Wind-Tunnel Test", NASA TM 84409, October 1983

4. Velkoff, H. R. & Parker, T. W., "An Introductory Study of the H-force Rotor", The Ohio State University Research Foundation RF Project 760964/712528, May 1982

5. Davis, S. J., "Predesign Study for a Modern 4-Bladed Rotor for RSRA", NASA CR 166155, March 1981

6. Boeing Vertol Company, "Rotor Airloads and Performance Analysis with Non-Uniform Induced Inflow", Boeing Vertol Document No. D8 0312, Jan. 1968

7. AGARD, "Helicopter Aerodynamics and Dynamics", AGARD-LS-63, 1973

8. Kumagai, H., "Preliminary Studies on a Numerical Simulation of Helicopter Rotor in Forward Flight", M.S. Thesis, Department of Aerospace Engineering, The University of Kansas, 1982

9. Bisplinghoff, R. L., Ashley, H. & Halfman, R. L., "Aeroelasiticity", Addison - Wisley, 1955

10. McViegh, M. A., Rosenstein, H. & Bartie, K., "Investigation of a Rotor

System Incorporating a Constant Lift Tip", NASA CR 166361 October 1981

11. Boeing Vertol Company, "Aeroelastic Rotor Analysis Program, C-60", Boeing Vertol Document No. D201-10378-1, May 1974

12. Blackwell, J. A. & Hinson, B. L., "The Aerodynamic Design of an Advanced Rotor Airfoil", NASA CP 2046 "Advanced Technology Airfoil Research" Volume II, 1979, pp 121

13. Whitcomb, R. T., "Review of NASA Supercritical Airfoils", International Council of the Aeronautical Sciences, ICAS Paper No. 74-10, August 1974

14. McGhee, R. J. & Beasley, W. D., "Low Speed Aerodynamic Characteristics of a 17 Percent Thick Airfoil Section Designed for General Aviation Applications", NASA TN D-7428, Dec. 1973

15. McGee, R. J., Beasley, W. D. & Somers, D. M., "Low-Speed Aerodynamic Characteristics of a 13-percent Thick Airfoil Section Designed for General Aviation Application", NASA TM X-72697, May, 1977

16. McGhee, R. J., Beasley, W. D. & Whitcomb, R. T., "NASA Low- and Medium-Speed Airfoil Development", NASA CP 2046 "Advanced Technology Airfoil Research", Volume II, 1979, pp 1.

17. McGhee, R. J. & Beasley, W. D., "Low-Speed Aerodynamic Characteristics of a 13-Percent-Thick Medium-Speed Airfoil Designed for General Aviation Applications" NASA TP 1498, August 1979

18. Harris, C. D., "Aerodynamic Characteristics of 10-percent Thick NASA Supercritical Airfoils with Different Aft Camber", NASA TM X-72007, February 1975

19. Harris, C. D., "Aerodynamic Characteristics of the 10-percent-Thick NASA Supercritical Airfoil 33 Designed for a Normal-Force Coefficient of 0.7", NASA TM X-72711

20. Harris, C. D., "Aerodynamic Characteristics of Two 10-percent-Thick NASA Supercritical Airfoils with Different Upper Surface Curvature Distributions", NASA TM X-2977, February 1974

21. Harris, C. D., "Aerodynamic Characteristics of an Improved 10-percent-Thick NASA Supercritical Airfoil", NASA TM X-2978, February 1974

22. Bauer, F., Grabedian, P. & Korn, D., "Supercritical Wing Section I", Lecture Notes in Economics and Mathematical Systems, Springer-Verlag, 1972

23. Bauer, F., Grabedian, P., Korn, D. & Jameson, A., "Supercritical Wing Section II", Lecture Notes in Economics and Mathematical Systems, Springer-Verlag, 1975

24. Bauer, F., Grabedian, P. & Korn, D., "Supercritical Wing Section III", Lecture Notes in Economics and Mathematical Systems, Springer-Verlag, 1977

25. Wirz, H. J. & Smolderen, J. J., "Numerical Method in Fluid Dynamics", McGraw Hill, 1978

26. US Army, "US Army Helicopter Design Datcom", USAAMRDL CR 76-2, 1976

27. Abbott, I. H. & von Doenhoff A. E., "Theory of Wing Sections", Dover Publications Inc., 1957

28. Harris, F. D. & McVeigh, M. A., "Uniform Downwash with Rotors Having a Finite Number of Blades", J. of American Helicopter Society, Jan. ,1976

29. Bramwell, A. R. S., "Helicopter Dynamics", Edward Arnold Ltd., 1977

30. Gessow, A. & Myers, G. J. Jr., "Aerodynamics of the Helicopter", Frederic Ungar Publishing Co. 1981

31. Bingham, G. J., Noonan, K. W. & Jones, H. E. "Results of an Investigation of several New Rotorcraft Airfoils as Related to Airfoil Requirements", NASA CP 2046, "Advanced Technology Airfoil Research" Volume II, 1979, pp109

32. Morris, C. E. K. Jr., "A Flight Investigation of Rotor Airfoil", NASA CP 2046, "Advanced Technology Airfoil Research" Volume II, 1979, pp141

Appendix B MS(1)-0313 Airfoil Table for B-65 Program

This airfoil table contains two dimensional aerodynamic data (c_ℓ, c_d and c_m) of MS(1)-0313 airfoil for various Mach numbers and angles of attack. The table was constructed to be read by Boeing Vertol B-65 program.

The table number to be used in the B-65 input file is "101".

This data set was generated by NYU program version H (Bauer Code) available on CRAY 1/S at NASA Ames Research Center.

The data set is strictly for steady and two dimensional case and contains no experimental information.

MS(1)-0313 Airfoil Table

```
    1Ø1  1Ø1 MS(1)-Ø313 AIRFOIL,  REVISED 9/22/83 H.K.
18Ø.       18Ø.
Ø.         1.          1.          1.          1.
    9
.Ø         .1          .4          .7          .75         .8          .85
.9         .95
    9
Ø.         4.          6.          8.          35Ø.        352.        354.
356.       36Ø.
.2819      .7277       .9552       1.1738      -.85Ø9      -.6392      -.4Ø47
-.1658     .2819
    9
Ø.         4.          6.          8.          35Ø.        352.        354.
356.       36Ø.
.2833      .7379       .9539       1.1799      -.863Ø      -.6435      -.4Ø89
-.1743     .2833
    9
Ø.         4.          6.          8.          35Ø.        352.        354.
356.       36Ø.
.3Ø66      .7971       1.Ø442      1.285Ø      -.9944      -.7129      -.4547
-.1923     .3Ø66
    8
Ø.         4.          6.          35Ø.        352.        354.        356.
36Ø.
.3854      1.1375      1.5232      -1.4185     -1.1169     -.8272      -.3453
.3854
    7
Ø.         4.          6.          352.        354.        356.        36Ø.
.4134      1.2672      1.6224      -1.1695     -.6238      -.42Ø8      .4134
    7
Ø.         4.          6.          352.        354.        356.        36Ø.
.5169      1.2521      1.4765      -1.1187     -.8323      -.4489      .5169
    6
Ø.         4.          352.        354.        356.        36Ø.
.44Ø6      1.ØØ79      -.9534      -.74Ø5      -.4126      .44Ø6
    6
Ø.         4.          352.        354.        356.        36Ø.
.2555      .7322       -.7552      -.5894      -.2964      .2555
    5
Ø.         352.        354.        356.        36Ø.
.1184      -.6744      -.5Ø35      -.3242      .1184
8.         35Ø.
   21
Ø.         Ø.5         1.          1.5         2.          2.5         3.
4.         5.          6.          8.          35Ø.        352.        353.
354.       355.        356.        357.        358         359.        36Ø.
    9
.Ø         .1          .4          .7          .75         .8          .85
.9         .95
.ØØ983     .ØØ981      .Ø1Ø76      .Ø1125      .Ø127Ø      .Ø2511      .Ø4787
.Ø782Ø     .1Ø326
    8
.Ø         .1          .4          .7          .75         .8          .85
.9
.ØØ996     .ØØ995      .Ø1Ø82      .Ø1Ø77      .Ø1357      .Ø2615      .Ø5375
.Ø8438
    8
.Ø         .1          .4          .7          .75         .8          .85
.9
.Ø1ØØ9     .Ø1ØØ9      .Ø1Ø68      .Ø113Ø      .Ø1484      .Ø3231      .Ø6172
.Ø9Ø94
```

MS(1)-0313 Airfoil Table (continued)

```
    8
.Ø          .1          .4          .7          .75         .8          .85
.9
.Ø1Ø22      .Ø1Ø23      .Ø1Ø93      .Ø1185      .Ø1625      .Ø4531      .Ø7Ø78
.Ø975Ø
    8
.Ø          .1          .4          .7          .75         .8          .85
.9
.1Ø136      .Ø1Ø37      .Ø1Ø99      .Ø13ØØ      .Ø1875      .Ø5738      .ØØØØØ
.1Ø5ØØ
    8
.Ø          .1          .4          .7          .75         .8          .85
.9
.Ø1Ø49      .Ø1Ø5Ø      .Ø11Ø5      .Ø16ØØ      .Ø2656      .Ø7375      .Ø9125
.11ØØ8
    8
.Ø          .1          .4          .7          .75         .8          .85
.9
.Ø1Ø62      .Ø1Ø64      .Ø1111      .Ø2Ø46      .Ø4ØØØ      .Ø6922      .1Ø169
.11844
    8
.Ø          .1          .4          .7          .75         .8          .85
.9
.Ø1Ø86      .Ø1Ø92      .Ø1122      .Ø3226      .Ø7268      .12Ø69      .13Ø48
.13427
    6
.Ø          .1          .4          .7          .75         .8
.Ø1132      .Ø1129      .Ø1181      .Ø486Ø      .11Ø46      .15366
    6
.Ø          .1          .4          .7          .75         .8
.Ø1175      .Ø1165      .Ø1239      .Ø757Ø      .14824      .18563
    3
.Ø          .1          .4
.Ø1317      .Ø1321      .Ø137Ø
    4
.Ø          .1          .4          .7
.Ø1298      .Ø137Ø      .Ø1833      .13Ø43
    9
.Ø          .1          .4          .7          .75         .8          .85
.9          .95
.Ø1213      .Ø1121      .Ø13Ø2      .Ø7Ø18      .1Ø996      .14994      .16824
.17827      .19693
    9
.Ø          .1          .4          .7          .75         .8          .85
.9          .95
.Ø1143      .Ø1114      .Ø1248      .Ø4922      .Ø7277      .1125Ø      .13978
.15494      .17624
    9
.Ø          .1          .4          .7          .75         .8          .85
.9          .95
.Ø1Ø84      .Ø11Ø7      .Ø1194      .Ø3399      .Ø5Ø46      .Ø8Ø86      .11132
.13181      .15555
    9
.Ø          .1          .4          .7          .75         .8          .85
.9          .95
.Ø1Ø65      .Ø1Ø49      .Ø1142      .Ø2281      .Ø3231      .Ø5538      .Ø82ØØ
.11Ø94      .13931
    9
.Ø          .1          .4          .7          .75         .8          .85
.9          .95
.Ø1Ø45      .ØØ991      .Ø1Ø89      .Ø1394      .Ø2Ø77      .Ø3381      .Ø6125
```

MS(1)-0313 Airfoil Table (continued)

```
.Ø9455     .123Ø6
    9
.Ø         .1         .4         .7         .75        .8         .85
.9         .95
.Ø1Ø3Ø     .ØØ989     .Ø1Ø86     .Ø1219     .Ø1631     .Ø2677     .Ø4646
.Ø8ØØØ     .11ØØØ
    9
.Ø         .1         .4         .7         .75        .8         .85
.9         .95
.Ø1Ø14     .ØØ986     .Ø1Ø63     .Ø1141     .Ø1462     .Ø2415     .Ø3877
.Ø716Ø     .Ø9815
    9
.Ø         .1         .4         .7         .75        .8         .85
.9         .95
.ØØ999     .ØØ984     .Ø1Ø79     .Ø113Ø     .Ø1354     .Ø2365     .Ø3923
.Ø715Ø     .Ø9585
    9
.Ø         .1         .4         .7         .75        .8         .85
.9         .95
.ØØ983     .ØØ981     .Ø1Ø76     .Ø1125     .Ø127Ø     .Ø2511     .Ø4787
.Ø782Ø     .1Ø326
-.Ø5Ø3     .1151
    9
Ø.         4.         6.         8.         35Ø.       352.       354.
356.       36Ø.
    9
.Ø         .1         .4         .7         .75        .8         .85
.9         .95
-.Ø598     -.Ø6Ø1     -.Ø649     -.Ø768     -.Ø845     -.1544     -.2Ø16
-.168Ø     -.Ø943
    8
.Ø         .1         .4         .7         .75        .8         .85
.9
-.Ø561     -.Ø579     -.Ø599     -.1Ø91     -.222Ø     -.3148     -.2969
-.2424
    6
.Ø         .1         .4         .7         .75        .8
-.Ø557     -.Ø544     -.Ø567     -.1779     -.3189     -.364Ø
    3
.Ø         .1         .4
-.Ø536     -.Ø536     -.Ø5Ø3
    4
.Ø         .1         .4         .7
-.Ø562     -.Ø548     -.Ø58Ø     .Ø199
    9
.Ø         .1         .4         .7         .75        .8         .85
.9         .95
-.Ø564     -.Ø565     -.Ø647     -.Ø263     .Ø453      .1Ø26      .1151
.Ø782      .Ø644
    9
.Ø         .1         .4         .7         .75        .8         .85
.9         .95
-.Ø594     -.Ø592     -.Ø64Ø     -.Ø365     -.Ø244     .Ø348      .Ø7Ø6
.Ø493      .Ø253
    9
.Ø         .1         .4         .7         .75        .8         .85
.9         .95
-.Ø627     -.Ø612     -.Ø664     -.Ø774     -.Ø69Ø     -.Ø384     -.ØØ73
-.Ø427     -.ØØ53
    9
.Ø         .1         .4         .7         .75        .8         .85
```

MS(1)-0313 Airfoil Table (continued)

.9	.95					
-.Ø598	-.Ø5Ø1	-.Ø649	-.Ø768	-.Ø845	-.1544	-.2Ø16
-.1568Ø	-.Ø943					